Probing cesium Rydberg atoms close to a sapphire surface

Biplab Dutta

UNIVERSITÉ PARIS XIII - SORBONNE PARIS NORD

École Doctorale Sciences, Technologies, Santé Galilée

Probing caesium Rydberg atoms close to a sapphire surface

Sonder les atomes de césium Rydberg à proximité d'une surface de saphir

---

THÈSE DE DOCTORAT
présentée par

Biplab DUTTA

Laboratoire de Physique des Lasers
pour l'obtention du grade de

DOCTEUR EN PHYSIQUE

soutenue le 13/10/2023 devant le jury d'examen composé de :

Vincent Lorent	Président du jury
Robert Loew	Rapporteur
Fabienne Goldfarb	Rapporteuse
Franck Pereira Dos Santos	Examinateur
Stefan Scheel	Examinateur
Athanasios Laliotis	Directeur de thèse
Isabelle Maurin	Co-directrice de thèse

চিত্ত যেথা ভয়শূন্য / Where the mind is without fear

চিত্ত যেথা ভয়শূন্য, উচ্চ যেথা শির,
জ্ঞান যেথা মুক্ত, যেথা গৃহের প্রাচীর
আপন প্রাঙ্গণতলে দিবসশর্বরী
বসুধারে রাখে নাই খন্ড ক্ষুদ্র করি,
যেথা বাক্য হৃদয়ের উৎসমুখ হতে
উচ্ছ্বসিয়া উঠে, যেথা নির্বারিত স্রোতে

ভারতেরে সেই স্বর্গে করো জাগরিত।

– রবীন্দ্রনাথ ঠাকুর (*নৈবেদ্য* হতে সংগ্রহীত)

Where the mind is without fear and the head is held high
Where knowledge is free
Where the world has not been broken up into fragments
By narrow domestic walls
Where words come out from the depth of truth
Where tireless striving stretches its arms towards perfection

Into that heaven of freedom, my Father, let my country awake.

– Rabindranath Thakur (Collected from *Naivedya*)

Abstract

The Casimir-Polder interaction between atoms and macroscopic surfaces is a fundamental prediction of quantum electrodynamics of importance for precision measurements, quantum technologies and our understanding of the electromagnetic properties of materials. In the near field, Casimir-Polder interactions are described as the interaction of the fluctuating atomic dipole with its surface-induced image, which evolves as $-C_3/z^3$ where z is the atom-surface distance and C_3 is the van der Waals coefficient. In this thesis, we study both theoretically and experimentally the Casimir-Polder interaction between a highly excited caesium atom (Rydberg atom) and a dielectric surface. Our theoretical study extends previous studies to include higher-order terms in the atom-surface interaction, beyond the dipole-dipole interaction term investigated in the seminal work of Casimir and Polder. In particular, we include quadrupole-quadrupole and dipole-octupole interaction terms with a distance dependence of $-C_5/z^5$ giving explicit calculations of the C_5 coefficients for most common alkali atoms. We also describe a new selective reflection experiment probing Cs Rydberg atoms ($15-17D_{3/2}$ and $16-17S_{1/2}$) at nanometric distances away from a sapphire surface. The experiment is performed in an all-sapphire vapour cell using stepwise excitation spectroscopy that includes a pumping step at $6S_{1/2} \rightarrow 6P_{1/2}$ (894nm) and a selective reflection probing step at $6P_{1/2} \rightarrow nS_{1/2}, nD_{3/2}$ with n = 15 - 17 ($\sim$ 510 nm). To analyze our experimental spectra, we extend selective reflection theory beyond the infinite Doppler approximation, including in our analysis the Maxwell-Boltzmann distribution of atomic velocities. Fitting our theoretical lineshape model to our experimental spectra allows us to extract the C_3 van der Waals coefficient for the probed caesium excited states. This C_3 measurement exceeds the theoretical predictions of Casimir-Polder theory by a factor of about 1.5 - 2, depending on the probed state. Finally, we describe a new thin-cell experiment that aims to illuminate the reported disagreement between theory and experiment for the C_3 coefficient and provide a first experimental measurement of the C_5 coefficient (experimental study of higher-order interactions).

Résumé

L'interaction Casimir-Polder entre un atome et une surface macroscopique est une prédiction fondamentale de l'électrodynamique quantique, importante pour les mesures de précision, les technologies quantiques et notre compréhension des propriétés électromagnétiques des matériaux. En champ proche, les interactions Casimir-Polder sont décrites comme l'interaction du dipôle atomique fluctuant avec son image induite par la surface, qui évolue comme $-C_3/z^3$, où z est la distance atome-surface et C_3 le coefficient de van der Waals. Dans cette thèse, nous étudions théoriquement et expérimentalement l'interaction Casimir-Polder entre un atome de césium fortement excité (atome de Rydberg) et une surface diélectrique. Notre théorie étend les études précédentes pour inclure des termes d'ordre supérieur dans l'interaction atome-surface, au-delà du terme d'interaction dipôle-dipôle étudié dans le travail de Casimir et Polder. En particulier, nous incluons des termes d'interaction quadrupôle-quadrupôle et dipôle-octupôle avec une dépendance en distance de $-C_5/z^5$. Nous fournissions également des calculs explicites des coefficients C_5 pour la plupart des atomes alcalins courants. Nous décrivons également une nouvelle expérience de réflexion sélective sondant des atomes de Rydberg de Cs ($15-17D_{3/2}$ et $16-17S_{1/2}$) à des distances nanométriques d'une surface de saphir. L'expérience est réalisée dans une cellule à vapeur entièrement en saphir en utilisant une spectroscopie d'excitation par étapes qui comprend une étape de pompage à $6S_{1/2} \rightarrow 6P_{1/2}$ (894nm) et une étape de sondage par réflexion sélective à $6P_{1/2} \rightarrow nS_{1/2}, nD_{3/2}$ avec n = 15 - 17 ($\sim$ 510 nm). Afin d'analyser nos spectres expérimentaux, nous étendons la théorie de la réflexion sélective au-delà de l'approximation Doppler infinie, en incluant dans notre analyse la distribution Maxwell-Boltzmann des vitesses atomiques. L'ajustement de nos spectres expérimentaux avec nos modèles théoriques nous permet d'extraire le coefficient de van der Waals C_3 pour les états excités du césium sondés. Les résultats expérimentaux dépassent nos prédictions théoriques (d'un facteur d'environ 1,5 à 2, selon l'état sondé). Enfin, nous décrivons une nouvelle expérience en cellule mince qui vise à éclaircir le désaccord signalé entre la théorie et l'expérience pour le coefficient C_3 et à fournir une première mesure expérimentale du coefficient C_5 (étude expérimentale des interactions d'ordre supérieur).

Acknowledgments

I extend my heartfelt gratitude to my father, Birendra, and my mother, Kalpana, whose unwavering encouragement bolstered my journey. Their support has been invaluable.
A special acknowledgement goes to Rimpa, my wife, whose unwavering support has been the bedrock of our shared life. Her incredible support, especially during my doctoral pursuits, was evident in her willingness to leave India and accompany me to France.
I am deeply indebted to my thesis supervisor, Athanasios Laliotis, for warmly welcoming me into his team and providing impeccable guidance throughout this thesis. His willingness to share his profound scientific knowledge, coupled with his accessibility to insightful discussions, has been pivotal. I am particularly grateful for his meticulous corrections and invaluable advice on refining my articulation of thoughts. His visionary guidance significantly shaped this thesis.
I am equally grateful to my co-supervisor, Isabelle Maurin, for not only fostering countless scientific discussions but also for her exceptional ability to uplift spirits. Her mentorship taught me valuable lessons in organization and composure during challenging times.
My heartfelt thanks extend to Danial Bloch for the enriching experiences during my doctoral journey. His invaluable insights into experiments and scientific expertise were immensely beneficial.
I express my gratitude to Martial Ducloy for the consistently constructive discussions.
I owe immense thanks to Paolo Pedri and Joao Carlos de Aquino Carvalho for their exceptional guidance, friendship, and unforgettable moments.
Special appreciation goes to Horacio Failache for sharing his invaluable experience, especially in the initial stages, which significantly contributed to my technical acumen within the team.
I would like to express my gratitude to my colleagues Esther Butery and Hippolyte Mouhanna for their valuable contributions to the discussions on physics, as well as for the countless enjoyable moments we shared in the office throughout the majority of my thesis journey.
A heartfelt thank you to Guadalupe Garcia for her invaluable help and unwavering friendship during this thesis.
I extend my gratitude to Stefan Scheel for the enriching discussions that broadened my understanding of the subject matter throughout my thesis. Additionally, I am thankful to Chris Boldt for his friendship and for guiding me through the numerical computational challenges.
I express my sincere appreciation to Anne Amy Klein, the director of LPL, for accepting me as a doctoral student.
I am deeply thankful to Marcos Oria, Marine Chevrollier and Maki Tachikaw for their invaluable advice, friendship, scientific exchanges, and unwavering encouragement.
Gratitude also goes out to the friends I made during my time at LPL: (to name some) Pablo Reséndiz Vázquez, Lachene, Elias Moufarej, Junior Lukusa, Francisco Perales, Gabriel Dutier, Laurent Vernac, Benoit Darquie, and Marc Martin.
I extend my thanks to Fabrice Wiotte, Albert Kaladjian, Thierry Billet, Marc Barbier, and Stephane Simonazzi for their unwavering technical support throughout my thesis.

I am grateful to the efficient LPL administration, specifically Maryse Medina and Carole Grangier, for their consistent support.
Last but by no means least, I would like to thank all the members of the jury for reviewing this thesis.

Contents

1 Introduction **17**

2 Non-retarded Casimir-Polder interactions between highly excited atom and dielectric surface **21**

2.1 Method of Images: Interaction between a Rydberg atom and its surface-induced image . . . 23
2.1.1 Multipole expansion of the potential . . . 23
2.1.2 Interaction energy between an atomic and its image (W) . . . 24
2.2 Calculation of the atom-surface interaction coefficients (C_3, C_4, C_5) . . . 29
2.2.1 Dipole-dipole (image) interactions coefficient (C_3) . . . 31
2.2.2 Dipole-quadrupole (image) interactions coefficient (C_4) . . . 32
2.2.3 Quadrupole-quadrupole (image) and dipole-octupole (image) interactions coefficient (C_5) . . . 33
2.3 Evaluation of the interaction coefficient for relevant Rydberg states . . . 34
2.3.1 Evaluation of dipole-dipole (image) interaction coefficient (C_3) . . . 35
2.3.2 Evaluation of quadrupole-quadrupole (image) interaction coefficient (C_5^{QQ}) . . . 37
2.3.3 Evaluation of dipole-octupole (image) interaction coefficient ($C_{5,pT}$) 39
2.4 Casimir-Polder (CP) formulation in the non-retared limit to estimate the dipole-dipole (image) interaction coefficient . . . 40
2.4.1 For an ideal reflector . . . 40
2.4.2 For a dielectric surface . . . 44

3 Spectroscopy of Casimir-Polder Interaction: Selective Reflection (SR) Spectroscopy and Thin Cell (TC) Spectroscopy **46**

3.1 Selective reflection (SR) spectroscopy . . . 47
3.1.1 A general solution to selective reflection (SR) spectroscopy . . . 50
3.1.2 Selective reflection signal in the absence of atom surface interaction 53
3.1.3 Frequency modulated selective reflection signal (FMSR) . . . 55
3.1.4 Selective reflection signal in the presence of atom surface interaction 57
3.2 A numerical approach on solving selective reflection spectroscopy . . . 59
3.2.1 Numerical approach to solve the z and z' integral . . . 59
3.2.2 Selective reflection lineshapes for different atomic velocities . . . 66
3.2.3 Selective reflection lineshape for different atomic velocity distribution and atom-surface interactions . . . 67
3.3 Nanometric thin cell spectroscopy (TC) . . . 72
3.3.1 Nanometric thincell as Fabry–Pérot (FP) cavity . . . 73

3.3.2 Thin cell (TC) lineshape in the presence of strong atom surface interactions . . . 75

4 Description of the atomic system and experimental setup 81
4.1 Caesium atomic levels and spectroscopic scheme . . . 82
4.2 Experimental setup . . . 85
4.2.1 Lasers . . . 85
4.2.2 A brief discussion of the cells . . . 89
4.2.3 Data acquisition unit and automation of the experimental setup . 96
4.3 Absorption spectroscopy in a volumetric cell . . . 97
4.3.1 Two-step absorption spectroscopy . . . 97
4.3.2 Saturated absorption Spectroscopy . . . 104

5 Experimental results of Casimir Polder interaction on $nS_{1/2}$ and $nD_{3/2}$ (where n = 15, 16, 17) using selective reflection spectroscopy 107
5.1 Recording the FMSR spectra . . . 108
5.2 Frequency modulated selective reflection spectroscopy on $6P_{1/2} \rightarrow 16S_{1/2}, 17S_{1/2}$ transition . . . 111
5.2.1 Effect of pump and probe laser intensity . . . 111
5.2.2 Fitting procedure of the FMSR spectra . . . 112
5.2.3 C_3 and γ measurement from $6P_{1/2} \rightarrow 16S_{1/2}, 17S_{1/2}$ FMSR spectra 117
5.3 Frequency modulated selective reflection spectroscopy of $15D_{3/2}$ $17D_{3/2}$ and $18D_{3/2}$ . . . 120
5.3.1 Effect of pump and probe laser intensity . . . 120
5.3.2 Relative amplitude of $6P_{1/2} \rightarrow nS_{1/2}, nD_{3/2}$ (n = 15 - 17) FMSR spectra . . . 122
5.3.3 C_3 and γ measurement from $6P_{1/2} \rightarrow 15D_{3/2}, 16D_{3/2}$ and $17D_{3/2}$ FMSR spectra . . . 124
5.3.4 Remarks . . . 130

6 Conclusion and Perspectives 132
6.1 Overview of this thesis . . . 132
6.2 Preliminary work on probing Rydberg atoms in nanometric thin cell . . . 133

7 Appendix A 138
7.1 Interaction between atom and its surface induced image: method of images 138
7.2 Interaction energy between atom and its surface induced image . . . 140
7.2.1 Derivatives of the dipole moment . . . 141
7.2.2 Derivatives of the quadruple moment . . . 141
7.2.3 Interaction energy between dipole and image dipole ($W_{pp^{im}}$) . . . 142
7.2.4 Interaction energy between dipole and quadrupole image ($W_{pQ^{im}}$) 143
7.2.5 Interaction energy between quadrupole and image dipole ($W_{Qp^{im}}$) 143
7.2.6 Interaction energy between quadrupole and image quadrupole ($W_{QQ^{im}}$) 144

List of Figures

2.1 A Rydberg atom represented as a charge distribution $\rho(\mathbf{r})$ and its surface induced image $\rho^{im}(\mathbf{r}')$. The surface is on the x - y plane while z is the atom-surface separation and r is the separation between the atom and its image. . . . 23

2.2 Elements of the electric dipole, quadrupole and octupole moment tensors of the atom and its surface induced image. . . . 25

2.3 $|u(r/a_o)_{n,l}|^2$ (in arbitrary units) as function of r/a_o, where $[u(r/a_o)_{n,l}]$ is the radial wavefunction and a_o is the Bohr radius (in m^{-1}). . . . 30

2.4 Accessible Rydberg states Cs($nS_{1/2}, nD_{3/2}$) from the first excited state Cs($6P_{1/2}$). . . . 35

2.5 C_3 (in MHz μm^3) as function of n^{*4}. nS, nP and nD states are indicated by square, circle and triangle respectively (n is the principal quantum number). . . . 36

2.6 C_5 as a function of $(n^*)^8$. (a) nS, nP, and nD states are indicated by square, circle, and triangle respectively and different colours for different n quantum numbers. (b) enlarged plot for n = 15 and 20 (n is the principal quantum number). . . . 38

2.7 Real part of the sapphire surface response Re[S(ω)] as funtion of frequency (in cm^-1). Here, we use the geometric mean $(\epsilon_{ord}\ \epsilon_{ext})^{1/2}$ of the dielectric constants, which is the relevant parameter for Casimir-Polder calculations when the extraordinary axis is perpendicular to the sapphire window. The dotted lines show the positions of the virtual couplings from the $15D_{3/2}$ state. . . . 45

3.1 Geometry of incident $\mathcal{E}_i$, refracted $\mathcal{E}_t$ and reflected $\mathcal{E}_r$ waves. The $x-y$ plane is the interface between the atomic vapour and the surface. n is the refractive index of the surface and $n_v(\omega)$ is the effective refractive index of the atomic vapour. θ_0 is the incident angle (θ_0«1). z is atom surface separation. . . . 48

3.2 Selective reflection lineshape in the absence of atom-surface interaction for different values of homogeneous linewidth. $\Delta = \omega - \omega_0/kv_p$ where v_p is the most probable velocity. . . . 54

3.3 Selective reflection lineshape in the absence of atom surface interaction: SR signal (Dash line), FMSR signal (solid line) in normalized frequency scale i.e Δ/Γ. . . . 56

3.4 Real part of $\mathcal{H}(z)$ as a function of z (in micron) for C_3 = 1 MHz μm^3, γ = 25 MHz, δ = - 50 MHz and v_z = 100 m/s. . . . 60

3.5 Logistic function $f(z)$ as a function of z (in μm) for different L values (in μm). . . . 62

3.6 Real part of $\mathcal{H}(z) \times f(z)$ (for L = 15 μm) as a function of z (in μm). . . 62
3.7 The amplitude variation of the real part of integral $\mathcal{I}$ for different cut-off points L for different combination of (a) γ, (b) v_z and (c) C_3 while keeping other two variables as constant. 63
3.8 $\Re[\mathcal{H}(z)]$ and $\Re[\mathcal{H}(z) - \mathcal{H}_0(z)]$ as a function of z (in μm). 65
3.9 Selective reflection lineshape with C_3 = 1 MHz μm^3, γ = 100 MHz for different atomic velocities (v_z). 67
3.10 Normalized FMSR lineshapes (normalized to maximum amplitude) for different thermal velocity distributions. The infinite Doppler and motionless atom approximations are marked with arrows. Here, C_3 = 10 kHz μm^3 and γ = 15 MHz. 68
3.11 Normalized FMSR lineshape (normalized to the maximum amplitude) for $C_3(17D_{3/2})$ = 8.8 MHz μm^3 and γ = 50 MHz considering the motionless atom approximation (dotted line), infinite Doppler approximation (dashed line) and Maxwell Boltzmann (MB) distribution with T = 500 K (in solid line). 69
3.12 Normalized SR lineshape (normalized to the maximum amplitude) for $C_3(17D_{3/2})$ (solid line: $\sim$ 8.8 MHz μm^3) and $C_3(17D_{3/2})$ & $C_5(17D_{3/2})$ (grey dashed line: $\sim$ 8.8 MHz μm^3 & 2.07 kHz μm^5) having a homogeneous linewidth, γ = 50 MHz. 70
3.13 Transmission path of a near normal incident beam $\mathcal{E}_{in}$ through the thin cell which acts as a low finesse Fabry–Pérot interferometer. $\mathcal{E}_R$, and $\mathcal{E}_T$ is the reflected and transmitted field respectively. $\alpha \ll 1$ is the incident angle which has been deliberately upscaled in the figure for convenience. $z > 0$ is the direction of propagation. 72
3.14 Thin cell with multiple images where the atom is placed at a distance z from surface 1 and $L - z$ from surface 2. 75
3.15 Normalized transmission (TS) and reflection (RS) spectra as a function of cell thickness (L$>\lambda/2$ where λ = 514 nm) with $C_3(16S_{1/2})$ (dashed lines: $\sim$ 4.1 MHz μm^3) and $C_3(16S_{1/2})$ & $C_5(16S_{1/2})$ (solid line: $\sim$ 4.1 MHz μm^3 & 0.45 kHz μm^5). Signal amplitude is normalized to the maximum amplitude of the signal. A and B correspond to γ = 200, 1000 MHz respectively. When the thickness is an integral multiple of $\lambda/2$ (514 nm and 771 nm) the reflection signal (RS) becomes zero. 77
3.16 Normalized transmission (TS) and reflection (RS) spectra as a function of cell thickness (L$>\lambda/2$ where λ = 514 nm) with $C_3(16S_{1/2}) \sim$ 4.1 MHz μm^3 (dashed lines) and $C_3(16S_{1/2}) \sim$ 4.1 MHz μm^3 & $C_5(16S_{1/2}) \sim$ 0.45 kHz μm^5 (solid line). Signal amplitude is normalized to the maximum amplitude of the signal. $\Delta = \Delta_1(C_3 + C5) - \Delta_2(C_3)$, additional redshift of the dip for considering quadrupole interactions. 78
3.17 Additional redshift of the atomic resonance as a function of cell thickness in the presence of the quadrupole-quadrupole interactions for some relevant Rydberg states. 80

4.1 Step-wise excitation scheme for probing Rydberg state. Pumping from $6S_{1/2}(F = 3) \rightarrow 6P_{1/2}(F = 4)$ at 894 nm and probing $6P_{1/2}(F = 4, 3) \rightarrow nS_{1/2}, nD_{3/2}$ (n = 15 - 18) at 507 - 513 nm. 82

4.2 A schematic of the experimental setup highlighting some of the key components. . . . 84
4.3 Pump and re-pump configuration on $6S_{1/2} \rightarrow 6P_{1/2}$ transition. . . . 86
4.4 Standard deviation of the probe laser intensity at different frequencies. The input power is about 10 mW. . . . 87
4.5 Frequency deviation of free-running probe laser as a function of integration time (in sec). . . . 88
4.6 A photo of the SR cell. . . . 89
4.7 Selective reflection cell with the ovens and the thermocouples. . . . 90
4.8 Ground state Caesium ($6S_{1/2}$) vapour pressure (in Torr) and atomic density (in atom cm^{-3}) as a function of temperature T (in °C) (where we assume $T_s = T_r = T$). . . . 92
4.9 A Photo of the thin cell with a coin for reference. . . . 93
4.10 Schematic of thin cell (side view) indicating the ovens and thermocouples. 93
4.11 Transmission path of a near normal incident beam (1) through the thin cell which acts as a low finesse Fabry–Pérot interferometer. Beams indicated by (2) and (3) are the reflected beams from the first window and the thin cell respectively. $\alpha \ll 1$ is the incident angle which has been deliberately upscaled in the figure for convenience. . . . 94
4.12 Reflectance (R_c) as a function of cell thickness (d) (red line: 894 nm, green line: 512 nm). The straight line shows the value of measured reflectance. By using two different wavelengths, we can pinpoint the cell thickness to be 477 ± 5 nm. . . . 95
4.13 Normalized $6P_{1/2} \rightarrow 15D_{3/2}$ absorption spectrum with the pump laser locked on $6S_{1/2}(F = 3) \rightarrow 6P_{1/2}(F = 4)$ transition. Signal amplitude normalized to off-resonant transmission probe powers. Laser intensities: pump ~ 3.5 mW/cm^2, probe ~ 2.5 mW/cm^2. Cs vapor pressure: ~ 0.1 mTorr. Horizontal dashed line: the zero level and vertical dashed lines: $6P_{F=4,3} \rightarrow 15D_{3/2}$ transition in volume. . . . 97
4.14 Normalized $6P_{1/2} \rightarrow 15D_{3/2}$ absorption spectrum with the pump laser locked on $6S_{1/2}(F = 3) \rightarrow 6P_{1/2}(F = 4)$ transition. Signal amplitudes: normalized to the maximum amplitude of each absorption line. Laser intensities: pump ~ 3.5 mW/cm^2, probe ~ 2.5 mW/cm^2. Cs vapor pressure: ~ 0.1 mTorr. Horizontal dashed line: the zero level and vertical dashed lines: $6P_{F=4,3} \rightarrow 15D_{3/2}$ transition in volume. . . . 98
4.15 Normalized $6P_{1/2} \rightarrow 15D_{3/2}$ absorption spectra with pump intensities of ~ 50 mW/cm^2 for different ground state ($6S_{1/2}$) vapour pressure. Signal amplitudes are normalized to off-resonant transmission probe powers. Probe laser intensities ~ 2.5 mW/cm^2. A horizontal dashed line indicates the zero level and two vertical dashed lines mark $6P_{F=4,3} \rightarrow 15D_{3/2}$ transition in volume. . . . 99

4.16 Normalized $6P_{1/2} \rightarrow 15D_{3/2}$ absorption spectra for Pump frequency : (a) pump frequency on resonance, $\omega_{IR} = \omega_0$ (b) pump frequency, $\omega_{IR} = \omega_0 - \delta$ (c) pump frequency, $\omega_{IR} = \omega_0 + \delta$. Signal amplitudes are normalized to the maximum amplitude of each absorption line. The pump frequency detuning is $\delta \approx 150$ MHz leading to a ≈ 260 MHz shift of the sub-Doppler peaks in the probe absorption spectrum. A horizontal dashed line indicates the zero level and two vertical dashed lines mark $6P_{F=4,3} \rightarrow 15D_{3/2}$ transition in volume. 100
4.17 An example of $6S_{1/2} \rightarrow 6P_{1/2}$ pumping configuration. 101
4.18 (a) Normalized $6P_{1/2} \rightarrow 15D_{3/2}$ absorption spectra (b) normalized FM $6P_{1/2} \rightarrow 15D_{3/2}$ absorption spectra for all 4 possible pumping configurations on the $6S_{1/2} \rightarrow 6P_{1/2}$ line. The signal amplitude is normalized to the maximum amplitude. Pump laser: on resonance (addressing $v_z = 0$ atoms) with AM modulated at 1.7 kHz. Probe laser: FM modulated with 23 MHz peak-to-peak excursion at 233 kHz. The directly pumped hyperfine component always presents a peak at $v_z = 0$ due to the velocity selection of the pump. The hyperfine component that is not directly pumped presents either a peak (for $6S_{1/2}(F = 4) \rightarrow 6P_{1/2}(F = 4)$ or $6S_{1/2}(F = 3) \rightarrow 6P_{1/2}(F = 3)$ pumping) or a dip (for $6S_{1/2}(F = 4) \rightarrow 6P_{1/2}(F = 3)$ or $6S_{1/2}(F = 3) \rightarrow 6P_{1/2}(F = 4)$ pumping). Horizontal dashed line indicates the zero level. 103
4.19 Schematic of the experimental setup for the $6P_{1/2} \rightarrow nS_{1/2}, nD_{3/2}$ saturated absorption spectroscopy. 104
4.20 Normalized $6P_{1/2} \rightarrow 15D_{3/2}$ saturated absorption spectrum (black line) with Lorentzian fitted with linewidth ~ 26 MHz (red line). Signal amplitude is normalized to the non-resonant transmission probe power. Pump laser intensities: IR ~ 3 W/cm^2 and green ~ 2 W/cm^2, Green Probe intensity : 0.06 mW/cm^2. Cs vapor pressure ~ 7 mTorr. 105
4.21 Homogeneous linewidth measurement of $6P_{1/2} \rightarrow 15D_{3/2}$ saturated absorption spectra as a function of Caesium vapour pressure. The linear fit (dotted line) to the measurement values shows a linear growth of the homogeneous linewidth with Caesium vapour pressure and presents a slop of 2 GHz/Torr. 106

5.1 Normalized FMSR spectrum (black line) and velocity-selective absorption spectrum (grey line) for $6P_{1/2} \rightarrow 16S_{1/2}$ transition at vapour pressures of ~ 25 mTorr and ~ 0.075 mTorr respectively. Signal amplitudes are normalized to off-resonant reflected probe powers. Laser intensities: pump $\sim$ 35 mW/cm^2, probe ~ 100 mW/cm^2. Scan: time constant 300 ms. Horizontal dashed line: zero references for each spectrum. Vertical dashed lines: frequency reference from $6P_{1/2} \rightarrow 16S_{1/2}$ absorption in volume. 108
5.2 Comparison between a single $6P_{1/2} \rightarrow 16S_{1/2}$ FMSR spectrum (grey line) and FMSR spectra after averaging 170 scans (black line).Cs vapour pressure: ~ 25 mTorr. Signal amplitudes are normalized to off-resonant reflected probe powers. Horizontal dashed line: zero references for each spectrum. Vertical dashed lines: frequency reference from $6P_{1/2} \rightarrow 16S_{1/2}$ absorption in volume. 109

5.3 Comparison between FMSR lineshape in the absence of atom surface interaction i.e. C3 = 0 and γ = natural linewidth of the D_1 (black line) and experimentally obtained $6P_{1/2} \rightarrow 16S_{1/2}$ FMSR spectrum (Grey line). Signal amplitudes are normalized to off-resonant reflected power. Horizontal dashed line: zero references for each spectrum. Vertical dashed lines: frequency reference from $6P_{1/2} \rightarrow 16S_{1/2}$ absorption in volume. 110
5.4 Normalized $6P_{1/2} \rightarrow 15D_{3/2}$ FMSR spectra for two pump intensities: 17 mW/cm^2 (black line, multiplied by 1.5 times) and 35 W/cm^2 (grey line) at a vapour pressure of 10 mTorr. Signal amplitudes are normalized to the off-resonant reflected probe powers. Horizontal dashed line: zero references for each spectrum. Vertical dashed lines: frequency reference from $6P_{1/2} \rightarrow 16S_{1/2}$ absorption in volume. 111
5.5 Fitting of normalized $6P_{1/2} \rightarrow 16S_{1/2}$ FMSR spectrum (grey line) at a vapour pressure of 10 mTorr with infinite Doppler approximation model (black line) and Maxwell Boltzmann velocity distribution model (dash line). Signal amplitude is normalized to the off-resonant reflected probe power. Horizontal dashed line: zero references for each spectrum. Vertical dashed lines: frequency reference from $6P_{1/2} \rightarrow 16S_{1/2}$ absorption in volume. 112
5.6 Normalized theoretical lineshape for different combination of C_3 and γ values (a) different C_3 having same γ (b) same C_3 with different γ (c) two different combination of C_3 and γ having same C_3/γ ratio (0.08). The amplitude is normalized to the maximum amplitude of the signal. Horizontal dashed line: zero references for each spectrum. The vertical zero line indicates the atomic resonance frequency. 113
5.7 Fits of normalized $6P_{1/2} \rightarrow 16S_{1/2}$ FMSR spectra (obtained at Cs vapour pressure of $\sim$ 25 mTorr) with the theoretical lineshapes having different combinations of C_3 and γ values. FMSR signal amplitude is normalized to the off-resonant reflected probe power. Horizontal dashed line: zero references for each spectrum. Vertical dashed lines: frequency reference from $6P_{1/2} \rightarrow 16S_{1/2}$ absorption in volume. 115
5.8 3D contour plot of the least square error (Z-axis) mapped with colours with X-axis being C_3 (MHz μm^3) and Y-axis being γ (MHz) for (a) large component i.e. $6P_{1/2}(F = 3) \rightarrow 16S_{1/2}$) and (b) small component i.e. $6P_{1/2}(F = 4) \rightarrow 16S_{1/2}$). 116
5.9 Best fit (black line) for $6P_{1/2} \rightarrow 16S_{1/2}$ FMSR signal (grey line) for different caesium vapour pressure. FMSR signal amplitude is normalized to the off-resonant reflected probe powers. Horizontal dashed line: zero references for each spectrum. Vertical dashed lines: frequency reference from $6P_{1/2} \rightarrow 16S_{1/2}$ absorption in volume. 117
5.10 Best fit (black line) for $6P_{1/2} \rightarrow 17S_{1/2}$ FMSR signal (grey line) for different caesium vapour pressure. FMSR signal amplitude is normalized to the off-resonant reflected probe powers. Horizontal dashed line: zero references for each spectrum. Vertical dashed lines: frequency reference from $6P_{1/2} \rightarrow 17S_{1/2}$ absorption in volume. 118

5.11 Extracted C_3 values (in MHz μm^3) as a function of Cs vapour pressure (in mTorr) for $16S_{1/2}$ (left) and $17S_{1/2}$ (right) states. Grey dashed line: predicted C_3 value for a sapphire surface. Square marker: larger transition ($6P_{1/2}(F = 3) \rightarrow nS_{1/2}$). Triangle marker: small transition ($6P_{1/2}(F = 4) \rightarrow nS_{1/2}$). The grey-shaded area shows the uncertainty in C_3 measurements. 119
5.12 Extracted homogeneous linewidth γ (in MHz) for $16S_{1/2}$ and $17S_{1/2}$ states as a function of Cs vapour pressure. The dashed lines show the linear growth of the homogeneous linewidth. Triangle marker : small transition ($6P_{1/2}(F = 4) \rightarrow nS_{1/2}$),square marker: the larger transition ($6P_{1/2}(F = 3) \rightarrow nS_{1/2}$). 120
5.13 $6P_{1/2} \rightarrow 15D_{3/2}$ FMSR spectra for pump intensities: 12, 17, 25, and 35 mW/cm^2 & Cs vapour pressure: $\sim$ 25 mTorr. Signal amplitudes are normalized to off-resonant reflected probe powers. Horizontal dashed line: zero reference. Vertical dashed lines: frequency reference from $6P_{1/2} \rightarrow 15D_{3/2}$ absorption in volume. 121
5.14 $6P_{1/2} \rightarrow 15D_{3/2}$ FMSR spectra for pump intensities: 12, 17 and 25 mW/cm^2 & Cs vapour pressure: $\sim$ 10 mTorr. Signal amplitudes are normalized to off-resonant reflected probe powers. Horizontal dashed line: zero reference. Vertical dashed lines: frequency reference from $6P_{1/2} \rightarrow 15D_{3/2}$ absorption in volume. 122
5.15 Velocity-selective $6P_{1/2} \rightarrow nS_{1/2}, nD_{3/2}$ (n = 15 - 17) absorption spectra in a 1 cm cell at $\sim$ 0.08 mTorr Cs vapor pressure. The amplitudes of absorption signals are first normalized to off-resonant transmitted probe powers and then to the maximum amplitude of the $6P_{1/2} \rightarrow 15D_{3/2}$ transition with appropriate multiplication factors. Horizontal dashed line: zero reference. Vertical dashed lines: frequency reference from $6P_{1/2} \rightarrow nS_{1/2}, nD_{3/2}$ absorption in volume. 123
5.16 FMSR spectra for $6P_{1/2} \rightarrow 15D_{3/2}, 16S_{1/2}$ (black and red line respectively) at Cs vapour pressure: $\sim$ 20 mTorr & pump laser intensity: 35 mW/cm^2. FMSR signal amplitudes are normalized to the off-resonant reflected probe powers. Horizontal dashed line: zero references for each spectrum. Vertical dashed lines: frequency reference from $6P_{1/2} \rightarrow 15D_{3/2}, 16S_{1/2}$ absorption in volume. 124
5.17 Best fit (black line) for $6P_{1/2} \rightarrow 15D_{3/2}$ FMSR signal (grey line) for different caesium vapour pressure. FMSR signal amplitudes are normalized to the off-resonant reflected probe powers. Pump laser intensity: 17 mW/cm^2. Horizontal dashed line: zero references for each spectrum. Vertical dashed lines: frequency reference from $6P_{1/2} \rightarrow 15D_{3/2}$ absorption in volume. . . 125
5.18 Best fit (red line) for $6P_{1/2} \rightarrow 15D_{3/2}$ FMSR signal (grey line) for different caesium vapour pressure. FMSR signal amplitudes are normalized to the off-resonant reflected probe powers. Pump laser intensity: 12 mW/cm^2. Horizontal dashed line: zero references for each spectrum. Vertical dashed lines: frequency reference from $6P_{1/2} \rightarrow 15D_{3/2}$ absorption in volume. . . 126

5.19 Best fit (black line) for $6P_{1/2} \rightarrow 16D_{3/2}$ FMSR signal (grey line) for different caesium vapour pressure. FMSR signal amplitudes are normalized to the off-resonant reflected probe powers. Pump laser intensity: 17 mW/cm^2. Horizontal dashed line: zero references for each spectrum. Vertical dashed lines: frequency reference from $6P_{1/2} \rightarrow 16D_{3/2}$ absorption in volume. . . 127
5.20 Best fit (black line) for $6P_{1/2} \rightarrow 17D_{3/2}$ FMSR signal (grey line) for different caesium vapour pressure. FMSR signal amplitudes are normalized to the off-resonant reflected probe powers. Pump laser intensity: 17 mW/cm^2. Horizontal dashed line: zero references for each spectrum. Vertical dashed lines: frequency reference from $6P_{1/2} \rightarrow 17D_{3/2}$ absorption in volume. . . 128
5.21 Extracted C_3 values (in MHz μm^3) as a function of Cs vapour pressure (in mTorr) for $15D_{3/2}$ state (left) for pump intensities: 17 (black marker), 12 (red marker) mW/cm^2 and $16D_{3/2}$ (right) states for pump intensity 17 mW/cm^2 (black marker). Grey dashed line: predicted C_3 value for a sapphire surface. Triangle marker: small transition ($6P_{1/2}(F = 4) \rightarrow nD_{3/2}$). Square marker: larger transition ($6P_{1/2}(F = 3) \rightarrow nD_{3/2}$). The grey-shaded area shows the uncertainty in C_3 measurements. 129
5.22 Measured homogeneous linewidth, γ (in MHz) as a function of Cs vapour pressure for $15D_{3/2}$ and $16D_{3/2}$. Red and black marker indicates the measurement for a pump power of 12 and 17 mW/cm^2 respectively. Triangle marker indicates the small transition ($6P_{1/2}(F = 4) \rightarrow nD_{3/2}$) and square marker indicates the larger transition ($6P_{1/2}(F = 3) \rightarrow nD_{3/2}$). 130

6.1 Normalized $6P_{1/2} \rightarrow 16S_{1/2}$ thin cell transmission spectra for various cell thicknesses L at two caesium vapour pressures: $\sim$ 0.27 Torr (red line) and $\sim$ 0.025 Torr (blue line). Signal amplitudes are normalized to off-resonance probe powers and further normalized to the maximum amplitude of transmission spectra at 640 nm for $\sim$ 0.27 Torr Cs vapour pressure, the normalization factors are indicated with their respective colours. $\Delta\omega$ represents the redshift from the frequency reference (marked as 0). Horizontal lines indicate the zero level of each spectrum. 134
6.2 Tracing the shift (only the dip) of the $6P_{1/2} \rightarrow 16S_{1/2}$ thin cell transmission spectra as a function of cell thickness (L). The colour lines are C_3 predictions assuming the atom is placed in the middle of the cell ($C_3 \sim \Delta\omega L^3/16$). 135

List of Tables

2.1 C_3 coefficient (in MHz μm^3) for $15D_{3/2}$ and $16S_{1/2}$ states. 35
2.2 C_3 (in MHz μm^3) coefficient for $nS_{1/2}$ and $nD_{3/2}$ states where n = 15 - 18 along with transition wavelength from $6P_{1/2}$ level. 36
2.3 C_5 (in kHz μm^5) coefficient for for $15D_{3/2}$, $16S_{1/2}$ and $17P_{1/2}$ states. . . . 37
2.4 C_5 (in kHz μm^5) coefficient for $nS_{1/2}$ and $nD_{3/2}$ states where n = 15 - 18. 37
2.5 $C_{5,pT}$ coefficients for $15D_{3/2}$, $16S_{1/2}$ and $17P_{1/2}$ states. 39
2.6 Contribution to the C_3 coefficient (in kHz μm^3) of $6P_{1/2}$ from dipole virtual couplings considering a perfect reflector. The sign (-) signifies the coupling in emission. This calculation excludes the virtual couplings for which the contribution is less than 0.03 kHz μm^3. 42
2.7 Contribution to the C_3 coefficient (in kHz μm^3) of $16S_{1/2}$ from dipole virtual couplings considering a perfect reflector. The sign (-) signifies the coupling in emission. This calculation excludes the virtual couplings for which the contribution is less than 4 kHz μm^3. 42
2.8 Contribution to the C_3 coefficient (in kHz μm^3) of $15D_{3/2}$ from dipole virtual couplings considering a perfect reflector. The sign (-) signifies the coupling in emission. This calculation excludes the virtual couplings for which the contribution is less than 4 kHz μm^3. 43
2.9 C_3 coefficients for $nD_{3/2}, nS_{3/2}$ states where n = 15 - 18 considering a perfect reflecting surface. 43
2.10 C_3 coefficient for $nD_{3/2}, nS_{3/2}$ states where n = 15 - 18. 45

4.1 Accessible Rydberg states and their transition wavelength from $6P_{1/2}$ state. 83
4.2 Relative $6S_{1/2} \rightarrow 6p_{1/2}$ hyperfine transition strength factor S_{FF}. 102

5.1 Square of reduced dipole matrix elements $|\langle 6P_{1/2}|\mathrm{p}|nS_{1/2}, nD_{3/2}\rangle|^2$ transition where n= 15 - 17 normalized $|\langle 6P_{1/2}|\mathrm{p}|15D_{3/2}\rangle|^2$. 123

Chapter 1

Introduction

The interaction between atoms and macroscopic surfaces is a fundamental prediction of quantum electrodynamics of importance for precision measurements, quantum technologies and our understanding of the electromagnetic properties of materials. Atom-surface interactions were studied from the early 20^{th} century in the works of Lennard-Jones [1], described as the interaction between the fluctuating atomic dipole and its surface-induced image. In this case, the interaction energy is equal to $-C_3/z^3$, where z is the atom-surface separation and C_3 is the dipole-dipole interaction coefficient (also called the van der Waals coefficient) that depends on the atomic state as well as the dielectric properties of the surface. This description is only valid in the electrostatic limit when field propagation effects can be ignored (i.e. when $z << \lambda/4\pi$, where λ is the relevant atomic transition wavelength)

In their seminal work, Casimir and D. Polder [2] examined the atom-surface interaction in a different way, taking into account the effects of propagation. In their interpretation, the atom interacts with the vacuum fluctuations modified by the presence of a surface. For ground-state atoms, they calculated the atom-surface interaction energy for arbitrary atom-surface separations, demonstrating that in the far-field limit the energy scales as $-\alpha/\mathrm{z}^4$, where α is the atomic polarizability. Naturally, in the near field ($z << \lambda/4\pi$) the

interaction energy converges to the electrostatic limit. The predictions of Casimir and Polder were experimentally confirmed in the group of E. A Hinds [3] and subsequently by a number of other experiments. For this reason, the term "Casimir-Polder" has become a generic term for atom-surface interactions.

The fluctuations of the atomic dipole (quantum mechanical average over the atomic state) scale very rapidly with the atomic excitation. In the case of alkali atoms (with one external electron), the spread of the atomic wavefunction scales as n^{*2}, where $n^* = n - \delta$ is the effective quantum number (n is the principal quantum number and δ is the quantum defect), suggesting that dipole moment fluctuation scale as n^{*4}. For this reason, highly excited atoms (Rydberg atoms) are expected to present huge atom-surface interactions making them very good candidates for experimental atom-surface measurements (and measurements of dispersion forces in general).

Due to their strong interactions with their surrounding environment, Rydberg atoms also present strong collective effects [4][5], the most emblematic of which is the Rydberg blockade. For this reason, Rydberg atoms now find a renewed interest in quantum technology applications based on thin-cell devices [6]. Additionally, Rydberg states can be used for precision electrometry and imaging in the microwave [7][8] and terahertz [9] range. Hybridization of Rydberg atoms with photonic platforms [10][11] for technological applications requires a good understanding of their interactions with dielectric surfaces.

Previous studies of the Casimir-Polder effect have focused on the interaction of fluctuating dipoles, ignoring higher-order multipole terms. This is well justified for experiments involving ground state or low-lying excited atoms since the atomic size (smaller than 1 nm) is negligible compared to the probed atom-surface distances (typically 100nm for more). In the case of Rydberg atoms, the dipole approximation should be put into question, because the spread of the electron wavefunction, scaling as n^{*2}, can be as large as 100nm for relatively modest excitations with a principal quantum number $n \sim 35$.

Rydberg atoms are therefore an excellent system for studying higher-order interactions (quadrupole-quadrupole and octupole-dipole). Although some theoretical treatment of this subject already exist [12] [13], there is so far no experimental demonstration of multipole effects in Casimir-Polder interactions.

Rydberg-surface Casimir-Polder (CP) interaction was first measured with sodium atomic beams flying through a metallic cavity demonstrating the van der Waals law of interaction [14]. More recently, thin atomic vapour cells [15] or hollow fibre [16] have been used as platforms to probe Rydberg atoms close to the surface. However, experiments with high-lying rubidium Rydbergs (n= 32 - 43) [15] were not in agreement with Casimir-Polder theory, sparking closer theoretical studies of Rydberg-surface interactions.

In our group SAI (Spectroscopie Atomique aux Interfaces), we use a technique which is called selective reflection spectroscopy (SR) that probes atoms at a typical distance of about $\lambda/2\pi$ (here λ is the excitation wavelength) and allows the measurement of Casimir-Polder interactions of excited atoms using atomic vapour cells [17][18]. This technique has been extensively used to probe low-lying excited states at a nanometric distance from dielectric windows, measuring C_3 coefficients [19][20], as well as exploring the coupling of atoms with surface polaritons [21][22]. Previously in our group, nanometric thin cells (TC) [23] having a thickness ranging from 30 nm to 1µm have also been used to measure atom-surface interactions by confining atoms very close ($\sim$ 50 nm) to the surface.

This thesis aimed to probe Rydberg atoms close to a sapphire surface using both of these techniques. The caesium atoms are first excited by a strong pump laser to the first caesium resonance ($6P_{1/2}$) with a DBR laser at λ = 894 nm (pump laser) and subsequently the $6P_{1/2} \rightarrow nS_{1/2}, nD_{3/2}$ (n = 15 - 17) transition are probed with a tunable extended cavity laser at λ = 512 nm - 508 nm (probe). The setup is similar to the one described in [22]. The outline of this thesis is as follows:

- In the second chapter, we deal with the non-retarded Casimir-Polder interaction

between highly excited atoms and dielectric surfaces. In an electrostatic framework, we expand the calculation of the atom-surface energy beyond the dipole-dipole approximation calculating quadrupole-quadrupole and octupole-dipole terms that scale as $-C_5/z^5$. In this chapter, we provide explicit calculations of the C_3 and C_5 coefficients.

- In the third chapter, we present numerical calculations of selective reflection and thin cell spectra, accounting for the Maxwell-Boltzmann velocity distribution, bypassing the infinite Doppler approximation that was used up to now for calculating SR spectra. We subsequently use our numerical models in order to explore the effects of higher-order interactions in thin-cell and SR spectra.

- In the fourth chapter, we describe the experimental techniques (selective reflection and thin cell) used for measuring Rydberg-surface interactions.

- In the fifth chapter, we present the results of our SR experiment on $6P_{1/2} \rightarrow nS_{1/2}, nD_{3/2}$ (n = 15 - 17) transitions. A detailed analysis of the experimental spectra allows us to measure the Rydberg-surface interactions. We find that the experimental value of the C_3 coefficient exceeds theoretical predictions (by a factor of 1.5 or 2, depending on the probed state). We propose further experiments that could be performed in order to illuminate this disagreement.

- In the sixth chapter, we present our preliminary work on thin cell spectroscopy on Rydberg states.

Chapter 2

Non-retarded Casimir-Polder interactions between highly excited atom and dielectric surface

---

In this chapter, we describe the non-retarded Casimir-Polder interaction between a Rydberg atom and a dielectric surface at distances for which the atomic structure of the surface is negligible. The interaction between an atom and a surface perturbs the free atom Hamiltonian and shifts the atomic energy levels. In the non-retarded limit, these energy shifts are mostly governed by dipole-dipole (image) interaction which goes as $1/z^3$, where z is the distance between the atom and the surface. Highly excited atoms such as the Rydberg atoms undergo stronger interaction as the dipole moment fluctuations evolve as $(n^*)^4$ ($n^* = n - \delta_l$, n is the principal quantum number and δ_l is the quantum defected for given angular momentum quantum number l). On the other hand as the spread of the atomic wavefunction which evolves as $(n^*)^2$, becomes comparable to the atom surface separation (z), the contribution of higher-order terms (such as quadrupole-quadruple, dipole-octupole interaction and so on) starts to be non-negligible. Thus, corrections beyond the dipole-dipole approximation become important for predicting Rydberg atom-surface interactions.

In section 2.1, we build the theoretical framework for calculating the atom-surface interaction energies (for a perfect reflector) beyond the dipole-dipole approximation assuming an instantaneous correlation between the atom and its surface-induced image (electrostatic approximation). This approach allows us to quantify for the first time quadrupole-image quadrupole and dipole-image octopole atom-surface interactions.

In section 2.2, we calculate the external electron wavefunction for Rydberg atoms, considering an effective central potential. Using first-order perturbation theory, we subsequently calculate the energy shift of Rydberg states due to the atom-surface interactions.

In Section 2.3, we estimate the C_3 and C_5 coefficients for the caesium Rydberg states ($nS_{1/2}$, $nD_{3/2}$ n = 15 - 18) that are relevant in our experiments for an ideal reflecting surface. These results can be very easily extended to other alkali atoms.

In section 2.4, we briefly describe the QED calculation of dipole-dipole Casimir-Polder (CP) interactions in the near-field limit that allows us to account for the effects of surface dispersion (frequency-dependent dielectric constant). We compute the C_3 coefficient of Rydberg-surface interactions by decomposition in a sum of all allowed dipole couplings (from a given state). We demonstrate that for Rydberg atoms, whose major couplings lie in the far-infrared or microwave range, it is only the static value of the dielectric constant that plays a role in Casimir-Polder calculations and the effects of dispersion are negligible.

Used Symbols and Abbreviation:

Symbols (Atom)	**Abbreviation**	**Symbols (Image)**
$\rho(\mathbf{r})$	Charge distribution	$\rho^{im}(\mathbf{r}')$
q	Electric charge	q^{im}
p_i	Electric dipole moment	p_i^{im}
Q_{ij}	Electric quadrupole moment	Q_{ij}^{im}
T_{ijk}	Electric octupole moment	T_{ijk}^{im}

2.1 Method of Images: Interaction between a Rydberg atom and its surface-induced image

We consider that a Rydberg atom consists of only one outermost external electron orbiting around a positively charged core which includes the atomic nucleus and the electron cloud. In the electrostatic limit, the atom-surface interaction is then an electrostatic interaction between the atom and its surface-induced image. We represent the atom as a charge distribution $\rho(\mathbf{r})$ and the surface-induced image as $\rho^{im}(\mathbf{r}')$. The surface is taken as a perfect reflector ($\varepsilon \to -\infty$, where ε is relative permittivity), infinitely extended in x - y plane while z is the atom-surface separation and r is the separation between the atom and its image (Figure 2.1).

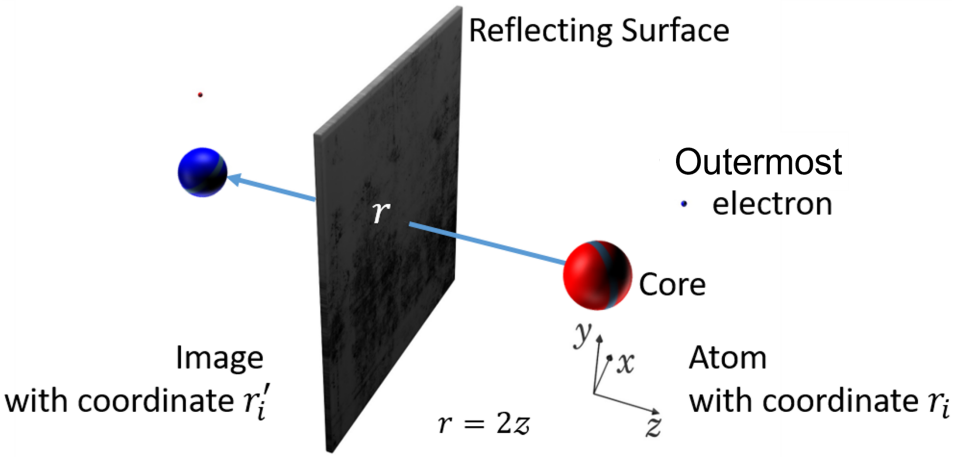

Figure 2.1: A Rydberg atom represented as a charge distribution $\rho(\mathbf{r})$ and its surface induced image $\rho^{im}(\mathbf{r}')$. The surface is on the x - y plane while z is the atom-surface separation and r is the separation between the atom and its image.

2.1.1 Multipole expansion of the potential

The interaction energy between the atom and the reflecting surface can be developed by considering the atom being placed in the external potential $\Phi^{im}(\mathbf{r})$ created by its surface-induced image. Performing a multipole expansion of the potential $\Phi^{im}(\mathbf{r})$ [24] and rewrite the potential in a compact format (using Einstein's summation notation and Gauss units),

we get:

$$\Phi^{im}(\mathbf{r}) = \frac{q^{im}}{r} + p_i^{im}\frac{r_i}{r^3} + \frac{1}{2}Q_{ij}^{im}\frac{r_i r_j}{r^5} + \frac{1}{6}T_{ijk}^{im}\frac{r_i r_j r_k}{r^7} + \dots$$

where,

- $q^{im} = \int \rho^{im}(\mathbf{r}')d^3r'$ is the image monopole moment (total charge).
- $p_i^{im} = \int r_i'\rho^{im}(\mathbf{r}')d^3r'$ is the image dipole moment.
- $Q_{ij}^{im} = \int \left(3r_i'r_j' - r'^2\delta_{ij}\right)\rho^{im}(\mathbf{r}')d^3r'$ is the image quadrupole moment.
- $T_{ijk}^{im} = \int \left[15r_i'r_j'r_k' - 3(\delta_{ij}r_k' + \delta_{ik}r_j' + \delta_{jk}r_i')r'^2\right]\rho^{im}(\mathbf{r}')d^3r'$ is the image octupole moment.

Here, we limit ourselves to the octupole term. Keeping in mind that the atom is neutral, we can omit the monopole term and write:

$$\begin{aligned}\Phi^{im}(\mathbf{r}) &= p_i^{im}\frac{r_i}{r^3} + \frac{1}{2}Q_{ij}^{im}\frac{r_i r_j}{r^5} + \frac{1}{6}T_{ijk}^{im}\frac{r_i r_j r_k}{r^7} + \dots \\ &= \Phi_p^{im}(\mathbf{r}) + \Phi_Q^{im}(\mathbf{r}) + \Phi_T^{im}(\mathbf{r}) + \dots\end{aligned} \tag{2.1}$$

(for details see appendix, equation 7.1)

where $\Phi_p^{im}(\mathbf{r})$, $\Phi_Q^{im}(\mathbf{r})$ and $\Phi_T^{im}(\mathbf{r})$ are the potential due to image dipole, quadrupole and octupole moment respectively.

2.1.2 Interaction energy between an atomic and its image (W)

The electrostatic interaction energy between the atom and the surface W can be calculated in the following form :

$$W = \frac{1}{2}\int \rho(\mathbf{r})\Phi^{im}(\mathbf{r})d^3r$$

As we consider the interaction between an atom and its surface-induced image, our calculation is only true in the region $z > 0$ i.e. the integration is only on half space. So we must multiply the interaction energy by a factor of $1/2$. If $\Phi^{im}(\mathbf{r})$ is a smooth (slowly varying) function over the region where $\rho(\mathbf{r})$ is non-negligible, we can expand this potential in the Taylor series by considering a suitably chosen origin (in our case it's around

the atomic itself) [24]. Restricting ourselves to the octupole term, the interaction energy can be decomposed as:

$$W = \underbrace{W_{pp^{im}}}_{\sim 1/r^3} + \underbrace{W_{pQ^{im}} + W_{Qp^{im}}}_{\sim 1/r^4} + \underbrace{W_{QQ^{im}} + W_{pT^{im}} + W_{Tp^{im}}}_{\sim 1/r^5} \tag{2.2}$$

(for details see appendix, equation 7.11)

where $W_{pp^{im}}$, $W_{pQ^{im}}$, $W_{Qp^{im}}$, $W_{QQ^{im}}$, $W_{pT^{im}}$, $W_{Tp^{im}}$ correspond to the interaction energy between atom-image: dipole-dipole, dipole-quadrupole, quadrupole-dipole, quadrupole-quadrupole, octupole-quadrupole, octupole-octupole respectively (batched together with their dependence over r). The atomic moments (dipole p_i, quadrupole Q_{ij} and octupole T_{ijk} moments) are linked to those of the image (p_i^{im}, Q_{ij}^{im}, T_{ijk}^{im}) by simple symmetry considerations that are illustrated in Figure 2.2.

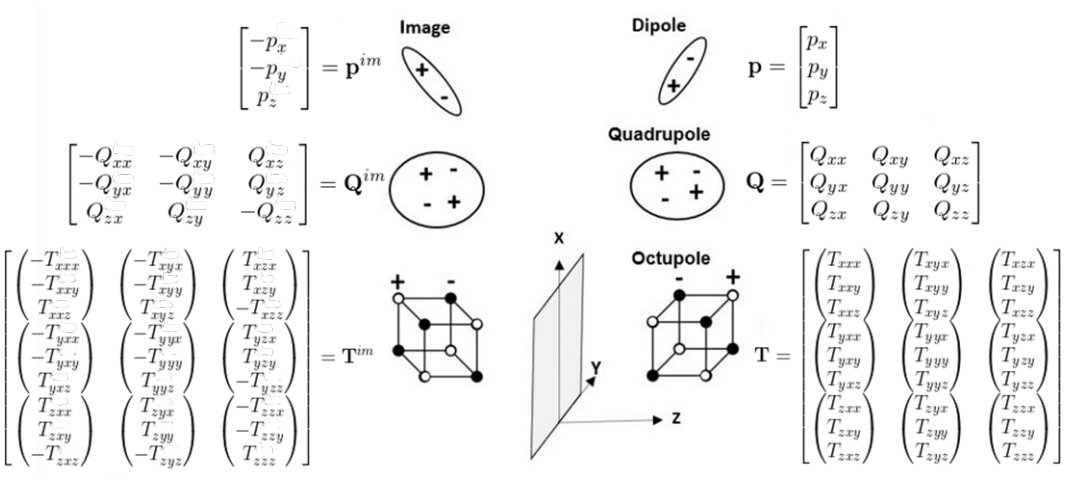

Figure 2.2: Elements of the electric dipole, quadrupole and octupole moment tensors of the atom and its surface induced image.

2.1.2.1 Interaction energy between an atomic dipole and an image dipole ($W_{pp^{im}}$)

We assume an atomic dipole $\mathbf{p}$ is placed in the field generated by its image dipole moment $\mathbf{p}^{im}$. The interaction energy $\mathbf{W}_{pp^{im}}$ can be obtained from equation 2.2, as (in vectorial

form):

$$W_{pp^{im}} = \frac{1}{2}\frac{\mathbf{p}\cdot\mathbf{p}^{im}}{r^3} - \frac{3}{2}\frac{(\mathbf{p}\cdot\mathbf{r})(\mathbf{p}^{im}\cdot\mathbf{r})}{r^5} \tag{2.3}$$

(for details see appendix, equation 7.4)

where $\mathbf{p}$ and $\mathbf{p}^{im}$ are the atomic dipole moment and its image dipole moment respectively. We can further simplify the expression, using the properties of symmetry described in figure 2.2 that links the elements of the image dipole moments (p_i^{im}) to the atomic dipole moment (p_i), as:

$$W_{pp}^{total} = W_{pp^{im}} = -\frac{1}{16z^3}\left[p^2 + p_z^2\right] \tag{2.4}$$

where $p^2 = p_x^2 + p_y^2 + p_z^2$.

Equation 2.4 gives the interaction energy between an atomic dipole and its image which evolves by $1/z^3$, where z is the atom surface separation.

2.1.2.2 Interaction energy between an atomic dipole and an image quadrupole ($W_{pQ^{im}}$)

Similarly, the interaction energy $W_{pQ^{im}}$ for placing an atomic dipole $\mathbf{p}$ in a field generated by its image quadrupole moment $\mathbf{Q}^{im}$ can be obtained as:

$$W_{pQ^{im}} = -\frac{5}{4}\frac{(\mathbf{p}\cdot\mathbf{r})(\mathbf{r}\cdot\mathbf{Q}^{im}\cdot\mathbf{r})}{r^7} + \frac{1}{2}\frac{\mathbf{p}\cdot\mathbf{Q}^{im}\cdot\mathbf{r}}{r^5} \tag{2.5}$$

(for details see appendix, equation 7.5)

where $\mathbf{p}$ and $\mathbf{Q}^{im}$ are the atomic dipole and the image quadrupole tensor respectively. Using the symmetry properties we rewrite the interaction terms in a Cartesian coordinate system :

$$W_{pQ^{im}} = \frac{1}{64z^4}\left[3p_zQ_{zz} + 2p_yQ_{yz} + 2p_xQ_{xz}\right] \tag{2.6}$$

where $Q_{xz}, Q_{yz}, Q_{zz}, ...$ are the components of the atomic quadrupole moment tensor.

2.1.2.3 Interaction energy between an atomic quadrupole and an image dipole ($W_{Qp^{im}}$)

The interaction energy for placing atomic quadrupole $\mathbf{Q}$ in a field of the image dipole $\mathbf{p}^{im}$ can be given by:

$$W_{Qp^{im}} = -\frac{1}{2}\frac{\mathbf{p}^{im}\cdot\mathbf{Q}\cdot\mathbf{r}}{r^5} + \frac{5}{4}\frac{(\mathbf{p}^{im}\cdot\mathbf{r})(\mathbf{r}\cdot\mathbf{Q}\cdot\mathbf{r})}{r^7} \tag{2.7}$$

(for details see appendix, equation 7.7)

The terms involving the interaction between an atomic dipole-image quadrupole moment ($W_{pQ^{im}}$) and the atomic quadrupole-image dipole moment ($W_{Qp^{im}}$) are the same due to the symmetry properties between the atom and image. Thus we add these two interactions:

$$\begin{aligned} W_{pQ}^{total} &= W_{pQ^{im}} + W_{Qp^{im}} \\ &= \frac{1}{32z^4}\left[3p_zQ_{zz} + 2p_yQ_{yz} + 2p_xQ_{xz}\right] \end{aligned} \tag{2.8}$$

2.1.2.4 Interaction energy between an atomic quadrupole and an image quadrupole ($W_{QQ^{im}}$)

For an atomic quadrupole $\mathbf{Q}$ placed in the field of its image quadrupole $\mathbf{Q}^{im}$, the interaction energy $W_{QQ^{im}}$ can be expressed as:

$$W_{QQ^{im}} = \frac{1}{12}\left[\frac{\mathrm{Tr}\left(\mathbf{Q}^{im}\cdot\mathbf{Q}\right)}{r^5} - 10\frac{\mathbf{r}\cdot\mathbf{Q}\cdot\mathbf{Q}^{im}\cdot\mathbf{r}}{r^7} + \frac{35}{2}\frac{(\mathbf{r}\cdot\mathbf{Q}^{im}\cdot\mathbf{r})(\mathbf{r}\cdot\mathbf{Q}\cdot\mathbf{r})}{r^9}\right] \tag{2.9}$$

(for details see appendix, equation 7.9)

Simplifying and rewriting the interaction in a Cartesian coordinate system we get:

$$W_{QQ}^{total} = W_{QQ^{im}} = -\frac{1}{768z^5}\left[17Q_{zz}^2 + 16Q_{zy}^2 + 16Q_{zx}^2 + 2Q_{xx}^2 + 4Q_{yx}^2 + 2Q_{yy}^2\right] \tag{2.10}$$

Equation 2.10 shows us the interaction energy between an atomic quadrupole and its image which evolves by $1/z^5$.

2.1.2.5 Interaction energy between an atomic dipole and an image octupole ($W_{pT^{im}}$)

The interaction energy $W_{pT^{im}}$, between an atomic dipole **Pp** and the image octupole $\mathbf{T}^{im}$ is given by:

$$W_{pT^{im}} = \frac{1}{12}\left[\frac{3p_i(\mathbf{r}\cdot\mathbf{T}_i^{im}\cdot\mathbf{r})}{2r^7} - 7\frac{(\mathbf{p}\cdot\mathbf{r})(\mathbf{r}\cdot\mathbf{T}_i^{im}\cdot\mathbf{r})r_i}{2r^9}\right] \tag{2.11}$$

where the matrices $\mathbf{T}_i^{im}$ are defined as $(\mathbf{T}_i^{im})_{jk} = T_{ijk}^{im}$.

The interaction in the Cartesian coordinate system can be described as:

$$W_{pT^{im}} = -\frac{1}{384z^5}\left[3p_xT_{xzz} + 3p_yT_{yzz} + p_zT_{zzz}\right] \tag{2.12}$$

where

p_x,p_y, and p_z are the components of the atomic dipole moment.

T_{zxz},T_{yzz},T_{zzz}, ... are the components of the octupole moment tensor.

Equation 2.12 shows the interaction energy between a dipole and its image octupole also goes by $1/z^5$ similar to the quadrupole-quadrupole interaction term.

2.1.2.6 Interaction energy between an atomic octupole and an image dipole ($W_{Tp^{im}}$)

Similarly, the interaction energy $W_{Tp^{im}}$ between an atomic octupole **T** and the image dipole $\mathbf{p}^im$ is given by:

$$W_{Tp^{im}} = \frac{1}{12}\left[\frac{3(\mathbf{r}\cdot\mathbf{T}_i\cdot\mathbf{r})p_i^{im}}{2r^7} - 7\frac{r_i(\mathbf{r}\cdot\mathbf{T}_i\cdot\mathbf{r})(\mathbf{p}^{im}\cdot\mathbf{r})}{2r^9}\right] \tag{2.13}$$

Due to symmetry properties, the terms involved in the interaction between dipole-image octupole and octupole-image dipole terms are similar (in cartesian coordinates). Thus, we add these interactions, as:

$$\begin{aligned} W_{pT}^{total} &= W_{pT^{im}} + W_{Tp^{im}} \\ &= -\frac{1}{192z^5}\left[3p_xT_{xzz} + 3p_yT_{yzz} + p_zT_{zzz}\right] \end{aligned} \tag{2.14}$$

2.2 Calculation of the atom-surface interaction coefficients (C_3, C_4, C_5)

The atom-surface interaction perturbs the free atom Hamiltonian and induces an energy shift that can be calculated using first-order perturbation theory. Using the interaction energies that we calculated in the previous section (Equations 2.2), we can express the frequency shift of an atomic level Δf in terms of the interaction coefficients as:

$$\Delta f = \frac{1}{h}\langle\psi_{n,j,m_j}|W|\psi_{n,j,m_j}\rangle = -\frac{C_3}{z^3} - \frac{C_4}{z^4} - \frac{C_5}{z^5} \tag{2.15}$$

where C_3, C_4 and C_5 are the interaction coefficients for dipole-image dipole, dipole-image quadrupole and quadrupole-image quadrupole or dipole-image octupole interaction coefficients.

The quantum state of the electron is expressed as:

$$|\psi_{n,j,m_j}\rangle \equiv \sum_{m_l,m_s} \mathrm{c}^{l,s,j}_{m_l,m_s,m_j} \frac{u_{n,l}(r)}{r} \mathrm{Y}_{l,m_l}(\theta,\phi)\chi(s)$$

where

$u_{n,l}(r)$ represents the radial wavefunction

$\mathrm{Y}_{l,m_l}(\theta,\phi)$ represents spherical harmonics

$\mathrm{c}^{l,s,j}_{m_l,m_s,m_j}$ are the corresponding Clebsch–Gordan coefficients

$\chi(s)$ represents the wavefunction for spin

For the solution of the radial part of the wavefunction, we use the Numerov method [25][26]. The radial wavefunction of the Rydberg atom is represented with the time-independent Schrodinger's equation for a hydrogen-like atom assuming that there is only one outermost electron which orbits around a positively charged core consisting of the nucleus and negatively charged electron cloud. The Coulomb interactions between the

electrons are also neglected. In this context, Schrodinger's equation can be expressed as:

$$-\frac{\hbar}{2m_e}\frac{d^2}{d^2r}u_{n,l}(r)+\left[\frac{\hbar^2}{2m_e}\frac{l(l+1)}{r^2}-\frac{e^2}{r}V_l(r)-E\right]u_{n,l}(r)=0 \tag{2.16}$$

where

m_e is the mass of the electron.

$\hbar$ is the reduced planks constant.

l is the orbital quantum number.

$E = h.R_H/n^{*2}$, the energy of the state taking into account the quantum defect ($n^* = n-\delta_l$ is the effective quantum number, R_H is Rydberg constant) [27].

$V_l(r)$ is the modified central potential, which depends on the orbital angular momentum of the valence electron and also takes into account the effect of the static polarizability of the core electron cloud [28].

Figure 2.3 shows the square of radial wavefunction $|u(r/a_0)|^2$ as a function of the (r/a_0), where a_0 is the Bohr radius (in SI) for the $16S_{1/2}$ (solid line) and $18D_{3/2}$ (dash line) states.

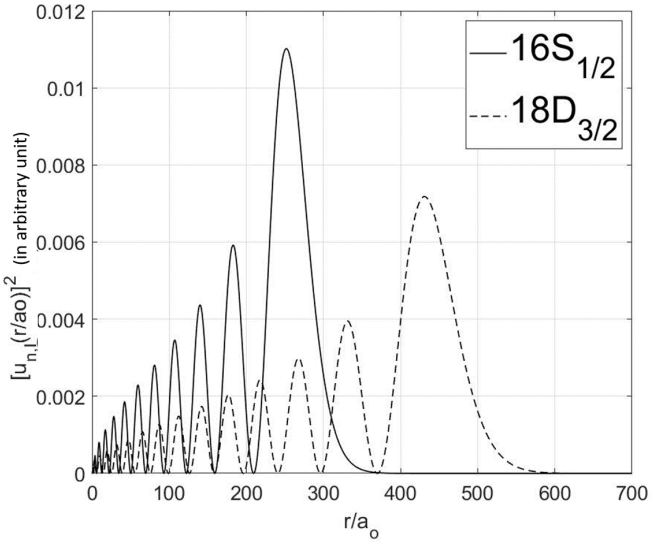

Figure 2.3: $|u(r/a_o)_{n,l}|^2$ (in arbitrary units) as function of r/a_o, where $[u(r/a_o)_{n,l}]$ is the radial wavefunction and a_o is the Bohr radius (in m^{-1}).

For the solution of the angular part of the wavefunction, we decompose the angular part of the wavefunction in the linear combination of the spherical harmonics with their corresponding Clebsch–Gordan coefficients. Below we show the decomposition of $S_{1/2}$, $P_{1/2}$ and, $D_{3/2}$ levels for all the possible degenerated states [29]:

- For state $S_{1/2}$

$$\mathcal{Y}_{l=0,s=1/2,j=1/2}(\theta,\phi) : \underbrace{C^{0,1/2,1/2}_{0,1/2,1/2}\mathrm{Y}_{0,0}(\theta,\phi)\chi(s_+)}_{m_j=1/2}$$
$$: \underbrace{C^{0,1/2,1/2}_{0,-1/2,-1/2}\mathrm{Y}_{0,0}(\theta,\phi)\chi(s_-)}_{m_j=-1/2}$$

- For state $\mathrm{P}_{1/2}$

$$\mathcal{Y}_{L=1,S=1/2,j=1/2}(\theta,\phi) : \underbrace{C^{1,1/2,1/2}_{0,1/2,1/2}\mathrm{Y}_{1,0}(\theta,\phi)\chi(s_+) + C^{1,1/2,1/2}_{1,-1/2,1/2}\mathrm{Y}_{1,1}(\theta,\phi)\chi(s_-)}_{m_j=1/2}$$
$$: \underbrace{C^{1,1/2,1/2}_{-1,1/2,-1/2}\mathrm{Y}_{1,-1}(\theta,\phi)\chi(s_+) + C^{1,1/2,1/2}_{0,-1/2,-1/2}\mathrm{Y}_{1,0}(\theta,\phi)\chi(s_-)}_{m_j=-1/2}$$

- For state $\mathrm{D}_{3/2}$

$$\mathcal{Y}_{l=2,s=1/2,j=3/2}(\theta,\phi) : \underbrace{C^{2,1/2,3/2}_{2,-1/2,3/2}\mathrm{Y}_{2,2}(\theta,\phi)\chi(s_-) + C^{2,1/2,3/2}_{1,1/2,3/2}\mathrm{Y}_{2,1}(\theta,\phi)\chi(s_+)}_{m_j=3/2}$$
$$: \underbrace{C^{2,1/2,3/2}_{1,-1/2,1/2}\mathrm{Y}_{2,1}(\theta,\phi)\chi(s_-) + C^{2,1/2,3/2}_{0,1/2,1/2}\mathrm{Y}_{2,0}(\theta,\phi)\chi(s_+)}_{m_j=1/2}$$
$$: \underbrace{C^{2,1/2,3/2}_{0,-1/2,-1/2}\mathrm{Y}_{2,0}(\theta,\phi)\chi(s_-) + C^{2,1/2,3/2}_{-1,1/2,-1/2}\mathrm{Y}_{2,-1}(\theta,\phi)\chi(s_+)}_{m_j=-1/2}$$
$$: \underbrace{C^{2,1/2,3/2}_{-1,-1/2,-3/2}\mathrm{Y}_{2,-1}(\theta,\phi)\chi(s_-) + C^{2,1/2,3/2}_{-2,1/2,-3/2}\mathrm{Y}_{2,-2}(\theta,\phi)\chi(s_+)}_{m_j=-3/2}$$

The separation between these magnetic sub-levels of the excited Rydberg states is very small in the order of a few MHz [30][31][32][33]. Thus, considering a spherical symmetry, we perform an averaging over all the m_j sub-levels of a given state and estimate the expectation value of $\langle\psi_{n,J,m_J}|W|\psi_{n,J,m_J}\rangle$.

2.2.1 Dipole-dipole (image) interactions coefficient (C_3)

The frequency shift due to the dipole-dipole (image) interaction for a given atomic state $|\psi_{n,J,m_J}\rangle$ can be calculated as:

$$\Delta f_{pp} = -\frac{1}{z^3}\frac{\langle\psi_{n,J,m_J}|p^2|\psi_{n,J,m_J}\rangle + \langle\psi_{n,J,m_J}|p_z^2|\psi_{n,J,m_J}\rangle}{16h}$$

$$\Delta f_{pp} = -\frac{\mathrm{C}_3}{z^3} \tag{2.17}$$

where C_3 is the coefficient of dipole-dipole interaction (van der Waals coefficient).

From equation 2.17, the coefficient of dipole-dipole (image) interaction, C_3 can be given as :

$$C_3 = \frac{\langle \psi_{n,J,m_J} | p^2 | \psi_{n,J,m_J} \rangle + \langle \psi_{n,J,m_J} | p_z^2 | \psi_{n,J,m_J} \rangle}{16h} \tag{2.18}$$

To separate the contribution of the radial and angular parts of the wave function, we rewrite the dipole-dipole (image) interaction terms (equation 2.4) in spherical coordinates using $x = r\sin\theta\cos\phi$, $y = r\sin\theta\sin\phi$ and $z = r\cos\theta$, as:

$$p^2 + p_z^2 = e^2 r^2 (1 + \cos^2\theta)$$

where e is the electric charge.

Separating the radial and angular parts of the wavefunction, the dipole-dipole (image) interaction coefficient is given by:

$$C_3 = \frac{e^2}{16}\left(C_3^{radial} C_3^{angular}\right) \tag{2.19}$$

where

$C_3^{radial} = \int_0^\infty r^2 |R(r)|^2 r^2 dr = \int_0^\infty r^2 |u(r)|^2 dr$ is the contribution for the radial part of the wavefunction.

$C_3^{angular} = \int_0^\pi \int_0^{2\pi} [1+\cos^2(\theta)]\sin(\theta) |\mathcal{Y}_{l,s,j,m_j}(\theta,\phi)|^2 d\theta d\phi$ is the contribution for the angular part of the wavefunction.

2.2.2 Dipole-quadrupole (image) interactions coefficient (C_4)

Using Equation 2.8, the frequency shift due to dipole-quadrupole (image) interactions can be written as follows:

$$\Delta f_{pQ} = -\frac{1}{z^4}\frac{\langle \psi_{n,J,m_J} | 3p_z Q_{zz} + 2p_y Q_{yz} + 2p_x Q_{xz} | \psi_{n,J,m_J} \rangle}{32h}$$

$$\Delta f_{pQ} = -\frac{C_4}{z^4} \tag{2.20}$$

where C_4 is the coefficient of dipole-quadrupole interaction.

Separating the contribution of the radial and angular parts, we can write:

$$C_4 = \frac{e^2}{32}\left(C_4^{radial} C_4^{angular}\right) \tag{2.21}$$

where

$C_4^{radial} = \int_0^\infty r^3 |R(r)|^2 r^2 dr = \int_0^\infty r^3 |u(r)|^2 dr$ is the contribution for the radial part of the wavefunction.

$C_4^{angular} = \frac{3}{128}\int_0^\pi \int_0^{2\pi} [7\cos(\theta) + 3\cos(3\theta)]\sin(\theta)|\mathcal{Y}_{l,s,j,m_j}(\theta,\phi)|^2 d\theta d\phi$ is the contribution for the angular part of the wavefunction.

Due to the symmetries of $\sin(\theta)$ and $\cos(\theta)$ functions the $C_4^{angular}$ coefficient is zero for all $|\psi_{n,J,m_J}\rangle$ atomic states. The selection rule for an electric dipole transition is $\Delta l = \pm 1$ (l is an orbital quantum number) and for an electric quadrupole transition is $\Delta l = 0, \pm 2$. There is no possibility of overlap for an excitation channel between a dipole and quadrupole transition. So, without any further development, we say:

$$C_4 = 0$$

2.2.3 Quadrupole-quadrupole (image) and dipole-octupole (image) interactions coefficient (C_5)

The quadrupole-quadrupole (image) and dipole-octupole (image) interactions have the same z dependence, therefore, we put both of these interactions under the umbrella of the same coefficient C_5.

Using equation 2.10, the energy shift due to quadrupole-quadrupole (image) interaction can be obtained as:

$$\Delta f_{QQ} = -\frac{1}{z^5}\frac{\langle\psi_{n,J,m_J}|17Q_{zz}^2 + 16Q_{zy}^2 + 16Q_{zx}^2 + 2Q_{xx}^2 + 4Q_{yx}^2 + 2Q_{yy}^2|\psi_{n,J,m_J}\rangle}{768h}$$

$$\Delta f_{QQ} = -\frac{C_5^{QQ}}{z^5} \tag{2.22}$$

where C_5^{QQ} is the coefficient of quadrupole-quadrupole (image) interaction.

The radial and angular contributions can be separated in a spherical coordinate as:

$$C_5^{QQ} = \frac{e^2}{768}\left(C_{5,QQ}^{radial} C_{5,QQ}^{angular}\right) \tag{2.23}$$

where

$C_{5,QQ}^{radial} = \int_0^\infty r^4 |u(r)|^2 dr$ is the contribution for the radial part of the wave function.

$C_{5,QQ}^{angular} = \frac{3}{2048}\int_0^\pi \int_0^{2\pi} [(41 + 20\cos(2\theta) + 3\cos(4\theta))]\sin(\theta)\mathcal{Y}_{l,s,j,m_j}(\theta,\phi)|^2 d\theta d\phi$ is the contribution for the angular part of the wavefunction.

Similarly, from equation 3.14 and 2.22 the coefficient of dipole-octupole (image) interaction can be expressed as:

$$C_5^{pT} = \frac{\langle \psi_{n,J,m_J} | 3p_x T_{xzz} + 3p_y T_{yzz} + p_z T_{zzz} | \psi_{n,J,m_J} \rangle}{192h} \tag{2.24}$$

where T_{zzz},T_{xzz},T_{yzz} are the components of the octupole moment operator.

After separating the radial and angular contributions, the dipole-image octupole interaction coefficient is given by:

$$C_5^{pT} = \frac{e^2}{512}\left(C_{5,pT}^{radial} C_{5,pT}^{angular}\right) \tag{2.25}$$

where

$C_{5,pT}^{radial} = \int_0^\infty r^4 |u(r)|^2 dr$ is the contribution for the radial part of the wave function.

$C_{5,pT}^{angular} = \frac{1}{512}\int_0^\pi \int_0^{2\pi} [44\cos(2\theta) + 5(3 + \cos(4\theta))]\sin(\theta)|\mathcal{Y}_{l,s,j,m_j}(\theta,\phi)|^2 d\theta d\phi$ is the contribution for the angular part of the wavefunction.

2.3 Evaluation of the interaction coefficient for relevant Rydberg states

---

Experimentally we probe $Cs(nS_{1/2}, nD_{3/2})$ states with set-wise excitation, pumping for

ground Cs($6S_{1/2} \rightarrow 6P_{1/2}$) with 894 nm laser and subsequently probing form Cs($6P_{1/2} \rightarrow nS_{1/2}, nD_{3/2}$) with an extended cavity laser 507 - 513 nm laser (shown in figure 2.4).

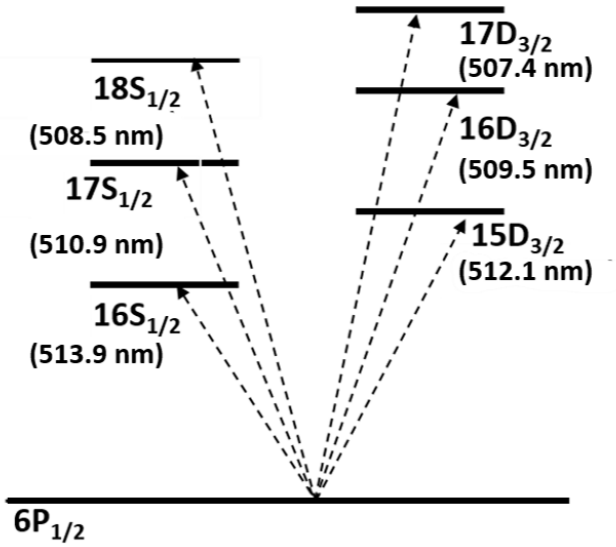

Figure 2.4: Accessible Rydberg states Cs($nS_{1/2}, nD_{3/2}$) from the first excited state Cs($6P_{1/2}$).

2.3.1 Evaluation of dipole-dipole (image) interaction coefficient (C_3)

Using equation 2.19, the radial and angular contributions of C_3 are calculated independently for all the degenerate m_j states and subsequently an isotropic averaging is performed (table 2.1 and 2.2).

Atomic State	m_j sub levels	$C_3^{angular}/16$	C_3^{radial}(m^3)	C_3 (MHz μm^3)	C_3 value Avg. overall m_j (in MHz μm^3)
$15D_{3/2}$	3/2	3/40	1.68×10^{-16}	4.39	**4.88**
	1/2	11/120		5.37	
	-1/2	11/120		5.37	
	-3/2	3/40		4.39	
$16S_{1/2}$	1/2	1/12	1.45×10^{-16}	4.14	**4.14**
	-1/2	1/12		4.14	

Table 2.1: C_3 coefficient (in MHz μm^3) for $15D_{3/2}$ and $16S_{1/2}$ states.

Atomic state	Effective principal quantum number $n^* = n - \delta$	Transition wavelength from $6P_{1/2}$ λ_{if} in μm	Value of C_3 for ideal reflector in MHz μm^3
$16S_{1/2}$	11.95	0.513884	4.14
$15D_{3/2}$	12.52	0.512068	4.88
$17S_{1/2}$	12.95	0.510887	5.71
$16D_{3/2}$	13.52	0.509469	6.66
$18S_{1/2}$	13.95	0.508537	7.69
$17D_{3/2}$	14.52	0.507407	8.88

Table 2.2: C_3 (in MHz μm^3) coefficient for $nS_{1/2}$ and $nD_{3/2}$ states where n = 15 - 18 along with transition wavelength from $6P_{1/2}$ level.

Figure 2.5 shows the expected linear growth of C_3 values over n^{*4}. nS, nP and nD states are indicated with square, circle and triangle markers respectively. C_3 coefficient has an exclusively dependence on n* and can be approximated as $C_3 \sim \alpha \times (\mathrm{n}^*)^4$ MHz μm^3, where $\alpha \approx 2.08 \times 10^{-4}$

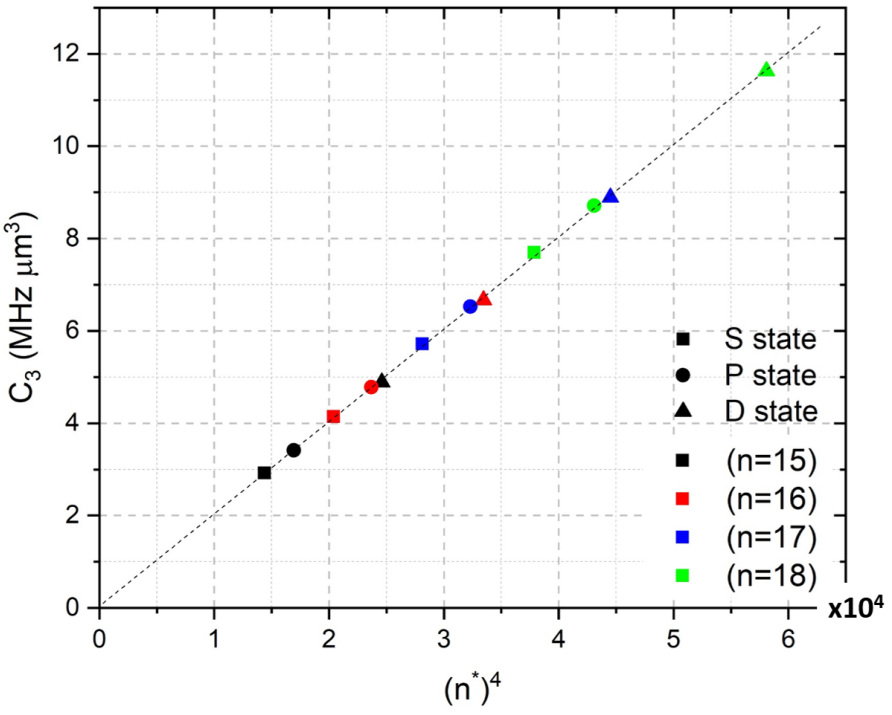

Figure 2.5: C_3 (in MHz μm^3) as function of n^{*4}. nS, nP and nD states are indicated by square, circle and triangle respectively (n is the principal quantum number).

2.3.2 Evaluation of quadrupole-quadrupole (image) interaction coefficient (C_5^{QQ})

Similarly, using equation 2.23, the radial and angular parts contributions C_5^{QQ} for all m_j sub-levels are calculated followed by an isotopic averaging (table 2.3 and 2.4).

State	m_j sub levels	$C_5^{angular}/768$	C_5^{radial}(m^5)	C_5^{QQ} (kHz μm^5)	Avg. over all m_j sub levels (in kHz μm^5)
$15D_{3/2}$	3/2	3/70	3.620×10^{-32}	0.5389	0.6303
	1/2	2/35		0.7185	
	-1/2	2/35		0.7185	
	-3/2	3/70		0.5389	
$16S_{1/2}$	1/2	1/20	2.5970×10^{-32}	0.4510	0.4510
	-1/2	1/20		0.4521	
$17P_{1/2}$	1/2	1/20	6.4261×10^{-32}	1.1160	1.1160
	-1/2	1/20		1.1187	

Table 2.3: C_5 (in kHz μm^5) coefficient for for $15D_{3/2}$, $16S_{1/2}$ and $17P_{1/2}$ states.

Atomic State	Effective principal quantum number $n^* = n - \delta$	Value of C_5^{QQ} for an ideal reflector in kHz μm^5	Atomic State	Effective principal quantum number $n^* = n - \delta$	Value of C_5^{QQ} for a ideal reflector in kHz μm^5
$15D_{3/2}$	12.52	0.6303	$15S_{1/2}$	10.95	0.2252
$16D_{3/2}$	13.52	1.1707	$16S_{1/2}$	11.95	0.4521
$17D_{3/2}$	14.52	2.0791	$17S_{1/2}$	12.95	0.8586
$18D_{3/2}$	15.52	3.5523	$18S_{1/2}$	13.95	1.5548

Table 2.4: C_5 (in kHz μm^5) coefficient for $nS_{1/2}$ and $nD_{3/2}$ states where n = 15 - 18.

Figure 2.6 shows the linear growth of C_5 with n^{*8}. nS, nP, and nD states are indicated

with square, circle, and triangle markers respectively with different colours for different n quantum numbers. C_5 coefficient also has an exclusive dependence over n^* and can be can approximate as $C_5 \sim \beta \times n^{*8}$ kHz μm^5 where $\beta \approx 1.08 \times 10^{-9}$. A rigorous analytical solution considering not only the principal quantum number (n) but also the angular quantum number (l) for estimating the C_5 has been calculated but this is excluded from the extent of this thesis.

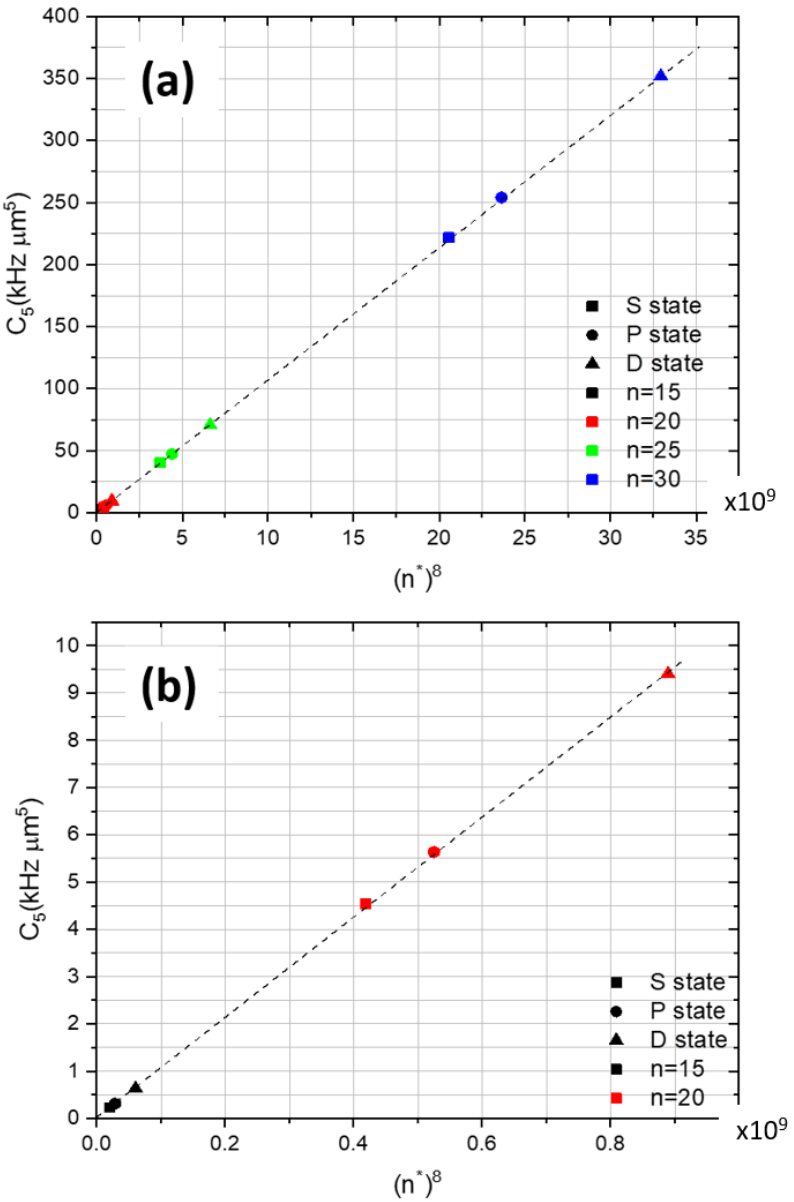

Figure 2.6: C_5 as a function of $(n^*)^8$. (a) nS, nP, and nD states are indicated by square, circle, and triangle respectively and different colours for different n quantum numbers. (b) enlarged plot for n = 15 and 20 (n is the principal quantum number).

2.3.3 Evaluation of dipole-octupole (image) interaction coefficient ($C_{5,pT}$)

Using equation 2.25, we calculate the dipole-octupole interaction coefficient, $C_{5,pT}$ (table 2.5).

State	m_j sub levels	$C_5^{angular}/512$	$C_5^{radial}(\mathrm{m}^5)$	C_5^{pT} (kHz $\mu\mathrm{m}^5$)	Avg. over all m_j sub levels
$15\mathrm{D}_{3/2}$	3/2	-3/140	3.620×10^{-32}	-0.2694	0.0
	1/2	3/140		0.2694	
	-1/2	3/140		0.2694	
	-3/2	-3/140		-0.2694	
$16\mathrm{S}_{1/2}$	1/2	0	2.5970×10^{-32}	0.0	0.0
	-1/2	0		0.0	
$17\mathrm{P}_{1/2}$	1/2	0	6.4261×10^{-32}	0.0	0.0
	-1/2	0		0.0	

Table 2.5: $C_{5,pT}$ coefficients for $15D_{3/2}$, $16S_{1/2}$ and $17P_{1/2}$ states.

The selection rule for an electric dipole-dipole transition is $\Delta l = \pm 1$ and for an octupole-octupole transition, it is $\Delta l = \pm 1, \pm 3$. Thus, there exist possible excitation channels through which an atom can be excited with a quadrupole transition and relaxation can occur through a dipole transition. In table 2.5, we see that the contribution of the dipole-octupole interaction term is non-zero for individual magnetic sub-levels for an anisotropic state such as $D_{3/2}$ but averages to zero for an isotropic averaging. Decomposing the states to their hyperfine structure can provide us with further information (not included here) about the anisotropic behaviour of dipole-octupole interactions and it is a matter of further investigation.

Up to this point, we have only considered a perfect reflector, whereas, in our experiments, we typically probe atoms close to dielectric windows, such as sapphire or glass. In this case,

the dielectric constant becomes a function of frequency (material dispersion). Therefore, to include the effect of a dispersive surface, atom-surface interactions should be calculated using the QED description. In the following section, we utilize the Casimir-Polder (CP) formulation (within the near-field approximation) to calculate the dipole-dipole (image) interaction C_3 coefficient for Rydberg atoms interacting with dielectric surfaces.

2.4 Casimir-Polder (CP) formulation in the non-retared limit to estimate the dipole-dipole (image) interaction coefficient

---

2.4.1 For an ideal reflector

The Casimir-Polder formulation for calculating the atom-surface induced energy shift is well established and has been used in numerous works [14][34][35][2][36][37]. We therefore skip the discussion on the specific details of the calculations. We consider an isotropic atomic state for which $p_x^2 = p_y^2 = p_z^2 = p/3$. The induced shift in the energy level due to dipole-image dipole interaction for a perfect reflector can be expressed as (in S.I. unit):

$$\Delta f_a = -\frac{1}{(2\pi\hbar)}\frac{1}{12z^3}\langle\psi_{n_i,j,m_j}|p^2|\psi_{n_i,j,m_j}\rangle \tag{2.26}$$

where $\hbar$ is the reduced Planck's constant.

With the expansion $\mathrm{I} = \sum_f |\psi_{n_f,j_f,m_j}\rangle\langle\psi_{n_f,j_f,m_j}|$, (I is the identity operator), we can write:

$$\langle\psi_{n_i,j,m_j}|p^2|\psi_{n_i,j,m_j}\rangle = \sum_f \langle\psi_{n_i}|p^2|\psi_{n_f}\rangle\langle\psi_{n_f}|p^2|\psi_{n_i}\rangle = \sum_f |\langle\psi_{n_i}|p|\psi_{n_f}\rangle|^2 \tag{2.27}$$

where

$\langle\psi_{n_i}|p|\psi_{n_f}\rangle = \langle\psi_{n_i,j_i,m_j}|p|\psi_{n_f,j_f,m_j}\rangle$ is the reduced dipole matrix element.

$|\psi_{n_i,j_i,m_j}\rangle$ is the initial atomic state.

$|\psi_{n_f,j_f,m_j}\rangle$ is the final atomic state.

Using the Wigner–Eckart theorem and the property of the Clebsch–Gordan coefficients, the average shift for the m_J sub-levels can be expressed as [29][38]:

$$\Delta f_i = -\frac{1}{(2\pi\hbar)12z^3} \cdot \frac{1}{2j_i+1} \sum_f |\langle\psi_{n_i}|p|\psi_{n_f}\rangle|^2 \tag{2.28}$$

$$\Delta f_i = -\frac{C_3}{z^3}$$

By knowing the atomic transition probability for $n_i \to n_f$ transition, we can obtain the matrix element $\langle\psi_{n_i}|p|\psi_{n_f}\rangle$ or vise-versa:

$$A_{i\to f} = \frac{4}{3\hbar}\frac{k_{if}^3}{2j_>+1}|\langle\psi_{n_i}|p|\psi_{n_f}\rangle|^2 \tag{2.29}$$

where

$k_{if} = \frac{2\pi}{\lambda_{i\to f}}$ and $\lambda_{i\to f}$ is the transition wavelength for the transition $|\psi_{n_i}\rangle \to |\psi_{n_f}\rangle$.

$A_{i\to f}$ is the spontaneous emission rate.

$j_> = j_f$ if $E_{n_f} > E_{n_i}$, or else $j_> = j_i$. Comparing Equations 2.28 and 2.29, we define the dipole-dipole interaction the coefficient, C_3^i as:

$$C_3^i = \sum_j \left(\frac{2j_>+1}{2j_i+1}\right)\frac{A_{i\to f}\lambda_{if}^3}{256\pi^4} \tag{2.30}$$

For example, the spectroscopic shifts of the atomic resonance for probing the $6P_{1/2} \to 15_{3/2}$ transition will be related to the difference between the CP shifts between the initial and probed states:

$$\Delta f_{6P_{1/2}\to 15D_{3/2}} = \frac{C_3^{15D_{3/2}}}{z^3} - \frac{C_3^{6P_{1/2}}}{z^3} \tag{2.31}$$

Tables 2.6, 2.7 and 2.8 below show the most influential virtual couplings for the $6P_{1/2}$, $16S_{1/2}$ and $15D_{3/2}$ atomic states respectively with their individual contributions to the overall C_3 coefficient for a perfect reflecting surface. The transition probabilities of the individual couplings and the dipole matrix elements are sourced from [39] [40][41].

$6P_{1/2}$	Wavelength λ_{ij} in µm	Transition rate A_{if} 10^6 in s^{-1}	$\frac{2J_>+1}{2J_i+1}$	Value C_3 for ideal reflector in kHz μm^3
$6S_{1/2}$	(-)0.895	28.514	1.0	0.82
$7S_{1/2}$	1.359	7.263	1.0	0.73
$8S_{1/2}$	0.761	2.508	1.0	0.04
$9S_{1/2}$	0.636	1.223	1.0	0.01
$5D_{3/2}$	3.011	0.935	2.0	2.05
$6D_{3/2}$	0.876	13.465	2.0	0.73
$7D_{3/2}$	0.673	6.999	2.0	0.17
$8D_{3/2}$	0.601	4.051	2.0	0.07
$9D_{3/2}$	0.567	2.466	2.0	0.04
Total				**4.66**

Table 2.6: Contribution to the C_3 coefficient (in kHz μm^3) of $6P_{1/2}$ from dipole virtual couplings considering a perfect reflector. The sign (-) signifies the coupling in emission. This calculation excludes the virtual couplings for which the contribution is less than 0.03 kHz μm^3.

$16S_{1/2}$	Wavelength λ_{ij} in µm	Transition Frequency in THz	Transition Rate, A in s^{-1}	$\frac{2J_>+1}{2J_i+1}$	Value C_3 for ideal reflector in kHz μm^3
$14P_{1/2}$	-40.815	-7.345	3730.176	1.0	10.170
$14P_{3/2}$	-41.890	-7.157	6238.389	1.0	18.389
$15P_{1/2}$	**-133.380**	**-2.248**	**5247.558**	1.0	**499.331**
$15P_{3/2}$	**-142.465**	**-2.104**	**9527.528**	1.0	**1104.743**
$16P_{1/2}$	**179.884**	**1.667**	**3680.162**	1.0	**859.023**
$16P_{3/2}$	**168.606**	**1.778**	**4177.396**	2.0	**1605.884**
$17P_{1/2}$	63.281	4.737	985.310	1.0	10.0129
$17P_{3/2}$	62.122	4.826	1349.249	2.0	25.943
$18P_{1/2}$	41.2	7.262	786.670	2.0	4.438
Total					**4137.9**

Table 2.7: Contribution to the C_3 coefficient (in kHz μm^3) of $16S_{1/2}$ from dipole virtual couplings considering a perfect reflector. The sign (-) signifies the coupling in emission. This calculation excludes the virtual couplings for which the contribution is less than 4 kHz μm^3.

$15D_{3/2}$	Wavelength λ_{ij} in µm	Transition Frequency in THz	Transition Rate, A in s^{-1}	$\frac{2J_>+1}{2J_i+1}$	Value C_3 for ideal reflector in kHz μm^3
$14P_{1/2}$	-31.845	-9.414	3397.807	1.0	4.400
$11F_{5/2}$	-47.035	-6.374	4578.761	1.0	19.105
$15P_{1/2}$	-69.450	-4.317	2199.182	1.0	29.542
$15P_{3/2}$	-71.835	-4.173	569.304	1.0	8.462
$12F_{5/2}$	**-150.203**	**-1.996**	**6173.220**	1.0	**838.888**
$16P_{1/2}$	**-744.997**	**-0.402**	**86.513**	1.0	**1434.528**
$16P_{3/2}$	**-1030.467**	**-0.291**	**6.616**	1.0	**290.324**
$13F_{5/2}$	**212.734**	**1.409**	**3558.962**	1.5	**2061.028**
$17P_{1/2}$	**112.347**	**2.668**	**4881.957**	0.5	**138.80**
$17P_{3/2}$	108.744	2.757	427.250	1.0	22.032
$14F_{5/2}$	72.946	4.110	498.280	1.5	11.633
$18P_{1/2}$	58.531	5.122	3367.401	0.5	13.538
$19P_{1/2}$	42.146	7.113	2501.206	0.5	3.754
Total					**4876.034**

Table 2.8: Contribution to the C_3 coefficient (in kHz μm^3) of $15D_{3/2}$ from dipole virtual couplings considering a perfect reflector. The sign (-) signifies the coupling in emission. This calculation excludes the virtual couplings for which the contribution is less than 4 kHz μm^3.

The prediction of the dipole-dipole interaction coefficient (vdW coefficient), C_3 for $6\mathrm{P}_{1/2} \rightarrow 15\mathrm{D}_{3/2}$ transition, can be estimated as:

$$C_3^{6P_{1/2}\rightarrow 15D3/2} = C_3^{15D_{3/2}} - C_3^{6P_{1/2}} \approx 4.8\ \mathrm{MHz}\,\mu\mathrm{m}^3$$

Table 2.9, shows us the prediction on C_3 for transition between $6P_{1/2} \rightarrow nD_{3/2}, nS_{3/2}$ where n= 15 - 18 considering a perfect reflecting surface:

Transition between **$6\mathrm{P}_{1/2}$**	Wavelength λ_{if} in µm	Value C_3 for ideal reflector in MHz $\cdot\ \mu$m^3
$16\mathrm{S}_{1/2}$	0.513884	**4.1**
$15\mathrm{D}_{3/2}$	0.512068	**4.9**
$17\mathrm{S}_{1/2}$	0.510887	**5.7**
$16\mathrm{D}_{3/2}$	0.509469	**6.6**
$18\mathrm{S}_{1/2}$	0.508537	**7.6**
$17\mathrm{D}_{3/2}$	0.507407	**8.8**

Table 2.9: C_3 coefficients for $nD_{3/2}, nS_{3/2}$ states where n = 15 - 18 considering a perfect reflecting surface.

Comparing the tables 2.6 - 2.8, we see that the dipole-surface interaction coefficient is about 1000 times stronger (in the order of a few MHz μm^3) for the Rydberg states compared to that of the low lying state, $6P_{1/2}$ (in the order of a few kHz μm^3) and would mostly overshadow any effects of low lying states. On the other hand table 2.2 and table 2.9 demonstrate that both of our approaches, electrostatic and QED, give identical results for a perfectly reflecting surface. An inspection of Tables 2.7 and 2.8 also shows that the main dipole couplings contributing to Casimir-Polder interactions of Rydberg atoms are in the far-infrared regime, suggesting that retardation effect can safely be ignored [42].

2.4.2 For a dielectric surface

The interaction between an excited atom and a sapphire surface has already been studied theoretically and experimentally in our group [43][44][45][46] exploring the resonant coupling between atoms and surface polaritons and the temperature dependence of Casimir-Polder interaction. For a real surface (in our case, sapphire), the dielectric constant is a function of frequency. To include the effects of dispersion on Casimir-Polder interactions we adopt the Wylie and Sipe formalism [41][40] (at zero temperature) that has also been extended to include temperature effects [47]. According to [47] the C_3 contribution of a given i-f coupling at zero temperature is given by:

$$C_3(|i>) = \frac{1}{12h}\sum_f r(\omega_{if})|\langle\psi_{n_i}|\mathbf{p}|\psi_{n_f}\rangle|^2 \tag{2.32}$$

with:

$$r(\omega_{if}) = \frac{2}{\pi}\int_0^\infty \frac{\omega_{if}}{\omega_{if}^2+u^2}\frac{\epsilon(iu)-1}{\epsilon(iu)+1}du + 2\Re[S(\omega_{if})]\Theta(-\omega_{if}) \tag{2.33}$$

Here, ω_{if} is the transition frequency that can be negative for downwards (emission) couplings and Θ is the Heaviside function. $\Theta(-\omega_{if})$ takes the value of unity when $\omega_{if} < 0$ (downward coupling) and becomes zero when $\omega_{if} > 0$ (upward coupling). $\epsilon(\omega)$ is the frequency-dependent dielectric constant of the medium, also extended to the complex frequency plane and S is the surface response defined as:

$$S(\omega) = \frac{\epsilon(\omega)-1}{\epsilon(\omega)+1} \tag{2.34}$$

The dielectric constant of sapphire has been measured in many previous works [48][49]. Here we use the works of Barker [48] that provide simple analytical expressions (sum of Lorentzian resonances) for the dielectric constant of sapphire for both ordinary (ϵ_{ord}) and extraordinary (ϵ_{ord}) axes.

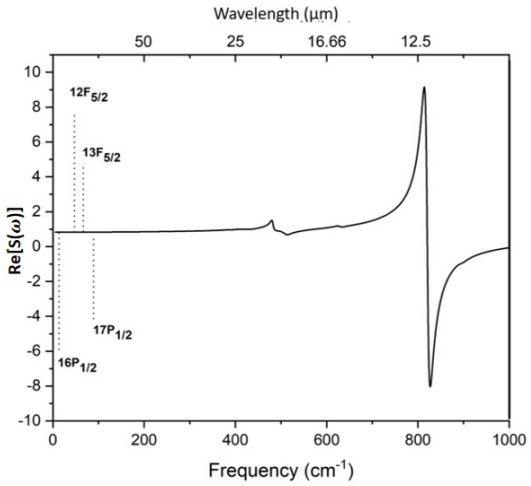

Figure 2.7: Real part of the sapphire surface response Re[S(ω)] as funtion of frequency (in cm$^-$1). Here, we use the geometric mean $(\epsilon_{ord}\ \epsilon_{ext})^{1/2}$ of the dielectric constants, which is the relevant parameter for Casimir-Polder calculations when the extraordinary axis is perpendicular to the sapphire window. The dotted lines show the positions of the virtual couplings from the $15D_{3/2}$ state.

Figure 2.7 shows the real part of the sapphire surface response, Re[S(ω)], as a function of frequency. We see that all influential couplings from the $15D_{3/2}$ state are far away from any surface resonances and the dielectric constant at these frequencies is essentially equal to its static value which we call ϵ_{st}. This suggests that for most Rydberg atoms the effects of the dielectric can simply and straightforwardly be accounted for by multiplying the C_3 coefficient calculated for a perfect reflector by the static surface response $S_{st} = \frac{\epsilon_{st}-1}{\epsilon_{st}+1}$. For the same reasons, CP temperature effects can be safely ignored in the case of Rydberg atoms [Casimir-Polder effect with thermally excited surfaces] . We note that the value of S_{st} varies very little between reported experiments. In Table 2.10 we show the predicted C_3 coefficient of the Rydberg-sapphire interaction for the atomic states relevant to our experiments. For all states, the full QED approach agrees with the electrostatic calculation (performed for perfect conductors) multiplied by S_{st}.

Transition between **6P$_{1/2}$**	Value C_3 for Sapphire in MHz μm^3	Value C_3 for perfect reflector in MHz μm^3
16S$_{1/2}$	**3.5**	**4.1**
15D$_{3/2}$	**4.1**	**4.9**
17S$_{1/2}$	**4.8**	**5.7**
16D$_{3/2}$	**5.6**	**6.6**
18S$_{1/2}$	**6.4**	**7.6**
17D$_{3/2}$	**7.4**	**8.8**

Table 2.10: C_3 coefficient for $nD_{3/2}, nS_{3/2}$ states where n = 15 - 18.

Chapter 3

Spectroscopy of Casimir-Polder Interaction: Selective Reflection (SR) Spectroscopy and Thin Cell (TC) Spectroscopy

---

To probe the Casimir-Polder interaction of a Rydberg atom with a dielectric surface, we have used two techniques: selective reflection (SR) spectroscopy and thin cell (TC) spectroscopy. SR spectroscopy consists of measuring the change of the reflection coefficient at the interface between a dielectric surface and the resonant atomic vapour [45][38] as the laser frequency is scanned around the atomic resonance. With a nanometric thin vapour cell (TC), the spatial dependence of the Casimir-Polder interaction can also be explored by confining atoms close to a surface with reflection or transmission spectroscopy (reflection and transmission spectroscopy are complementary). In this following chapter, we briefly discuss both of these techniques in the context of strong Rydberg surface interaction.

In section 3.1, we introduce the theoretical framework for Selective Reflection (SR) spectroscopy followed by a brief discussion on the general solution of SR lineshape (section 3.1.1). In section 3.1.2 we present the SR lineshapes in the absence of atom-surface interaction and subsequently in section 3.1.3 we briefly discuss the frequency-modulated

Selective Reflection spectroscopy (FMSR). In section 3.1.4 we present the solution FMSR lineshape in the presence of atom-surface interactions under infinite Doppler ($\gamma \ll$ ku, Doppler width) and motionless atom ($v_z = 0$) approximation [18]. This approximation has extensively been used to measure atom surface interactions [38] [22] [50] for low-lying atomic states. However, this approximation breaks down on interpreting highly excited Rydberg surface interactions, such as the ones performed during this thesis.

Therefore, section 3.2 presents a novel numerical development for simulating SR lineshapes (section 3.2.1) accounting for the Maxwell-Boltzmann atomic velocity distribution. We further discuss the evolution of SR lineshape for different velocity distributions (section 3.2.2) in the presence of weak and strong atom surface interactions (section 3.2.3). We will subsequently use this model (using the full atomic velocity distribution) to fit our experimental spectra and measure the C_3 coefficient of Rydberg-surface interactions in Chapter 5.

In section 3.3, we briefly discuss thin cell (TC) spectroscopy. Nanometric thin cells (TC) with varying thicknesses were already used by our group for probing atoms at a nanometric distance from the surface [23]. Here we present the necessary theoretical overview (section 3.3.1) for simulating TC lineshapes [51][52] and our numerical adoption for simulating TC lineshapes under the influence of strong atom surface interactions. Finally, in section 3.3.2, we present thin cell (TC) lineshapes taking into account higher-order interaction (quadrupole interaction) and examine the conditions under which higher-order interactions can be experimentally observable.

3.1 Selective reflection (SR) spectroscopy

For the theoretical framework, we follow the notations and the formalism already described in [18]. We take an interface (infinitely extended in $x - y$ plane) between atomic vapour filling $z>0$ and a dielectric surface ($z<0$) having refractive index $\mathbf{n}$ (Figure 3.1) where z is the atom-surface separation (an atom-surface separation for which the atomic

structure of the surface is insignificant). A plane wave $\mathcal{E}_i$ having wavevector $\mathbf{k}$ incident on the interface (from the dielectric side) is partly reflected $\mathcal{E}_r$ into the dielectric surface and partly refracted $\mathcal{E}_t$ in the atomic vapour (as the incident angle is near normal to the interface plane and the field propagation is only along z, the fields are represented in scalar form).

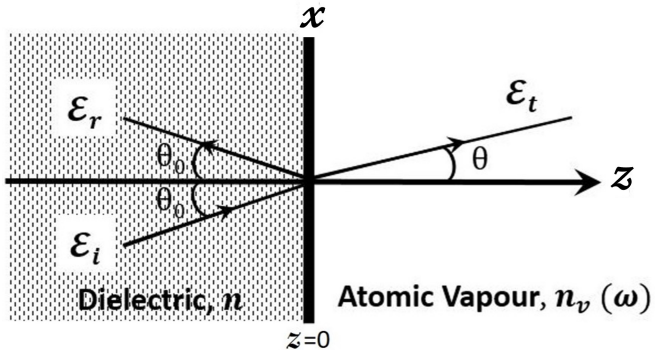

Figure 3.1: Geometry of incident $\mathcal{E}_i$, refracted $\mathcal{E}_t$ and reflected $\mathcal{E}_r$ waves. The $x-y$ plane is the interface between the atomic vapour and the surface. n is the refractive index of the surface and $n_v(\omega)$ is the effective refractive index of the atomic vapour. θ_0 is the incident angle ($\theta_0 \ll 1$). z is atom surface separation.

For a normal incident beam, the field transmitted into the vapour can be expressed as:

$$E_t(r,t) = \mathcal{E}_t e^{(\mathbf{k}z-\omega t)} + c.c\,(\text{complex conjugate}) \tag{3.1}$$

where $\mathcal{E}_t$ is the amplitude and ω is the frequency of the transmitted field. The incident electric field tuned close to the atomic resonance ω_0 polarizes the atomic medium which re-emits a field that propagates in the direction of the reflected field $\mathcal{E}_r$. Thus the field reflected at the interface is the sum of the non-resonant contribution reflected from the interface and a resonant contribution emitted in the backward direction from the atomic vapour. We assume that the resonant contribution is much smaller than the non-resonant contribution, i.e. the vapour effective refractive index deviates negligibly from unity.

The induced macroscopic vapour polarization P may be spatially in-homogeneous due to the motion-induced spatial dispersion and surface-induced atomic resonance shifts. We consider that the surface is smooth enough so that the atomic structure of the surface is insignificant. We also suppose that atoms get de-excited upon colliding with the surface losing their phase coherence with the excitation field. Considering translational invariance

along the $x-y$ plane (plane parallel to the surface), the slowly varying amplitude of P may depend only on z. The induced macroscopic electric polarization can be written as:

$$P(z,t) = p(z)e^{i(kz-\omega t)} + c.c. \tag{3.2}$$

where z is the atom-surface separation, $p(z)$ is the amplitude of the induced atomic dipole at position z.

This macroscopic polarization can be related to the change in the reflected field by introducing an effective atomic vapour susceptibility $\bar{\chi}$ with an oscillating phase factor "exp($2ikz$)". This "phase factor" yields the round-trip accumulated phase appearing in the reflected field radiated by the atom at the position z. The effective atomic vapour susceptibility can be expressed as [53][54][55]:

$$\bar{\chi} = -\frac{2i\mathrm{k}}{\epsilon_0 \mathcal{E}_t} \int_0^{+\infty} dz \cdot p(z)e^{2ikz} \tag{3.3}$$

where ϵ_0 is the vacuum permittivity, k is the wavevector in vacuum.

Considering the modification of the resonant reflectivity to be much smaller than unity, the effective refractive index of the vapour n_v can be introduced in the Fresnel reflection formula as:

$$n_v = \sqrt{1+\bar{\chi}} = 1 + \bar{\chi}/2 \tag{3.4}$$

(when $\bar{\chi} << 1$)

The e.m. field reflected into the dielectric can be written as $\mathcal{E}_r = r(\omega-\omega_0)\mathcal{E}_i$, where $\mathcal{E}_i$ is the incident field and $r(\omega-\omega_0)$ is the reflection coefficient. For normal incident irradiation, using the Fresnel reflection formula, the reflection coefficient becomes:

$$\begin{aligned} r(\omega-\omega_0) &= \frac{n-(1+\bar{\chi}/2)}{n+(1+\bar{\chi}/2)} \\ &\approx \frac{n-1}{n+1} - \frac{n}{(n+1)^2}\bar{\chi}(\omega-\omega_0) \\ &\approx r_0 + \rho\bar{\chi}(\omega-\omega_0) \end{aligned} \tag{3.5}$$

(as $\bar{\chi} << 1$)

Where r_0 is the dielectric-vacuum reflection coefficient (non-resonance reflection coefficient) and $\rho\bar{\chi}$ is vapour-induced reflectivity change.

The change of reflectivity at the interface between the atomic vapour and dielectric can be given as:

$$\begin{aligned} R(\omega-\omega_0) &= |r(\omega-\omega_0)|^2 \\ &= |r_0+\rho\bar{\chi}(\omega-\omega_0)|^2 \\ &\approx r_0^2 + 2r_0\rho\cdot\Re\left[\bar{\chi}(\omega-\omega_0)\right] \end{aligned} \tag{3.6}$$

The selective reflection (SR) signal can thus be expressed as:

$$I_{SR}(\omega-\omega_0) = 2r_0\rho\cdot\Re\left[\bar{\chi}(\omega-\omega_0)\right] \tag{3.7}$$

3.1.1 A general solution to selective reflection (SR) spectroscopy

To evaluate the effective atomic vapour susceptibility (equation 3.3), first the induced atomic vapour polarization $P(z)$ (equation 3.2) needs to be calculated. The driving field ($\mathcal{E}_t$) frequency (equation 3.1) tuned close to the atomic resonance (ω_0), the atomic vapour can be considered as a collection of two-level atomic systems (ground state $|g\rangle$; excited state $|e\rangle$) whose density matrix is governed by the Bloch equations. The macroscopic dipole polarization can be determined by:

$$p(z) = N\mu\int_{-\infty}^{+\infty} dv_z W(v_z)\sigma_{eg}(z,v_z) \tag{3.8}$$

where μ is the e-g electric dipole moment, N is the atomic density, $W(v_z)$ is the normalized velocity distribution along the z-direction. σ_{eg} is the off-diagonal density matrix element which measures the amount of the optical coherence between the states $|e\rangle$ and $|g\rangle$.

The incident field is supposed to be weak enough so that the atomic response is linear and the time evolution of σ_{eg} can be obtained from the Bloch equations using the rotating

wave approximation [56]:

$$\frac{d}{dt}\sigma_{eg} = -\left[\frac{\gamma}{2} - i(\omega - \omega_0 - kv_z)\right]\sigma_{eg} + i\frac{\Omega}{2} \tag{3.9}$$

where

- ω_0 is the atomic resonance frequency and ω is the frequency of the driving field.
- $\Omega = 2\mu\mathcal{E}_t/\hbar$ is the Rabi frequency. We consider that in the SR technique, the attenuation of the field over the probing region is so weak that the driving (transmitted) field $\mathcal{E}_t$ remains constant.
- γ is the optical transition linewidth, taking into account the natural transition linewidth as well as collisional broadening.
- kv_z is the Doppler shift for a normal incident.

Using the hydrodynamic conservation, the time evolution of optical coherence transforms into:

$$\frac{d\sigma_{eg}}{dt} = \frac{\partial\sigma_{eg}}{\partial t} + v_z\frac{\partial\sigma_{eg}}{\partial z}$$

Apart from the straightforward assumptions like negligible change in the refractive index ($|\chi| << 1$) and linearity with driving field (Rabi Frequency, $\Omega << \gamma$), we also assume that the atomic trajectories are rectilinear and atoms travel at a constant speed neglecting changes in the curvature of trajectories due to surface-induced forces or due to velocity changing inter-atomic collisions.

For the steady-state regime σ_{eg} is only a function of z and can be expressed as:

$$v_z\frac{d\sigma_{eg}(z)}{dz} = -\left[\frac{\gamma}{2} - i(\omega - \omega_0 - k\cdot v_z)\right]\sigma_{eg} + \frac{i\Omega}{2} \tag{3.10}$$

A general solution of equation 3.10 can be obtained by integration for a given position z knowing the solution at z_0, where z_0 is the atom-surface separation for which the optical coherence vanishes (i.e. $\sigma_{eg} = 0$ at $z_0 = 0$ or $+\infty$) and is given by:

$$\sigma_{eg}(v_z, z) = \frac{i\Omega}{2v_z}\int_{z_0}^{z} dz' e^{[\mathcal{L}(z') - \mathcal{L}(z)]/v_z} \tag{3.11}$$

with $\mathcal{L}(z)$ being the 'lineshape function' given by:

$$\mathcal{L}(z) = \mathcal{L}_0(z) + izkv_z \tag{3.12}$$

where

$$\mathcal{L}_0(z) = \int_{z_0}^{z} dz \left[\frac{\gamma}{2} - i(\omega - \omega_0)\right] \tag{3.13}$$

Subsequently, a general solution of equation 3.11 can be obtained considering the following three cases:

- For $v_z > 0$ i.e. the atoms going away from the surface. Due to the collision with the wall, the light-atom interaction is disrupted. In this case $\sigma_{eg} = 0$ at $z_0 = 0$.

$$\sigma_{eg}(v_z > 0, z) = \frac{i\Omega}{2v_z} \int_0^z dz' e^{[\mathcal{L}(z') - \mathcal{L}(z)]/v_z} \tag{3.14}$$

- For $v_z < 0$ i.e. the atoms coming towards the surface from far $z = +\infty$ side. We consider that atoms are not exited as the excitation fields get fully absorbed while travelling along z. In this case $\sigma_{eg} = 0$ for $z_0 = +\infty$.

$$\sigma_{eg}(v_z < 0, z) = \frac{i\Omega}{2v_z} \int_{+\infty}^z dz' e^{[\mathcal{L}(z') - \mathcal{L}(z)]/v_z} \tag{3.15}$$

- For $v_z = 0$ i.e. atoms are moving parallel to the interaction plane XY. For this special case, we can obtain a semi-analytical solution from equation 3.10, given by:

$$\sigma_{eg}(v_z = 0, z) = i\frac{\Omega}{2} \frac{1}{(\gamma/2) - i\left[\omega - \omega_0 - kv_z\right]} \tag{3.16}$$

Substituting equation 3.11-3.16 in equation 3.8, the atomic vapour polarization can be expressed as:

- For $v_z > 0$:

$$p(v_z > 0, z) = \frac{i\Omega}{2} N\mu \int_{-\infty}^{+\infty} dv_z \frac{W(v_z)}{v_z} \int_0^z dz' e^{[\mathcal{L}(z') - \mathcal{L}(z)]/v_z} \tag{3.17}$$

- For $v_z < 0$:

$$p(v_z < 0, z) = \frac{i\Omega}{2} N\mu \int_{-\infty}^{+\infty} dv_z \frac{W(v_z)}{v_z} \int_{+\infty}^z dz' e^{[\mathcal{L}(z') - \mathcal{L}(z)]/v_z} \tag{3.18}$$

Substituting the equations 3.17-3.18 in equation 3.3 allows us to obtain a general expres-

sion of the effective atomic vapour susceptibility as:

$$\bar{\chi}(v_z > 0) = \frac{2N\mu^2 \mathrm{k}}{\epsilon_0 \hbar} \int_0^{+\infty} \frac{dv_z}{v_z} [W(v_z)] \int_0^{+\infty} dz \int_0^z dz' e^{2ikz} e^{[\mathcal{L}(z')-\mathcal{L}(z)]/v_z} \tag{3.19}$$

and

$$\bar{\chi}(v_z < 0) = \frac{2N\mu^2 \mathrm{k}}{\epsilon_0 \hbar} \int_{-\infty}^0 \frac{dv_z}{v_z} [W(v_z)] \int_0^{+\infty} dz \int_{+\infty}^z dz' e^{2ikz} e^{[\mathcal{L}(z')-\mathcal{L}(z)]/v_z} \tag{3.20}$$

The corresponding selective reflection signal I_{SR} can expressed as:

$$\begin{aligned} I_{SR} &= I_{SR,v_z>0} + I_{SR,v_z<0} \\ &= r_0 \rho \cdot \Re \left[\bar{\chi}(v_z > 0) + \bar{\chi}(v_z < 0) \right] \end{aligned} \tag{3.21}$$

It is noteworthy to mention that $\bar{\chi}(v_z)$ is an even function of v_z, i.e. $\bar{\chi}(v_z > 0) = \bar{\chi}(v_z < 0)$. For a linear reflection signal, $(+v_z)$ and $(-v_z)$ atomic velocity group has identical contributions [57][56]. This remarkable behaviour is valid irrespective of whether we consider the atom surface interaction or not. Therefore, the integration over velocity for the atoms which arrive towards the surface and the atoms which leave it, are identical and eventually double. Now, the integration limits of z and z' can be interchanged as:

$$\int_0^{+\infty} dz \int_z^{+\infty} dz' = \int_0^{+\infty} dz' \int_0^z dz$$

and a general solution of the SR signal for all velocity classes can be given by:

$$I_{SR} = \eta r_0 \rho \Re \left[\int_0^{+\infty} \frac{dv_z}{v_z} [W(v_z)] \int_0^{+\infty} dz \int_0^z dz' e^{2ikz} e^{[\mathcal{L}(z')-\mathcal{L}(z)]/v_z} \right] \tag{3.22}$$

where $\eta = \frac{8N\mu^2 \mathrm{k}}{\epsilon_0 \hbar}$.

3.1.2 Selective reflection signal in the absence of atom surface interaction

For a freely-processing atomic polarization not affected by the atom surface interaction, γ and ω_0 are independent of z. The lineshape function of equation 3.12 simply becomes :

$$L = \left[\gamma/2 - i(\omega - \omega_0 - k \cdot v_z) \right] z \tag{3.23}$$

Using equation 3.23 in 3.22 and performing integration along z and z' we can express the SR signal as [38]:

$$I_{SR} = \frac{\eta r_0 \rho}{k} \Re \left[\int_0^{+\infty} W(v_z) \frac{\omega - \omega_0 + k v_z}{(\gamma/2)^2 + (\omega - \omega_0 + k v_z)^2} dv_z \right] \tag{3.24}$$

($\Re$ is the real part of the complex function)

where, $W(v_z) = (v_p\sqrt{\pi})^{-1} e^{-(v_z^2/v_p^2)}$ is the Maxwell-Boltzmann velocity distribution with v_p being the most probable velocity.

Equation 3.24 can be simplified using the reduced variable as $\Delta = \omega - \omega_0/kv_p$, $\Lambda = (kv_z)/(kv_p)$ and $\Gamma = \gamma/(2kv_p)$.

$$I_{SR}(\Delta) = \frac{\eta r_0 \rho}{k} \Re \left[\int_0^{+\infty} W(\Lambda) \frac{\Delta + \Lambda}{(\Delta + \Lambda)^2 + \Gamma^2} d\Lambda \right] \tag{3.25}$$

Equation 3.25 is a product of Maxwell velocity distribution ($W(\Lambda)$) and a dispersive Lorentzian ($[\Delta+\Lambda]/[(\Delta+\Lambda)^2+\Gamma^2]$) of width Γ whose amplitude will be greater from the smaller value of Γ and presents a divergence as $\Gamma \to 0$. Figure 3.2 shows the SR signal lineshape in the absence of atom surface interaction for different values of Γ.

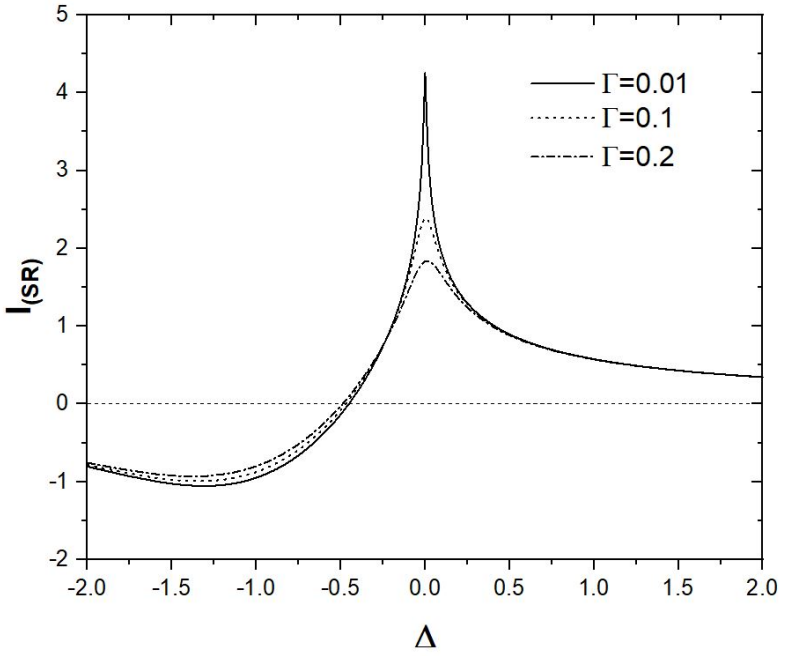

Figure 3.2: Selective reflection lineshape in the absence of atom-surface interaction for different values of homogeneous linewidth. $\Delta = \omega - \omega_0/kv_p$ where v_p is the most probable velocity.

The SR lineshape free from atom surface interaction resembles a Doppler broadened dispersion lineshape and amplitude of dispersive Lorentzian ($[\Delta + \Lambda]/[(\Delta + \Lambda)^2 + \Gamma^2]$) increases as Γ decreases and it posses a logarithmic singularity as $\Gamma \to 0$. The selective reflection lineshape has the contribution of all velocity groups with a weight factor of $1/\Lambda$ but with a greater contribution for $v_z = 0$. i.e. the contribution of the atoms that move parallel to the interaction plane. For these atoms, the interaction is less affected by the collision, and the major changes in the lineshape are observed as $\Delta \to 0$. For the most practical cases, we are mostly interested in this region ($\Delta \to 0$) rather than the Doppler broaden profile. One of the most common ways to eliminate this broad Doppler profile is to perform a frequency-modulated selective reflection spectroscopy.

3.1.3 Frequency modulated selective reflection signal (FMSR)

To monitor the weak resonant change in the reflection coefficient relative to a strong non-resonant reflected background, most of the time SR spectroscopy is carried out with small frequency modulation (FM) on the incident field and a phase-sensitive heterodyne detection is performed to retrieve the FMSR signal. This also provides a convenient means to observe the narrow lineshape of the SR signal while effectively suppressing the Doppler response.

A general expression of the incident field taking into account FM can be written as:

$$\mathcal{E}_i = |\mathcal{E}_i| e^{-i(M sin\, \omega_m t)} = |\mathcal{E}_i| \sum_N J_N(M) e^{-iN\omega_m t}$$

where M and ω_m are the modulation index and frequency respectively. J_N is the Bessel function of order N. A corresponding reflected field can be also expressed as:

$$\mathcal{E}_r = \sum_N r(\omega + N\omega_m) |\mathcal{E}_i| J_N(M) e^{-iN\omega_m t}$$

where $r(\omega + N\omega_m)$ is the reflection coefficient at $(\omega + N\omega_m)$ given by : $r(\omega + N\omega_m) = r_0 + \rho\bar{\chi}(\omega + N\omega_m)$. r_0 is the non-resonant reflection coefficient.

The resonant change of the reflectivity at the interface $R = |\mathcal{E}_r/\mathcal{E}_i|^2$ can given by [18]:

$$\delta R(\omega_m) = r_0\rho \sum_N [\bar{\chi}(\omega + N\omega_m) + \bar{\chi}^*(\omega + N\omega_m - \omega_m)]J_N J_{N-1} e^{-i\omega_m t} + c.c \tag{3.26}$$

For a small value of modulation frequency and index, the FMSR signal (after demodulation at ω_m) can be approximated as:

$$I_{FMSR} = M \cdot r_0\rho\Re\left[\frac{d\bar{\chi}(\omega)}{d\omega}\right] \tag{3.27}$$

Figure 3.3 shows the FMSR (solid line) signal along with the SR signal (dashed line). The slowly varying broad Doppler "wings" of SR spectra get flattened for the FMSR spectra whereas the fast variation close to logarithmic singularity around v_z=0 becomes prominent which helps to obtain a better contrast over the region of interest.

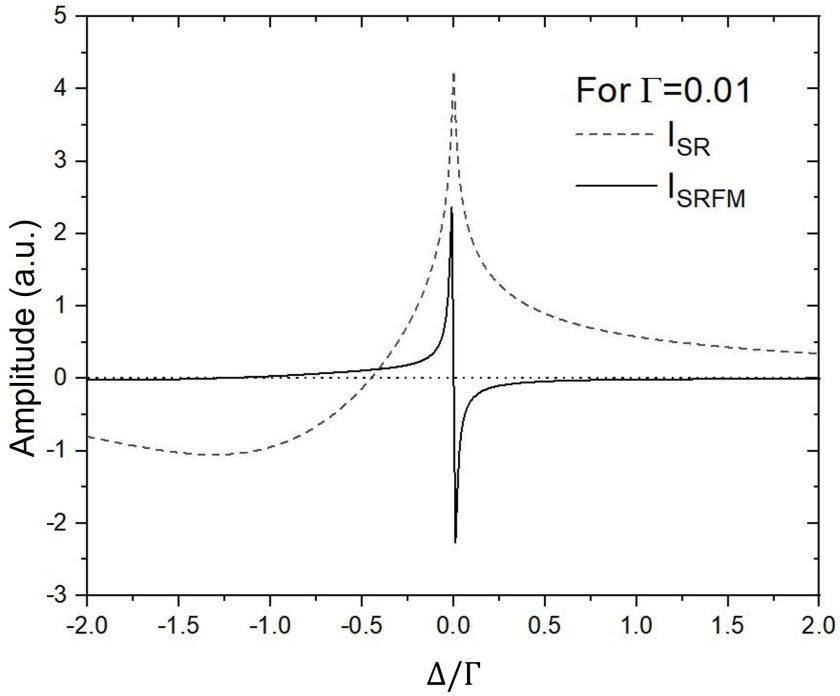

Figure 3.3: Selective reflection lineshape in the absence of atom surface interaction: SR signal (Dash line), FMSR signal (solid line) in normalized frequency scale i.e Δ/Γ.

Up to this point, we have excluded the atom-surface interaction. In the following sections, we present the formalism of the selective reflection spectroscopy in the presence of atom surface interaction.

3.1.4 Selective reflection signal in the presence of atom surface interaction

In the presence of atom-surface interactions, the lineshape function (equation 3.12) is modified (here limiting to dipole-image dipole interaction term) and can be expressed as:

$$\mathcal{L}(z) = (\gamma/2)z - i(\delta - kv_z)z + \left[i(C_3/2z^2)\right] \tag{3.28}$$

where $\delta = \omega - \omega_0$ and C_3 is the van der Waals coefficient.

Subsequently, the SR signal in the presence of dipole-image dipole interaction can be obtained by substituting this modified lineshape function (equation 3.28) in equation 3.22, given by:

$$I_{SR} = \eta r_0 \rho \Re \left[\int_0^{+\infty} \frac{dv_z}{v_z} [W(+v_z) + W(-v_z)] \int_0^{+\infty} dz \int_0^{+\infty} dz' e^{2ikz} e^{[\mathcal{L}(z') - \mathcal{L}(z)]/v_z} \right] \tag{3.29}$$

The numerical approach to solve the general expression of SR lineshape in the presence of atom surface interaction (equation 3.30) is computationally intensive and complicated mainly because:

- it involves the computation of a triple integral.
- the oscillatory behaviour of the $\exp\left(\mathcal{L}(z') - \mathcal{L}(z)\right)$ function.
- the $(1/v_z)$ term diverges when $v_z \to 0$.

Before going into the details of the numerical procedure for solving the general solution of SR lineshape, we briefly present some of the pre-existing solutions for SR lineshapes in some limiting cases. For some well-chosen approximations, the calculation can be simplified and has been successfully used previously [58][46][45] on predicting weak atom surface interaction.

3.1.4.1 Selective reflection signal with infinite Doppler approximation

In the infinite Doppler approximation i.e. when the homogeneous transition linewidth (γ) and the atom-surface shifts are much smaller than the Doppler width (kv), we can assume that the major contribution to the FMSR signal comes from slow atoms (in the direction of the beam). In this case ($ku >> \gamma$) we can simply assume that $W(\pm v_z) = W(0)$ and the FMSR signal (equation 3.27) becomes [18]:

$$I_{FMSR} = M \cdot \eta r_0 \rho[W(0)] \cdot \Re\left[\frac{d}{d\omega}\left(\int_0^{+\infty} dz \int_0^{+\infty} dz' e^{2ik(z+z')} \frac{z - z'}{\mathcal{L}(z') - \mathcal{L}(z)}\right)\right] \tag{3.30}$$

On the other hand, in the case of strong Rydberg-surface interactions, the atom-surface shifts can be huge and can exceed the Doppler width, especially for small atom-surface separations. For example, when C_3 =5 MHz μm^3 and atom surface separation is z=200 nm (typical probing depth), the atom-surface shift is about 600 MHz, which is larger than the typical Doppler width of FWHM 500 MHz. In this case, the infinite Doppler approximation is no longer valid.

3.1.4.2 Selective Reflection signal with motionless atom approximation

When the homogeneous transition linewidth γ and the atom-surface interaction shifts become much larger than the Doppler shift, the effects of atomic motion can be ignored. In this case of motionless atoms, the SR signal can have a semi-analytical solution as:

$$I_{SR} = \frac{2N\mathrm{k}\mu^2}{\hbar\epsilon_0} \int_0^{+\infty} dz \frac{e^{2ikz}}{\frac{1}{2}\gamma - i(\omega - \omega_0 - \frac{C_3}{z^3})} \tag{3.31}$$

For our Rydberg atom interactions, neither of these two approximations is fully valid as the homogeneous transition linewidth ($\sim$ 100MHz), as well as the atom-surface interaction shifts ($\sim$ 600MHz), are comparable to the Doppler width ($\sim$ 500MHz). So it was necessary to obtain a numerical solution of the general SR lineshape (equation 3.30). During this thesis, we overcame the numerical limitations and developed a novel numerical model that takes into account the atom surface interaction as well as the effect of atomic velocity

distribution (Maxwell-Boltzmann velocity distribution).

3.2 A numerical approach on solving selective reflection spectroscopy

Our experiment is a collaborative project between the SAI (Spectroscopie Atomique aux Interfaces) group, Université Sorbonne Paris Nord, France and QMS (Quantenoptik makroskopischer Systeme) group, Universität Rostock, Germany under ANR funding (SQUAT project). During this thesis, Chris Boldt a PhD student of the QMS group visited our SAI group and we developed a numerical method for simulating the selective reflection lineshape (equation 3.30). The numerical simulation was carried out in MATLAB software utilizing a parallel computing toolbox and the integration time was optimized by using the cumulative summing method [59].

3.2.1 Numerical approach to solve the z and z' integral

Separating z and z' variable, the general solution of the FMSR signal (equation 3.30) can be rewritten in the following form:

$$\begin{aligned} I_{FMSR} &= M \cdot \eta r_0 \rho \Re \left[\int_0^{+\infty} dv_z \frac{W(v_z)}{v_z} \int_0^{+\infty} dz \cdot e^{2ikz} e^{-[\mathcal{L}(z,v_z)]} \int_0^{z} dz' \cdot e^{[\mathcal{L}(z',v_z)]} \right] \\ &= \eta r_0 \rho \cdot \Re \left[\int_0^{+\infty} dv_z \frac{W(v_z)}{v_z} \cdot \mathcal{I} \right] \end{aligned} \tag{3.32}$$

where

- $\mathcal{I}$ consists the z and z' integral:

$$\mathcal{I} = \int_0^{+\infty} dz \cdot e^{2ikz} e^{-[\mathcal{L}(z,v_z)]} \int_0^{z} dz' \cdot e^{[\mathcal{L}(z',v_z)]} = \int_0^{+\infty} dz \cdot \mathcal{H}(z) \tag{3.33}$$

- $\mathcal{H}(z)$ is a function that includes all the integrand of z integral, given by:

$$\mathcal{H}(z) = e^{2ikz} e^{-[\mathcal{L}(z,v_z)]} \int_0^{z} dz' \cdot e^{[\mathcal{L}(z',v_z)]}$$

- $\mathcal{L}(z, v_z)$ is the predefined lineshape function including the $1/v_z$ factor.

$$\begin{aligned}\mathcal{L}(z, v_z) &= -\frac{\gamma}{2v_z}z + i\frac{\delta - kv_z}{v_z}z - \left[i\frac{C_3}{2v_z}\frac{1}{z^2}\right] \\ &= -\mathcal{A}z + i\mathcal{B}z - i(\mathcal{C}/z^2)\end{aligned} \tag{3.34}$$

  where $\mathcal{A} = (\gamma/2v_z)$, $\mathcal{B} = (\delta - kv_z)/v_z$ and $\mathcal{C} = C_3/2v_z$.

To solve the integral $\mathcal{I}$, we need to study the evolution of $\mathcal{H}(z)$ as a function of γ, v_z, and C_3.

Figure 3.4 shows the real part of $\mathcal{H}(z)$ in terms of atom surface separation z for $C_3 = 1$ MHz μm^3, $\gamma = 25$ MHz, δ= -50 MHz and $v_z = 100$ m/s. For relevant Rydberg-surface interaction, C_3 typically lies in the order of few MHz μm^3 and detuning δ and velocity v_z are chosen thoughtfully so that variation of $\mathcal{H}(z)$ are easily visible as the different variables are changed.

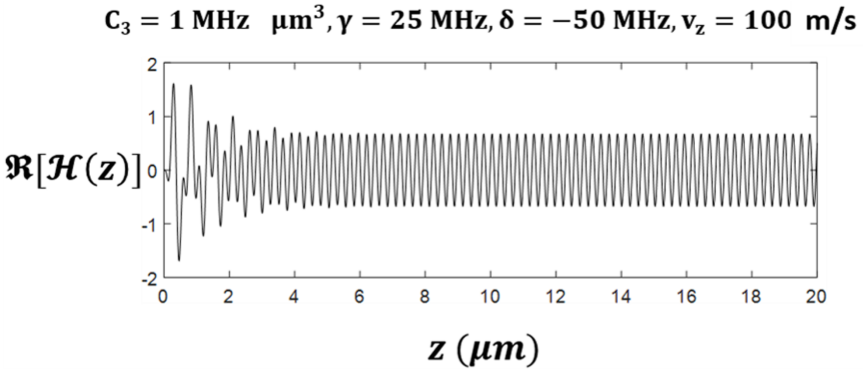

Figure 3.4: Real part of $\mathcal{H}(z)$ as a function of z (in micron) for $C_3 = 1$ MHz μm^3, $\gamma = 25$ MHz, δ = - 50 MHz and $v_z = 100$ m/s.

The response of $\mathcal{H}(z)$ can be crudely divided into two parts:

- Approaching towards the wall, i.e. $z \to 0$ (referring as the "transient regime"): the response consists of non-periodic oscillation, as the "$\exp(i\mathcal{C}/z^2)$" term, oscillates rapidly and overshadows other terms of $\mathcal{H}(z)$ as $z \to 0$.
- Approaching towards infinity, i.e. $z \to +\infty$ (referring as "steady-state regime"): the response consists of periodical oscillation, as "$\exp(i\mathcal{C}/z^2)$" term dies off quickly as $z \to +\infty$.

Observing the response of $\mathcal{H}(z)$ (figure 3.4), one can say that the major contribution to the integral $\mathcal{I}$ comes from the small value of z (transient regime). Furthermore, the

integral will only converge if we assume "losses" that suppress the periodical oscillations evident for large values of z (steady-state regime). In the following, we present two possible losses to the $\mathcal{H}(z)$ to ensure convergence of integral $\mathcal{I}$.

3.2.1.1 Truncation of $\mathcal{H}(z)$ with a damping function

First, we use the "Logistic function" [60][61] (i.e. sigmoid curve) as a dampening function, given by:

$$f(z) = \frac{f_c}{1 + e^{k[z-z_0]}}$$

where

z_0, the value of the sigmoid's midpoint.

f_c, the supremum of the values of the function.

k, the logistic decay rate or steepness of the curve.

For instance to truncate $\mathcal{H}(z)$ at a distance 'L' (cut-off point) where L corresponds to a large value of z (lies in the so-called steady-state regime). It is also preferred that the amplitude of $\mathcal{H}(z)$ "smoothly" go down to a small value like 1% of the initial value at L (i.e. $f_c = 10^{-2}$). 'z_0' is the point where the logistic function goes to half of its initial value and to make it smoother, the midpoint can be shifted to $3/4$ of the cut-off point i.e. $z_0 = 3L/4$. Satisfying these conditions, the k value can be calculated as:

$$k = \frac{4}{L} ln \frac{1 - f_c}{f_c} \tag{3.35}$$

Thus the logistic function $f(z)$ becomes:

$$f(z) = \frac{1}{1 + e^{k[z-(3L/4)]}} \tag{3.36}$$

Figure 3.5 shows the Logistic function as a function of z for different L values. For a larger value of the L, the steepness of the function decreases (becomes smoother) which is desirable as this slow decay would encounter more oscillations before reaching 1%.

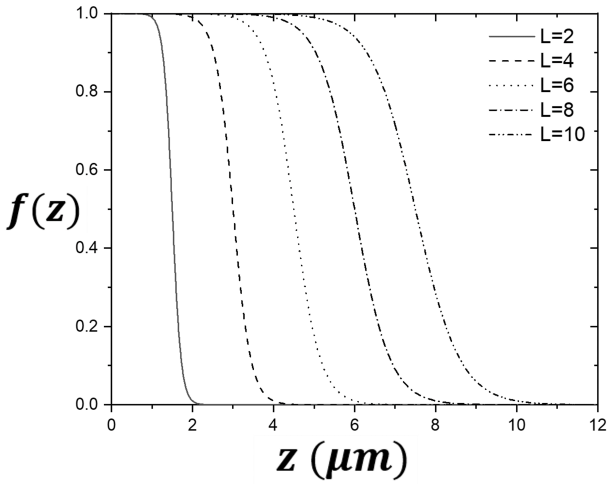

Figure 3.5: Logistic function $f(z)$ as a function of z (in μm) for different L values (in μm).

Applying the logistic function $f(z)$ for L=15 μm to $\mathcal{H}(z)$ (Figure 3.4), we get:

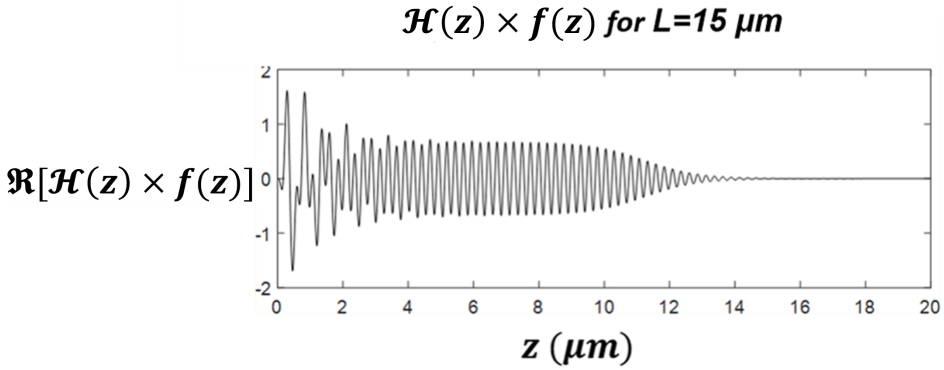

Figure 3.6: Real part of $\mathcal{H}(z) \times f(z)$ (for L = 15 μm) as a function of z (in μm).

It is evident that the logistic function with a cutoff point $L = 15\mu$m is more than sufficient for ensuring the convergence of the integral $\mathcal{I}$ without truncating the essential portions of the integral. The selection of this cutoff point is subjective to the variable of $\mathcal{H}(z)$ (i.e. C_3, Γ and v_z). It is worth noting that an excessively large value of L can lead to prolonged numerical simulation time, while an overly small value of L may truncate essential portions of the integral leading to inaccurate integral values.

One approach to determining an appropriate value of L involves systematically testing a range of L values, spanning from very small to large values with small increments ($\leq 0.005nm$) and evaluate the impact on the amplitude of the integral $\mathcal{I}$. This process was carried out for different combinations of C_3, Γ, and v_z. Figure 3.7 depicts the amplitude

variation of the real part of $\mathcal{I}$ for different values of (a) γ, (b) v_z and (c) C_3 (while keeping other variables constant) as the value of L is systematically adjusted. This testing aids to identify the optimal value of L at which the amplitude of integral $\mathcal{I}$ converges to a stable value.

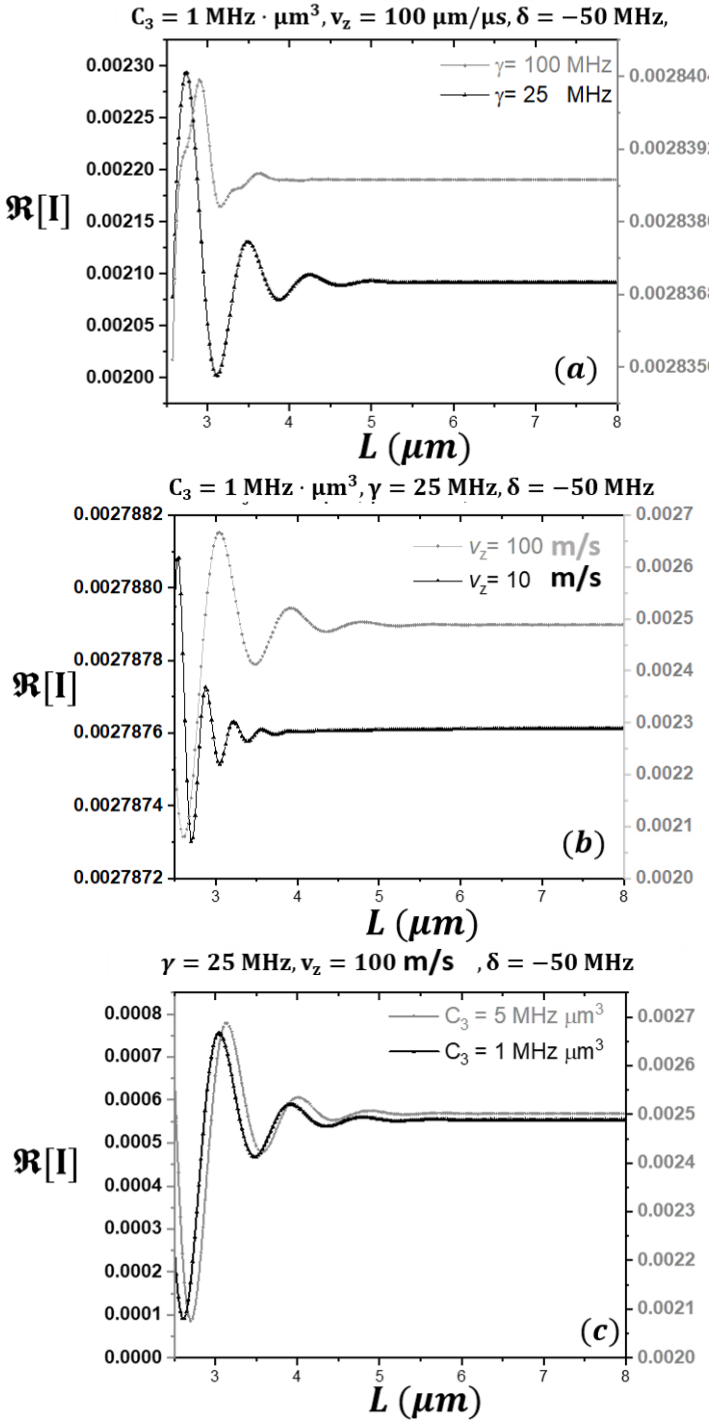

Figure 3.7: The amplitude variation of the real part of integral $\mathcal{I}$ for different cut-off points L for different combination of (a) γ, (b) v_z and (c) C_3 while keeping other two variables as constant.

For small values of L (cut-off points resemble a small atom surface separation z), the values of $\mathcal{I}$ exhibit considerable variation. This is expected as the logistic function truncates essential portions of $\mathcal{I}$ before it can reach a steady state. However, as the cutoff point is carefully adjusted to an optimal length, the amplitude of $\mathcal{I}$ stabilizes, ultimately yielding a consistent value. During this calculation, the convergence of $\mathcal{I}$ is accepted when the amplitude variation is well below 0.00001%.

In figure 3.7 (a), we see that the integral $\mathcal{I}$ converges faster for a larger value of γ (convergence is achieved at $L \sim 4.5$ μm when $\gamma = 100$ MHz and at $L \sim 6$ μm for $\gamma = 25$ MHz). As the decay lifetime of the atomic dipole is longer for smaller linewidth, the atom can explore more depth along z. Hence $\mathcal{I}$ converges at larger values of L for smaller values of γ.

In Figure 3.7 (b), we explore the convergence of $\mathcal{I}$ for two different velocities, v_z (100 m/s and 10 m/s), while maintaining $C_3 = 1$ MHz μm^3 and $\gamma = 25$ MHz. An atom travelling at a higher velocity explores greater depths along the z compared to a slower one. Consequently, $\mathcal{I}$ converges faster for lower velocities (for $v_z = 100$ m/s, convergence occurs around $L \sim 6.5$ μm, whereas for $v_z = 10$ m/s, convergence is achieved at $L \sim 4.5$ μm).

Finally, in Figure 3.7 (c), we explore the convergence of $\mathcal{I}$ for two different values of the C_3 coefficient (1 MHz μm^3 and 5 MHz μm^3). A higher C_3 coefficient signifies a more pronounced atom-surface shift, allowing the atom to explore greater depths along the z and $\mathcal{I}$ convergences at larger values of L. It's worth noting that the term $\exp(i\mathcal{C}/z^2)$ diminishes rapidly with increasing z. Consequently, the impact of C_3 on the convergence of $\mathcal{I}$ becomes relatively minor especially with chosen C_3 variation.

Most importantly, $\mathcal{I}$ tends to converge to a stable value when an appropriate cutoff point L is chosen. For this numerical approach, we have used the appropriate L values for a broad spectrum of γ, δ, v_z, and C_3 combinations to ensure the convergence of $\mathcal{I}$ (amplitude variation of $\mathcal{I} < 0.00001\%$).

3.2.1.2 Truncation of $\mathcal{H}(z)$ with an analytical function

As mentioned previously, $\mathcal{H}(z)$ varies rapidly for small values of z (transient regime) and eventually reaches a periodic oscillatory (steady-state) regime as z increases. In the steady state regime the influence of atom-surface interactions ($\exp(i\mathcal{C}/z^2)$ term) is negligible. For this solution, we assume that $\mathcal{H}(z)$ represents the response in the presence of atom-surface interaction, while $\mathcal{H}_0(z)$ represents the response in the absence of atom-surface interaction. By subtracting the response with atom-surface interaction from the response without atom-surface interaction, we introduce what we refer to as "natural losses" to the function. In the steady-state regime, these two functions will overlap and cancel each other perfectly, ensuring the convergence of the integral $\mathcal{I}$ (figure 3.8). Recalling equation 3.33, we have:

$$\mathcal{I} = \int_0^{+\infty} dz\,[\mathcal{H}(z) - \mathcal{H}_0(z)] + \int_0^{+\infty} dz\mathcal{H}_0(z) \tag{3.37}$$

where $\mathcal{H}_0(z)$ is given by:

$$\mathcal{H}_0(z) = e^{(2ikz)} \cdot e^{[-\mathcal{A}z + i\mathcal{B}z)]} \int_0^z dz' \cdot e^{[\mathcal{A}z - i\mathcal{B}z']} \tag{3.38}$$

where $\mathcal{A} = (\gamma/2v_z)$, $\mathcal{B} = (\delta - kv_z)/v_z$.

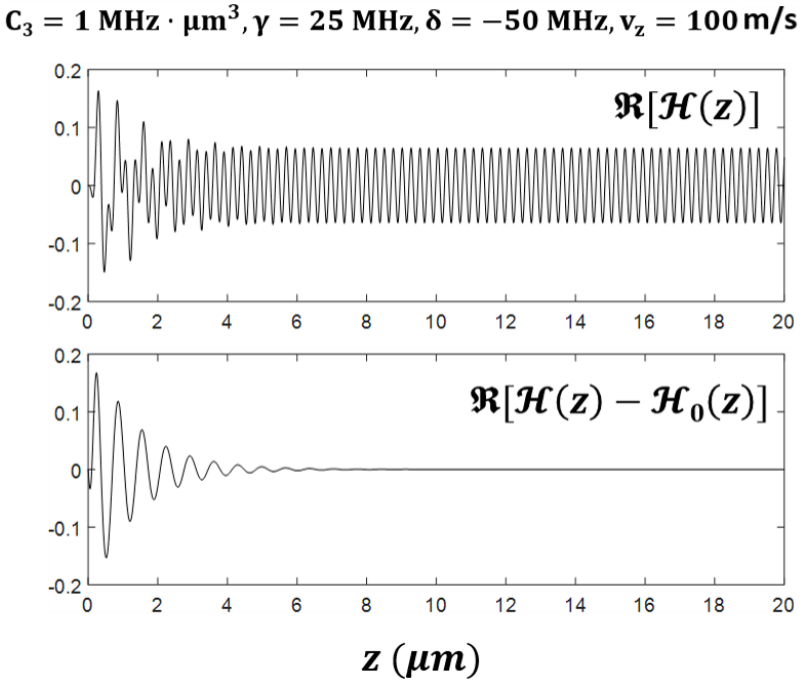

Figure 3.8: $\Re[\mathcal{H}(z)]$ and $\Re[\mathcal{H}(z) - \mathcal{H}_0(z)]$ as a function of z (in μm).

Similarly, we define $\mathcal{I}_{th}$ which refers to $\mathcal{I}$ in the absence of atom-surface interaction, given

by:

$$\begin{aligned}\mathcal{I}_{th} &= \int_0^{+\infty} dz \mathcal{H}_0(z) \\ &= \lim_{A\to 0} \int_0^{+\infty} dz \cdot \underbrace{e^{2ikz} \frac{1 - e^{-(\mathcal{A}-i\mathcal{B})z}}{\mathcal{A} - i\mathcal{B}}}_{\mathcal{H}_0(z)} e^{Az} \\ &= \frac{i}{2k(-2ik + \mathcal{A} - i\mathcal{B})}\end{aligned} \tag{3.39}$$

Finally, substituting 3.39 into 3.37, we can obtain the integral $\mathcal{I}$ as:

$$\mathcal{I} = \int_0^{+\infty} dz \left[\mathcal{H}(z) - \mathcal{H}_0(z)\right] + \frac{i}{2k(-2ik + \mathcal{A} - i\mathcal{B})} \tag{3.40}$$

The convergence of $\mathcal{I}$ with these natural losses was also examined in the same systemic way as discussed in the previous section. With this method, for a well-chosen upper boundary in z, the convergence of $\mathcal{I}$ was well within 0.00001%, resulting in identical values. The determining factor in choosing between these two methods boils down to computational speed. For cumulative summing, Matlab was more suitable for predefined integration limits and coding complexity was a bit simpler with the Logistic function. Thus the integration time was a bit faster for the Logistic function. For the results presented in this thesis, the logistic function was chosen to introduce losses.

3.2.2 Selective reflection lineshapes for different atomic velocities

After solving the z and z' integrals, it is rather straightforward to perform the integration over velocities v_z with the appropriate weight factors defined by the Maxwell-Boltzmann distribution. It is noteworthy to mention that the validity of the Maxwell-Boltzmann atomic velocity distribution in the vicinity of a reflecting surface is an ongoing subject of research [62].

Figure 3.9 presents the SR lineshape (excluding the weight factors) for $C_3 = 1$ MHz μm^3, $\gamma = 100$ MHz showcasing the influence of different atomic velocities v_z. As the velocity v_z approaches zero, the SR signal reassuringly converges towards the curve at $v_z = 0$ (equation 3.31). With increasing velocity, the atoms explore larger depths along z. Si-

multaneously, the resonance shifts to a higher red detuning. At these greater depths, the term $\exp(i\mathcal{C}/z^3)$ diminishes rapidly and the atom starts to experience the phase of the driving field $\exp(2ikz)$, which in turn, leads to a modification in the phase of the SR signal.

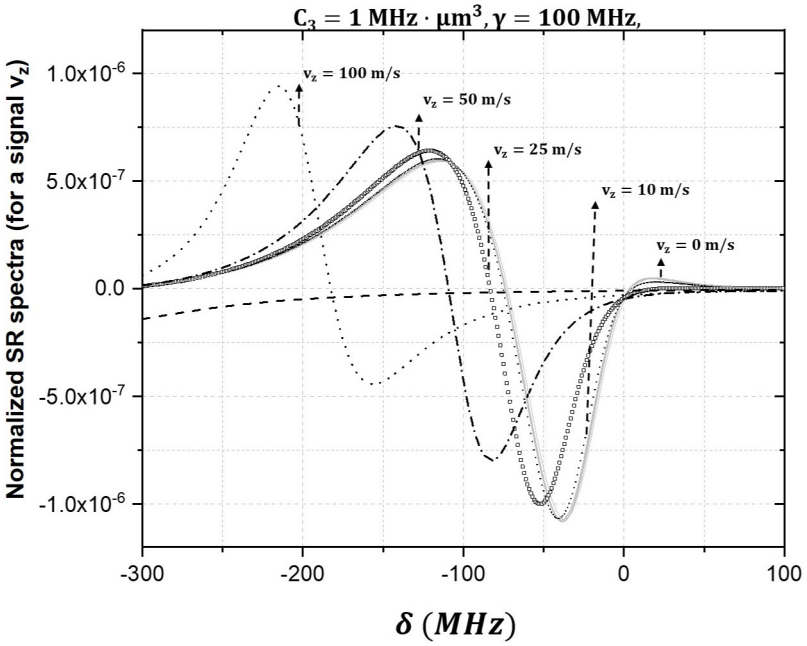

Figure 3.9: Selective reflection lineshape with $C_3 = 1$ MHz μm^3, $\gamma = 100$ MHz for different atomic velocities (v_z).

3.2.3 Selective reflection lineshape for different atomic velocity distribution and atom-surface interactions

3.2.3.1 For weak dipole-dipole interaction

In figure 3.10, we present normalized FMSR lineshapes (normalized to maximum amplitude) for C_3 =10 kHz μm^3 and γ = 15MHz with different velocity distributions: the infinite Doppler and motionless atom approximation (marked with arrows) and Maxwell-Boltzmann distribution for different thermal velocities (marked with different markers). With a temperature of T = 0.002 K, it is reasonable to assume that the Maxwell-Boltzmann distribution is sufficiently narrow and most of the atoms are moving very slowly simulating the condition for $v_z \to 0$. The simulated FMSR lineshape for T = 0.002 K, converges nicely to the analytical solution for $v_z = 0$ (equation 3.31, indicated

by arrow). With increasing temperatures to higher values, MB distributions practically broaden, simulating the conditions for which the infinite Doppler approximation is valid. The convergence of the simulated SR lineshape for T = 500 K (the usual operating temperature of the surface) to the infinite Doppler approximation (equation 3.30) is acceptable especially close to $\delta \to 0$. However, a small divergence can be observed on the "wings" (for higher negative detuning). This can be attributed to the fact that the infinite Doppler condition might not be fully valid (with γ = 15 MHz, Doppler FWHM 600 MHz). On increasing the temperature to T = 8000 K where the Doppler width is about 2.5 GHz » the linewidth, γ = 15 MHz, the simulated SR lineshape converges to the Doppler limited solution almost perfectly.

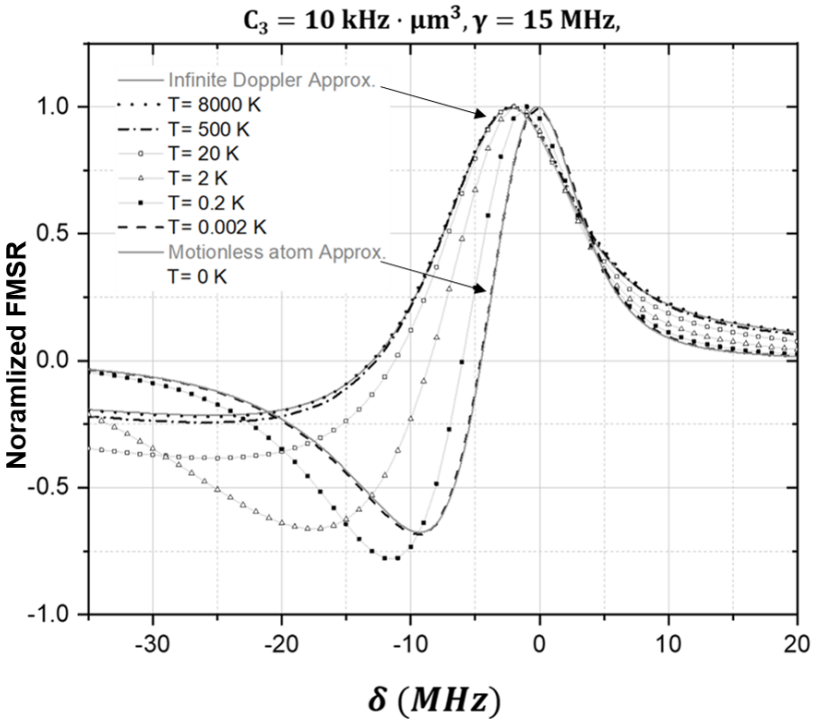

Figure 3.10: Normalized FMSR lineshapes (normalized to maximum amplitude) for different thermal velocity distributions. The infinite Doppler and motionless atom approximations are marked with arrows. Here, C_3 = 10 kHz μm^3 and γ = 15 MHz.

3.2.3.2 For strong dipole-dipole interaction

Figure 3.11 shows the normalized FMSR lineshape (normalized to the maximum amplitude) for $C_3(17D_{3/2})$ = 8.8 MHz μm^3 and γ = 50 MHz (most excited relevant Rydberg

state) considering different velocity distributions: the motionless atom approximation (in dotted line), infinite Doppler approximation (in dashed line) and Maxwell Boltzmann (MB) distribution at T=500 K (in solid line). Close to resonance ($\delta \to 0$) where the atom surface shifts are small ($\sim$ -100 MHz) compared to the Doppler width (about $\sim$ 600 MHz), the divergence between MB (in solid line) and Doppler-limited (in dashed line) FMSR lineshape is negligible. But for higher negative detuning, especially in the 'wing' of the FMSR lineshape where the atom surface shift (more than -500 MHz) becomes comparable to the Doppler width, Doppler-limited approximation is no longer valid and we observe a strong divergence between the MB and the Doppler-limited FMSR lineshapes. Meanwhile, the SR lineshape due to motionless approximation (in dotted line) appears narrower than the other two lineshapes, since we have excluded the effect of atomic motion. Nevertheless, neither the Doppler-limited approximation nor the motionless atom approximation is adequate for explaining Rydberg atom-surface interactions.

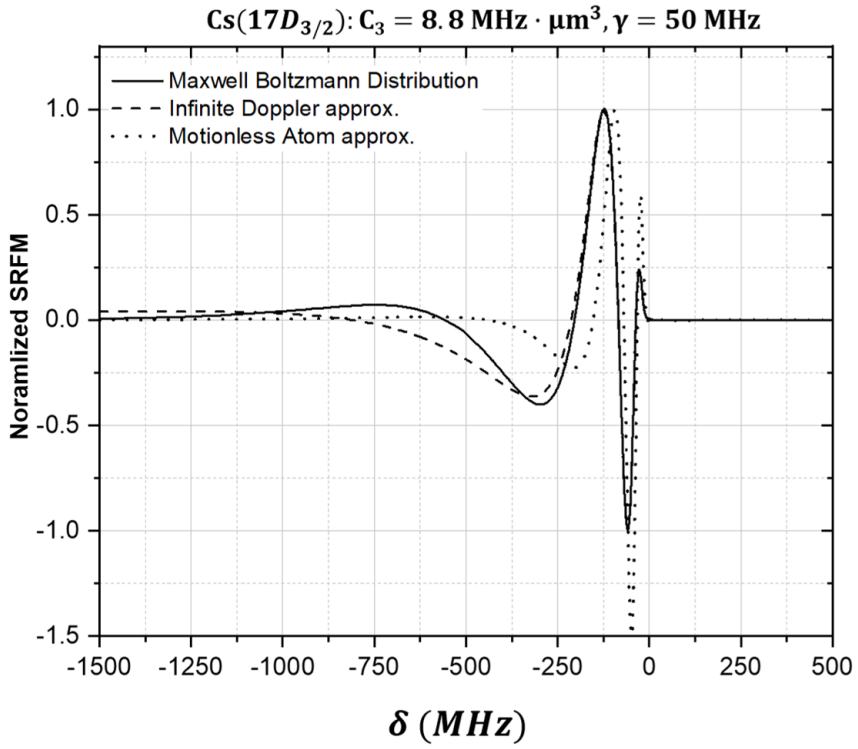

Figure 3.11: Normalized FMSR lineshape (normalized to the maximum amplitude) for $C_3(17D_{3/2}) = 8.8$ MHz μm^3 and $\gamma = 50$ MHz considering the motionless atom approximation (dotted line), infinite Doppler approximation (dashed line) and Maxwell Boltzmann (MB) distribution with T = 500 K (in solid line).

3.2.3.3 For strong atom surface interaction including quadrupole interactions term

The addition of the quadrupole interaction term in the numerical solution is a relatively straightforward process with introducing a newly defined lineshape function $\mathcal{L}(z, v_z)$ that includes both the dipole-dipole(image) and quadrupole-quadrupole (image) interaction terms, given by:

$$\begin{aligned}\mathcal{L}(z, v_z) &= -\frac{\gamma}{2v_z}z + i\frac{\delta - kv_z}{v_z}z - \left[i\frac{C_3}{2v_z}\frac{1}{z^2}\right] - \left[i\frac{C_5}{4v_z}\frac{1}{z^4}\right] \\ &= -\mathcal{A}z + i\mathcal{B}z - i(\mathcal{C}/z^2) - i(\mathcal{D}/z^4)\end{aligned} \tag{3.41}$$

where $\mathcal{A} = (\gamma/2v_z)$, $\mathcal{B} = (\delta - kv_z)/v_z$, $\mathcal{C} = C_3/2v_z$ and $\mathcal{D} = C_5/4v_z$.

Figure 3.12 shows the normalized SR lineshape (normalized to the maximum amplitude) for $C_3(17D_{3/2}) \sim 8.8$ MHz μm^3 (in solid line) and $C_3(17D_{3/2}) \sim 8.8$ MHz μm^3 & $C_5(17D_{3/2})$ & 2.07 kHz μm^5 (in dashed line) having a homogeneous linewidth, $\gamma = 50$ MHz.

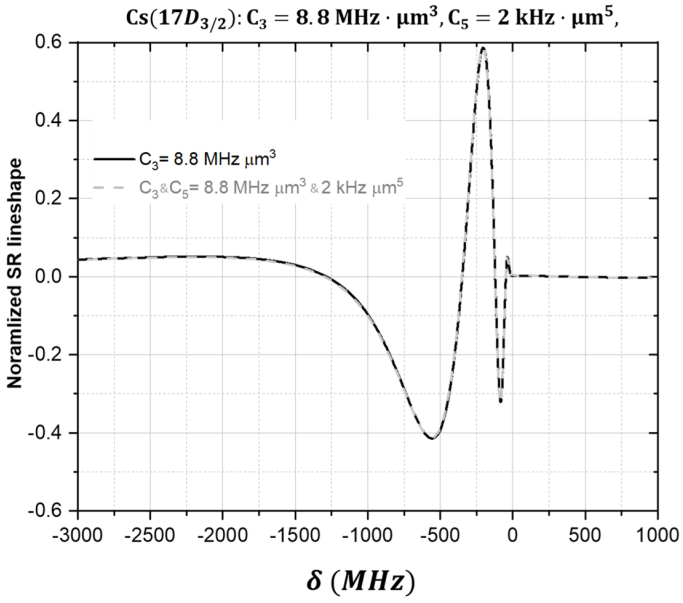

Figure 3.12: Normalized SR lineshape (normalized to the maximum amplitude) for $C_3(17D_{3/2})$ (solid line: ~ 8.8 MHz μm^3) and $C_3(17D_{3/2})$ & $C_5(17D_{3/2})$ (grey dashed line: ~ 8.8 MHz μm^3 & 2.07 kHz μm^5) having a homogeneous linewidth, $\gamma = 50$ MHz.

The introduction of the quadrupole term has a negligible effect on the SR lineshape. The strongest contrast of SR lineshape corresponds to larger atom surface separations (z) where the atom-surface shifts are relatively large. For these large atom surface separations, the influence of the quadrupole term C_5 (which scales as $1/z^5$) diminishes rapidly when compared to the dominant C_3 term (which scales as $1/z^3$). To explore higher-order interaction effects, it becomes necessary to probe atoms at much shorter atom-surface separations. However, in the SR technique, the probing depth is inherently defined by the atom-surface shifts, which limits its appropriateness for observing higher-order interaction terms.

One possible approach to probe atoms even closer to the surface would be using a nanometric cell with varying thicknesses giving us an effective control over the probing depth. This was one of the key motivations behind our decision to perform experiments in such a cell. In the following sections, we briefly discuss thin-cell (TC) spectroscopy and our numerical approach for simulating TC lineshapes.

3.3 Nanometric thin cell spectroscopy (TC)

Nanometric thin cell spectroscopy is a well-established method of probing Casimir Polder interactions [23][63]. The thin cell, we use consists of two dielectric surfaces (made of YAG) separated by a nanometric spacer [64][65] (figure 3.13). The two surfaces buckle under atmospheric pressure giving rise to a thickness gradient of 50 nm - 1000 nm.

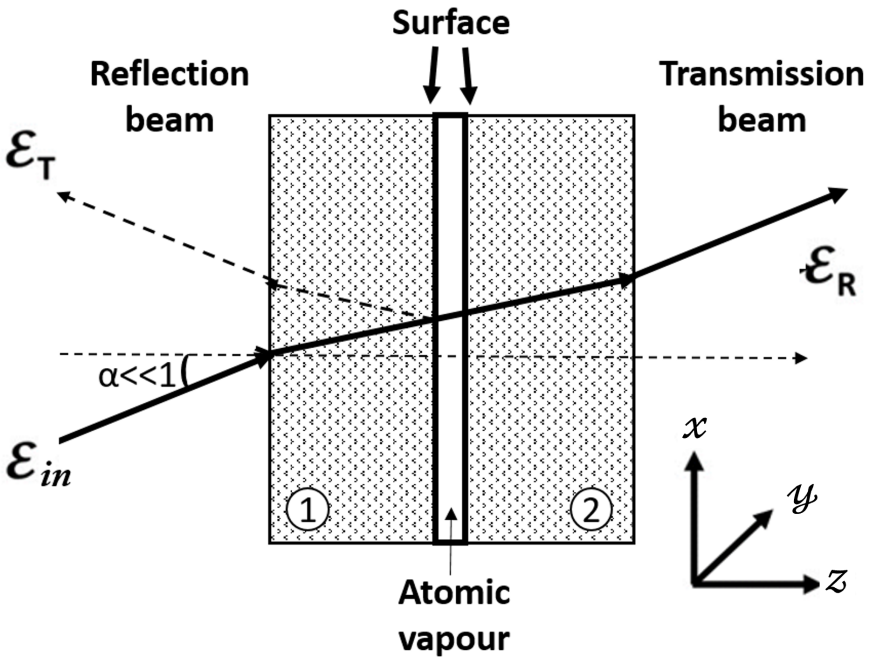

Figure 3.13: Transmission path of a near normal incident beam $\mathcal{E}_{in}$ through the thin cell which acts as a low finesse Fabry–Pérot interferometer. $\mathcal{E}_R$, and $\mathcal{E}_T$ is the reflected and transmitted field respectively. $\alpha \ll 1$ is the incident angle which has been deliberately upscaled in the figure for convenience. $z > 0$ is the direction of propagation.

$\mathcal{E}_{in}$ is the incident beam (α=0, coming from the surface 1 side) and $\mathcal{E}_R$ and $\mathcal{E}_\mathcal{T}$ are the reflected and transmitted fields respectively. Due to the parallelism of our cell, Only one reflected beam ($\mathcal{E}_R$) can be observed from the vapour-surface interface. The cell acts as a low finesse Fabry–Pérot (FP) micro-cavity of cavity length L and any thickness gradient effects are also neglected. Throughout this calculation, a diluted atomic vapour is considered for which the optically thin medium approximation is valid [51] i.e. the absorption of the incident field is negligible.

3.3.1 Nanometric thincell as Fabry–Pérot (FP) cavity

3.3.1.1 Mixing of reflection and transmission response

The incident field $\mathcal{E}_{in}$ (tuned to the atomic resonance) introduces macroscopic polarization in the atomic vapour. In the limit of a dilute medium (i.e. the absorption is negligible compared to $\mathcal{E}_{in}$), the field $\mathcal{E}'_o(z)$ that drives the atomic polarization $P(z)$ in the medium is essentially the field of an empty FP, given by [52][51]:

$$\mathcal{E}'_o(z) = \mathcal{E}_{in} \cdot \frac{2n}{n+1} \cdot [1 - r \cdot \exp(2ik(z-L))]/\mathcal{F} \tag{3.42}$$

where

- $k = 2\pi/\lambda$ is the wavevector where λ is the incident wavelength.
- $r = (n-1)/(n+1)$ is the reflectivity of the surface (both surfaces possess identical reflectivity).
- $\mathcal{F} = 1 - [r^2 \cdot \exp(2ikL)]$ is the complex finesse of the cavity.

In the limit of optically thin medium approximation [51] (atomic response remains linear to the excitation field), the linear reflection (I_R^{lin}) and transmission (I_T^{lin}) signal neglecting any internal reflections inside the cell can be obtained as:

$$I_R^{lin} = \frac{\eta r_0 \rho}{\mathcal{F}} \cdot \left[\int_0^{+\infty} \frac{dv_z}{v_z} [W(v_z) + w(-v_z)] \int_0^L dz \int_0^z dz' e^{2ikz} e^{[\mathcal{L}(z') - \mathcal{L}(z)]/v_z} \right] \tag{3.43}$$

$$I_T^{lin} = \frac{\eta r_0 \rho}{\mathcal{F}} \cdot \left[\int_0^{+\infty} \frac{dv_z}{v_z} [W(v_z) + w(-v_z)] \int_0^L dz \int_0^z dz' e^{[\mathcal{L}(z') - \mathcal{L}(z)]/v_z} \right] \tag{3.44}$$

where, the lineshape function, $\mathcal{L}(z)$ is given as:

$$\mathcal{L}(z) = \frac{\gamma}{2v_z} z + i\frac{\delta - kv_z}{v_z} - i\frac{C_3}{2v_z}\left[\frac{1}{z^2} - \frac{1}{(L-z)^2}\right] - i\frac{C_5}{2v_z}\left(\frac{1}{z^4} - \frac{1}{(L-z)^4}\right) \tag{3.45}$$

Here, we consider that the Casimir-Polder interaction in the cavity is simply the sum of the interactions of the atom with two walls (the effects of multiple images will be discussed later).

If we take into account the internal reflection due to the FP structure of the cell, it mixes

the reflection and transmission response (Equation 3.43 and 3.44) and these mixed signal can be given as [51]:

$$I_f = \left[I_T^{lin} - r \cdot I_R^{lin}\right] \tag{3.46}$$

$$I_b = \left[I_R^{lin} - \left(r \cdot I_T^{lin} \cdot e^{2ikL}\right)\right] \tag{3.47}$$

For a dilute atomic vapour, the atomic medium becomes transparent for most of the incident field and this field will propagate back and forth through the cell length (L). The respective resonant transmission and reflection signals given by S_T and S_R can be interpreted as a homodyne beating between the mixed signals (I_f and I_b) and the transmitted (reflected) field of an empty FP cavity of length, L. The mixed transmission (S_T) and reflection signal (S_R) are expressed as [51]:

$$S_T = \Re[I_f - 2 \cdot r \cdot I_b]/|\mathcal{F}|^2 \tag{3.48}$$

$$S_R = \Re[r \cdot (1 - e^{-2ikL}) \times (I_b - r \cdot I_f \cdot e^{2ikL})]/|\mathcal{F}|^2 \tag{3.49}$$

3.3.1.2 Effect of multiple images

Due to the good parallelisms of two reflecting surfaces, we can introduce a minor adjustment to our lineshape function (equation 3.45) to account for the formation of multiple images [52] (figure 3.14).

We assume that the atom is placed at a distance z from surface 1 and $L-z$ from surface 2 (figure 3.14). The surface-induced images: image (**1**) and image (**2**) will be at a distance $2z$ and $2(L-z)$ with respect to (w.r.t) the position of the atom. The image (**1**) will produce an image of itself (**1**') with the far side surface (i.e. surface 2) at a distance $2L$ w.r.t to the position of the atom. Similarly, the image (**2**) will also create an image of itself (**2**') with the far side surface (now i.e. surface 1) at a distance $2(L-z)$ and so on. The position of the images w.r.t the position of the atom will evolve as:

- For Image (**1**) the next images will be positioned at : $2z$, $2L$, $2L$+$2z$, $4L$, $4L$+$2z$, ...
- For Image (**2**) the next images will be positioned at: $2(L$-$z)$, $2L$, $2L$+$2(L$-$z)$, $4L$,

$4L$+2(L-z) ,. . .

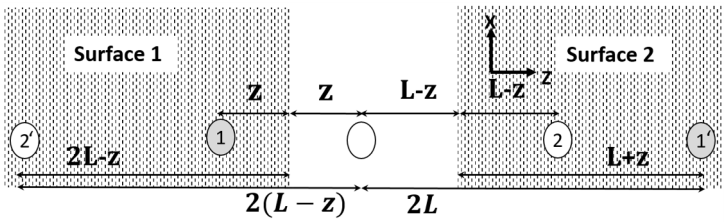

Figure 3.14: Thin cell with multiple images where the atom is placed at a distance z from surface 1 and $L - z$ from surface 2.

This evolution of the position of the images can be put in an analytical form, such as :

$$\sum_n \frac{1}{[z+nL]^2} - \sum_n \frac{1}{[(L-z)+nL]^2} = \frac{1}{L^2}\left[\sum_n \frac{1}{[z/L+nL]^2} - \sum_n \frac{1}{[(L-z)/L+nL]^2}\right] = \Psi^{(1)}\left(\frac{z}{L}\right) - \Psi^{(1)}\left(\frac{L-z}{L}\right) \tag{3.50}$$

where $\Psi^{(1)} = \frac{d^2}{dz^2}\ln(\Gamma(z))$ is the tri-gamma function [66].

Subsequently, the modified lineshape function in the presence of multiple images can be given as (considering only dipole-dipole (image) interaction):

$$\mathcal{L}(z) = \frac{\gamma}{2v_z}z + i\frac{\delta - kv_z}{v_z} - i\frac{C_3}{2v_z}\left[\Psi^{(1)}\left(\frac{z}{L}\right) - \Psi^{(1)}\left(\frac{L-z}{L}\right)\right] \tag{3.51}$$

The modification introduced by second-order images (**1**',**2**') is negligible ($< 5\%$) compared to the response due to first-order images (**1**,**2**). With the increasing order of the images (**1**",**2**",..), the atom surface separation also increases and its corresponding response becomes even more insignificant compared to the first-order images.

3.3.2 Thin cell (TC) lineshape in the presence of strong atom surface interactions

The numerical solution to thin-cell lineshape is less complicated than the SR lineshape, because, unlike the SR case, the integrals I_R^{lin} and I_T^{lin} naturally converge as they are bound between the cell walls [0, L].

$$I_R^{lin} = \frac{\eta r_0 \rho}{\mathcal{F}} \cdot \left[\int_0^{+\infty} \frac{dv_z}{v_z} [W(v_z) + w(-v_z)] \int_0^L dz \int_0^z dz' e^{2ikz} e^{[\mathcal{L}(z') - \mathcal{L}(z)]/v_z} \right]$$

$$I_T^{lin} = \frac{\eta r_0 \rho}{\mathcal{F}} \cdot \left[\int_0^{+\infty} \frac{dv_z}{v_z} [W(v_z) + w(-v_z)] \int_0^L dz \int_0^z dz' e^{[\mathcal{L}(z') - \mathcal{L}(z)]/v_z} \right]$$

Simulation of the TC lineshape by mixing reflection and transmission signal and homodyne beating becomes somewhat trivial, which is given by:

$$S_T = \Re \left[\left(I_T^{lin} - r \cdot I_R^{lin} \right) - 2 \cdot r \cdot \left(I_R^{lin} - r \cdot I_T^{lin} \cdot e^{2ikL} \right) \right] / |\mathcal{F}|^2$$

$$S_R = \Re \left[r \cdot (1 - e^{-2ikL}) \times \left\{ \left(I_R^{lin} - r \cdot I_T^{lin} \cdot e^{2ikL} \right) - r \cdot \left(I_T^{lin} - r \cdot I_R^{lin} \right) \cdot e^{2ikL} \right\} \right] / |\mathcal{F}|^2$$

So instead of going into the details of the numerical procedure, we present the TC lineshapes for different cell thicknesses and examine the conditions under which higher-order interactions can be experimentally observable.

In figure 3.15 and 3.16, we present simulated $6P_{1/2} \rightarrow 16S_{1/2}$ TC lineshapes (transmission (TS) and reflection (RS) spectra) for different cell thicknesses with $C_3(16S_{1/2}) \sim 4.1$ MHz μm^3 (in dashed lines) and $C_3(16S_{1/2}) \sim 4.1$ MHz μm^3 & $C_5(16S_{1/2}) \sim 0.45$ kHz μm^5 (in solid line) considering a Maxwell-Boltzmann (MB) distribution with a probable velocity of $v_p = 250$ m/s. For simulating TC lineshapes, we have taken the reflection coefficient of both windows to be $r = 0.29$. We have also considered the internal mixing of the transmission I_T^{lin} and reflection signal I_R^{lin} as well as the homodyne beating of the mixed signal with the empty FP but we have excluded the effects of multiple images.

We show transmission (TS) and reflection signals (RS), normalized to their maximum amplitude, for two different homogeneous linewidths marked as A ($\sim$ 200 MHz) and B ($\sim$ 1000 MHz). We have also divided the lineshape into two parts depending on the cell thickness: cell thickness bigger than $\lambda/2$ (figure 3.15) where λ is the transition wavelength ($\sim$ 514 nm) and cell thickness smaller than $\lambda/2$ (figure 3.16).

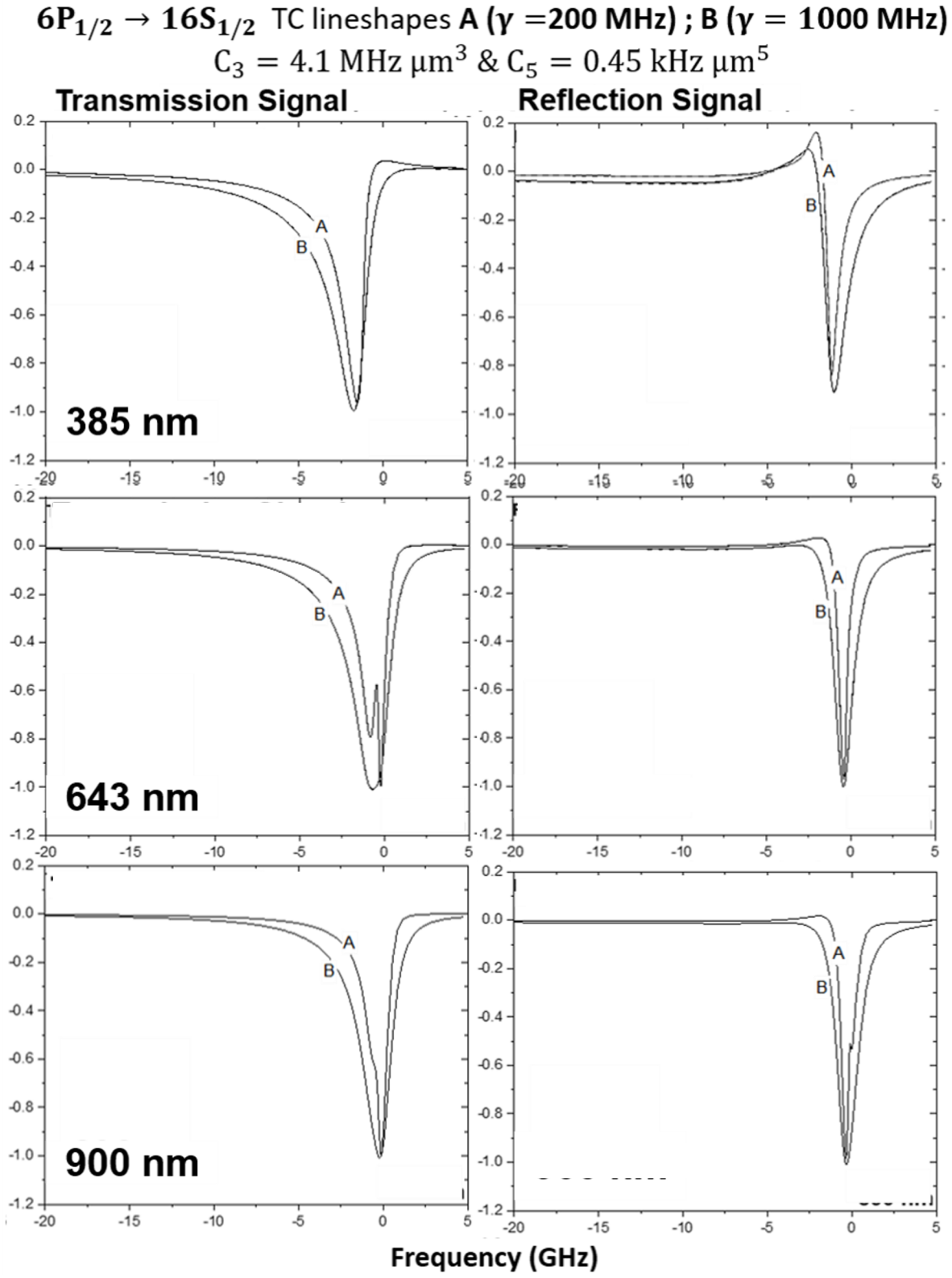

Figure 3.15: Normalized transmission (TS) and reflection (RS) spectra as a function of cell thickness (L>$\lambda/2$ where λ = 514 nm) with $C_3(16S_{1/2})$ (dashed lines: $\sim$ 4.1 MHz μm^3) and $C_3(16S_{1/2})$ & $C_5(16S_{1/2})$ (solid line: $\sim$ 4.1 MHz μm^3 & 0.45 kHz μm^5). Signal amplitude is normalized to the maximum amplitude of the signal. A and B correspond to γ = 200, 1000 MHz respectively. When the thickness is an integral multiple of $\lambda/2$ (514 nm and 771 nm) the reflection signal (RS) becomes zero.

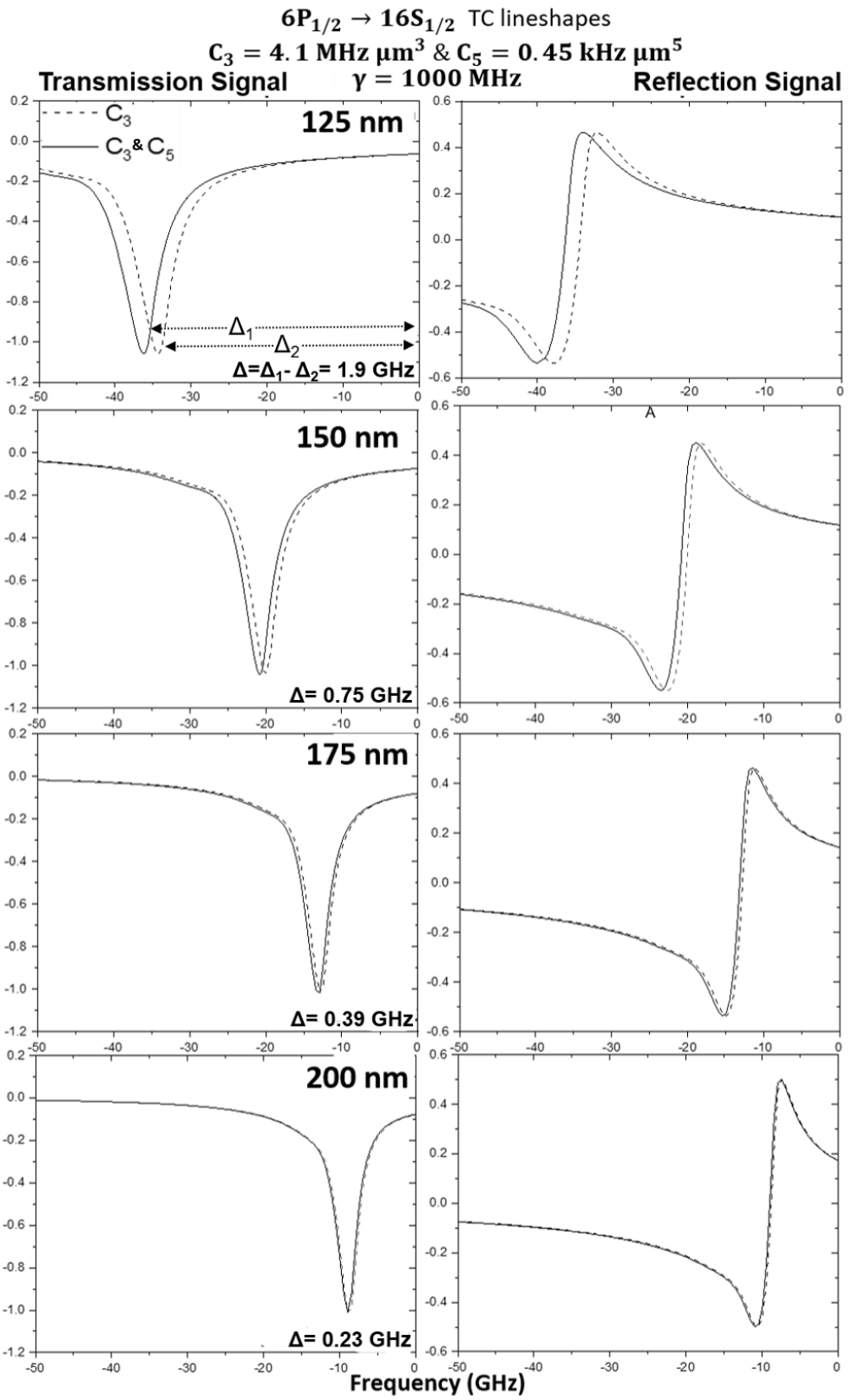

Figure 3.16: Normalized transmission (TS) and reflection (RS) spectra as a function of cell thickness (L>$\lambda/2$ where $\lambda = 514$ nm) with $C_3(16S_{1/2}) \sim 4.1$ MHz μm^3 (dashed lines) and $C_3(16S_{1/2}) \sim 4.1$ MHz μm^3 & $C_5(16S_{1/2}) \sim 0.45$ kHz μm^5 (solid line). Signal amplitude is normalized to the maximum amplitude of the signal. $\Delta = \Delta_1(C_3 + C5) - \Delta_2(C_3)$, additional redshift of the dip for considering quadrupole interactions.

For large cell thicknesses L>$\lambda/2$ where $\lambda = 514$ nm (figure 3.16) the dipole interaction is the dominating term and quadrupole interactions are irrelevant (dashed and solid lines almost overlap). However, it is interesting to notice that, for some specific cell thicknesses, like 514 or 643, some narrow features can be observed for a smaller γ value (A) and diminish for a larger value of γ (B). In our initial, investigation we found that these narrow features depend on C_3, γ and also on cell thickness L. In our preliminary experiment on TC spectroscopy (chapter 6), we observed some reminiscence of these narrow features. An intuitive hypothesis for these narrow features would be the mixing of the transmission and reflection signal or related to the mixing of "the CP interactions" with the "Dicke effects" [67] as it depends on C_3 and as well as on L. This behaviour is yet to be understood and warns further investigation.

For small cell thickness L<$\lambda/2$ (figure 3.15), we have compared TC Transmission (TS) and Reflection (RS) spectra as a function of cell thickness with $C_3(16S_{1/2}) \sim 4.1$ MHz μm^3 (dashed lines) and $C_3(16S_{1/2}) \sim 4.1$ MHz μm^3 & $C_5(16S_{1/2}) \sim 0.45$ kHz μm^5 (solid line) having $\gamma = 1000$ MHz. With decreasing cell thickness, increasing discrepancies can be observed between the two lineshapes. An additional redshift of the lineshape can be observed by taking into account the quadrupole interaction (solid line) compared to the lineshape only considering dipole interaction (dashed line). This additional shift becomes more prominent for smaller cell thickness (i.e. at smaller atom-surface separations). Most importantly, by tracking this additional shift (denoted as Δ in figure 3.16), we can establish a method to estimate the cell thickness at which the manifestation of higher-order interactions becomes experimentally observable. For instance, with the presence of the quadrupole interaction, one can expect an additional redshift of approximately 2 GHz of the resonance for a cell thickness of 125 nm which is about half of the FWHM of the linewidth. This information can be crucial for designing experiments and optimizing conditions to probe higher-order interactions effectively.

Figure 3.17 shows the trace of the additional redshift in TC transmission lineshapes

due to the presence of the quadrupole interactions as a function of cell thickness for some relevant Rydberg states. With higher Rydberg states, the influence of higher-order interactions becomes discernible even at larger atom surface separations, necessitating corrections beyond the dipole approximation.

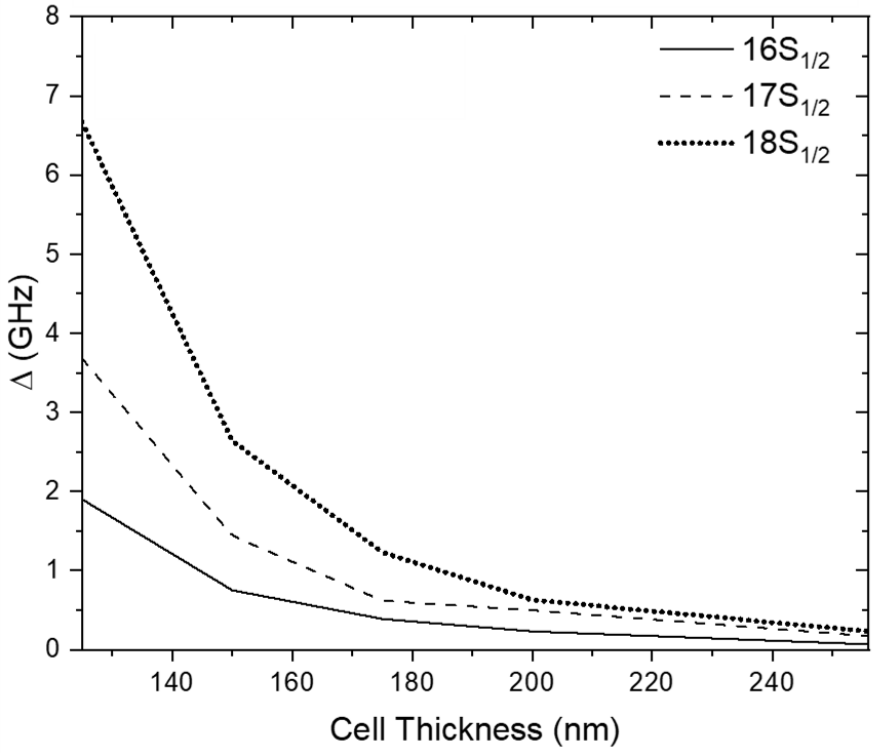

Figure 3.17: Additional redshift of the atomic resonance as a function of cell thickness in the presence of the quadrupole-quadrupole interactions for some relevant Rydberg states.

Chapter 4

Description of the atomic system and experimental setup

This chapter focuses on the experimental setup used for measuring the Casimir Polder interactions between Rydberg states $[6P_{1/2} \rightarrow nS_{1/2}, nD_{3/2}(n = 15 - 18)]$ using selective reflection (SR) and thin cell (TC) spectroscopy. The experimental setup can be divided into two main parts. The first part involves conducting absorption spectroscopy in a microscopic cell (where spectroscopic measurements are not influenced by atom-surface interaction) which acts as a frequency reference. In conjunction with absorption spectroscopy we have measured the Casimir-Polder interaction with an independent setup using selective reflection or thin cell spectroscopy.

In Section 4.1, we introduce the general spectroscopic scheme which involves a step-wise excitation process to probe the Rydberg States. The initial step consists of optically exciting atoms from $6S_{1/2} \rightarrow 6P_{1/2}$ using an 894 nm laser. Subsequently, we probe the atoms to $6P_{1/2} \rightarrow nS_{1/2}, nD_{3/2}$ states using an extended cavity laser having a wavelength range of 510 - 514 nm. In Section 4.2, we provide a comprehensive description of the experimental setup highlighting key components such as the lasers, vapour cells, data acquisition and detection system. Section 4.3 provides a brief overview of the volume experiment

(sub-Doppler velocity-selective $6P_{1/2} \rightarrow nS_{1/2}, nD_{3/2}$ absorption spectra) which acts as frequency references in volume. Additionally, we present our experimental measurements of homogeneous linewidth broadening for the $6P_{1/2} \rightarrow 15D_{3/2}$ transition as a function of Caesium vapour pressure.

4.1 Caesium atomic levels and spectroscopic scheme

Figure 4.1 shows the Caesium energy levels relevant to our experiments: the fundamental state Cs($6S_{1/2}$), the first excited state Cs($6P_{1/2}$) and all accessible Rydberg states Cs($nS_{1/2}$, $nD_{3/2}$).

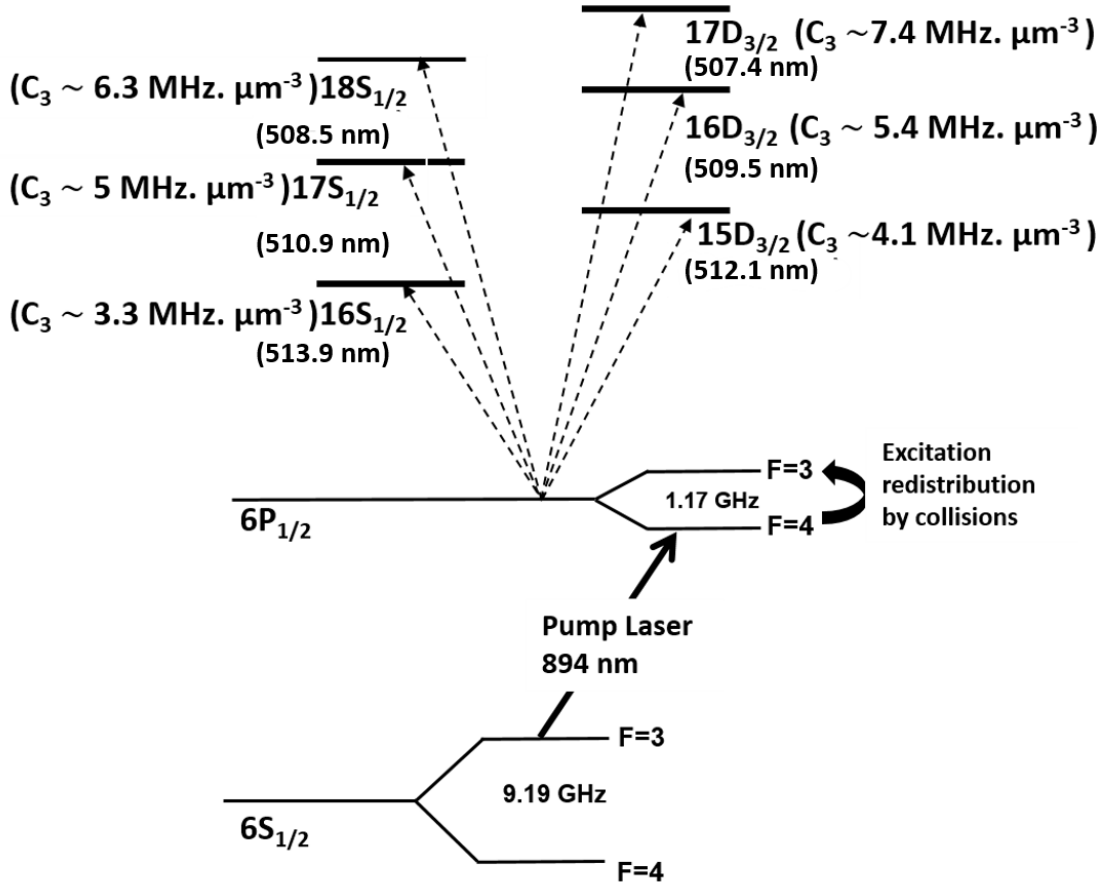

Figure 4.1: Step-wise excitation scheme for probing Rydberg state. Pumping from $6S_{1/2}(F = 3) \rightarrow 6P_{1/2}(F = 4)$ at 894 nm and probing $6P_{1/2}(F = 4, 3) \rightarrow nS_{1/2}, nD_{3/2}$ (n = 15 - 18) at 507 - 513 nm.

To reach the relevant Rydberg state, we use a step-wise excitation, firstly pumping the

atoms from any of the hyperfine components of the ground state Cs($6S_{1/2}$) to any of the hyperfine components of the first excited state Cs($6P_{1/2}$) (D_1 line) with an 894 nm laser and subsequently probing on the $6P_{1/2} \rightarrow nS_{1/2}, nD_{3/2}$ transitions (for n = 15 - 18) with a green laser emitting at 507 - 513 nm.

Caesium ground state Cs($6S_{1/2}$) has two hyperfine components (F=4, 3) separated by $\sim$ 9.19 GHz. Atoms are pumped from one of the hyperfine states of Cs($6S_{1/2}$) to the first excited state Cs($6P_{1/2}$) (in the figure $6S_{1/2}(F = 3) \rightarrow 6P_{1/2}(F' = 4)$). Due to collisions, the excitations are redistributed among both hyperfine components $6P_{1/2}$ state which are separated by 1.17 GHz. So, on probing the Rydberg states from $6P_{1/2}$, we obtain responses for the both hyperfine components of $6P_{1/2}$(F=4,3). Similar configurations have been used in previous studies to measure CP interaction of low-lying states using selective reflection (SR) spectroscopy [45][38][68] where this collisional redistribution was exploited by assuming a quasi-thermal velocity distribution. The separation between the hyperfine components of the $nS_{1/2}$ and $nD_{3/2}$ levels are within a few MHz [69][31][30], making it impossible to resolve in our experimental conditions. Table 4.1, shows the accessible Rydberg states and their transition wavelength from $6P_{1/2}$ state.

Probing states from $6P_{1/2}$	Transition wavelength (nm)
$15D_{3/2}$	512.06871
$16S_{1/2}$	513.88478
$16D_{3/2}$	509.46958
$17S_{1/2}$	510.88788
$17D_{3/2}$	507.40752
$18S_{1/2}$	508.35371

Table 4.1: Accessible Rydberg states and their transition wavelength from $6P_{1/2}$ state.

On the next page, we provide a schematic of our experimental setup highlighting some of the key components of the setup.

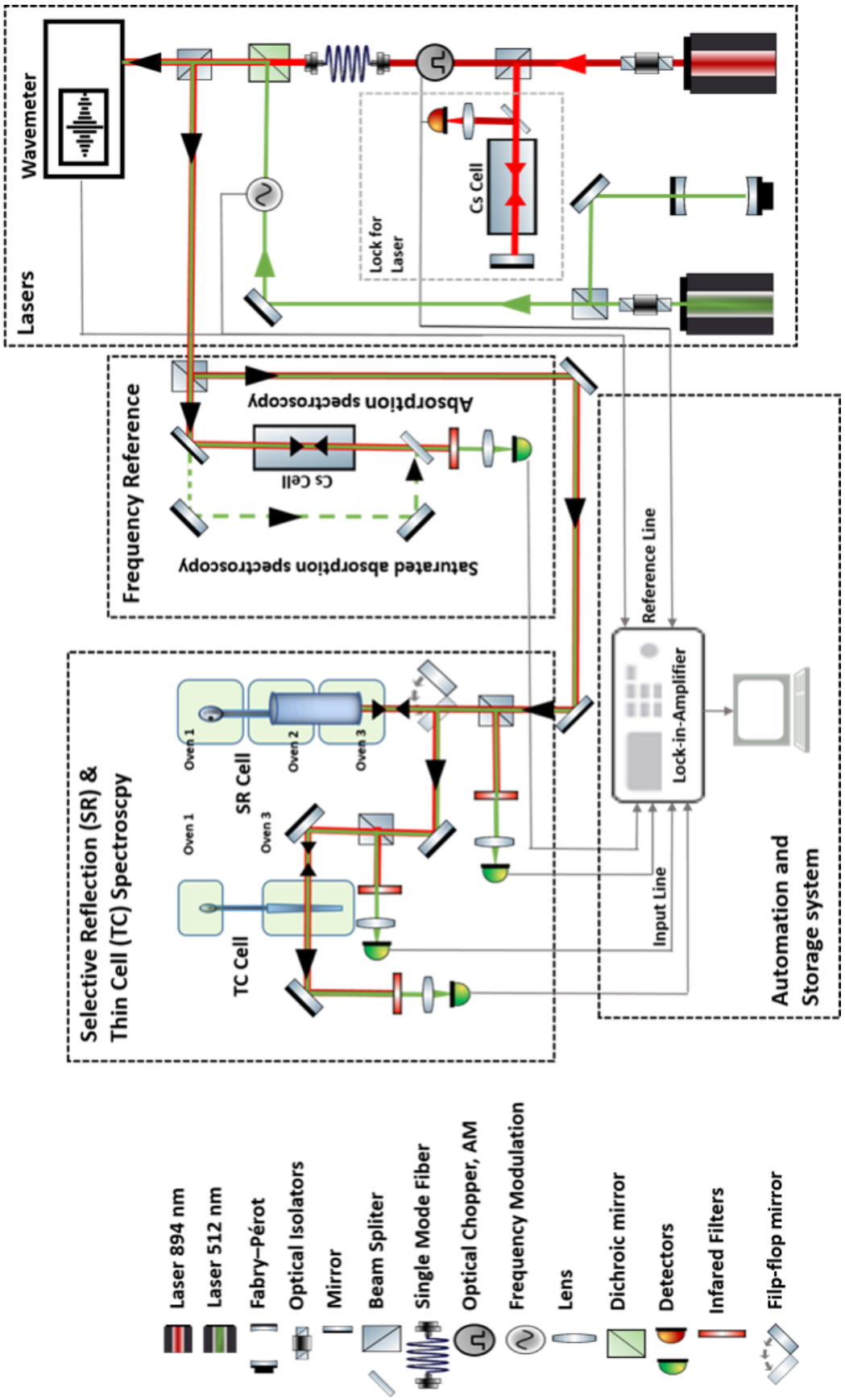

Figure 4.2: A schematic of the experimental setup highlighting some of the key components.

4.2 Experimental setup

Figure 4.2 shows a schematic of the key elements of our experimental setup. The setup can be divided into four primary sections (depicted within a dashed rectangle in Figure 4.2): the laser (consisting of the locks, scanning of the laser, AM, FM), the experiment in volume (step-wise absorption spectroscopy), the experiment close to surface (Selective refection or Thin-cell spectroscopy) and the data acquisition.

We apply amplitude modulation (AM) to the pump laser (indicated by the red line) and frequency modulation (FM) (only for selective reflection experiment) to the probe laser (indicated by the green line). Our main experiment consists of selective reflection (SR) or thin cell (TC) spectroscopy allowing us to probe Rydberg atoms close to a surface and measure CP interactions. Using flip-flop mirrors (Figure 4.2), we channel the lasers to either of these setups (SR or TC). In both cases, we ensure that the incident angle is close to normal with the interacting surfaces. For SR spectroscopy, we perform our measurements on the beam reflected from the atomic vapour-surface interface. For TC spectroscopy, we measure simultaneously the transmitted beam through the thin cell and the reflected beam from the atom vapour-surface interface. The spectroscopic signal is obtained by phase-sensitive detection using lock-in amplifiers. An auxiliary step-wise absorption or saturated absorption spectroscopy experiment is performed in a macroscopic vapour cell to obtain a frequency reference in the volume (not affected by the atom-surface interactions). This provides frequency markers allowing us to calibrate the frequency scale of our laser scans.

4.2.1 Lasers

4.2.1.1 Pump laser

To attain a high population of $6P_{1/2}$ atoms, we adopt a pump and re-pump configuration employing two 894 nm lasers detuned by 9.19 GHz (separation between the hyperfine

components of the ground state $F = 4$ and $F = 3$). One of the lasers is a DBR laser (pump laser 1) with an output power of 50 mW and a linewidth of about 1-2 MHz (as measured in [50]) while the other (pump laser 2) is an extended cavity laser from TOPTICA DL 100 with an output power of 15 mW (linewidth of $\approx$ 200 kHz at time scales of $\approx 5\mu$s as mentioned by the manufacturer). The two pump lasers are orthogonally polarized and overlapped on a polarising beam splitter. Figure 4.3 shows the typical pumping configuration. The lasers are tuned to the same hyperfine component of the excited ($6P_{1/2}$) level, starting from different components of the ground state ($6S_{1/2}$) (most commonly, pump laser 1 is tuned on the $6S_{1/2}(F = 3) \rightarrow 6P_{1/2}(F = 4)$ and pump laser 2 on the $6S_{1/2}(F = 4) \rightarrow 6P_{1/2}(F = 4)$ transition).

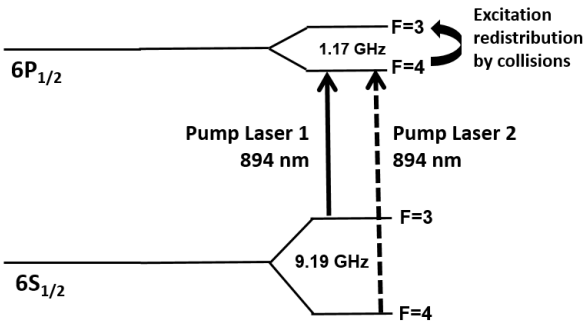

Figure 4.3: Pump and re-pump configuration on $6S_{1/2} \rightarrow 6P_{1/2}$ transition.

- Frequency Stabilization

Frequency drifts of the pump laser from the D_1 resonance could result in loss of population in the $6P_{1/2}$ state and consequently, this could result in a decline in the signal amplitude probing $6P_{1/2} \rightarrow nS_{1/2}, nD_{3/2}$ transition. To avoid this, we stabilize the pump frequency by locking both pump lasers (1 and 2) on a Doppler-free $6S_{1/2} \rightarrow 6P_{1/2}$ saturated absorption signal obtained in two small auxiliary setups.

- Amplitude Modulation

An optical chopper manufactured by Thorlabs was employed to introduce amplitude modulation at 4.7 kHz on both of the pump lasers. The two (aligned) pump lasers are focused on the plane of the chopper to impose the same amplitude modulation for both lasers. The selection of this modulation frequency was based on measuring the probe laser

noise (standard deviation) at different frequencies, as depicted in figure 4.4. Notably, we observed a fast reduction in noise levels when increasing the modulation frequency from 1 kHz to 5 kHz. However, a further increase in the modulation frequency didn't significantly reduce the noise level. For frequencies higher than 4 - 5 kHz the noise (standard deviation) is proportional to the square root of the incident optical power of the probe laser. The optical chopper can modulate the beam with a maximum frequency of 8 kHz but, at such frequencies, it induces an important mechanical vibration of the optical table exacerbating the noise of the system. We therefore used an AM frequency of 4.7 kHz.

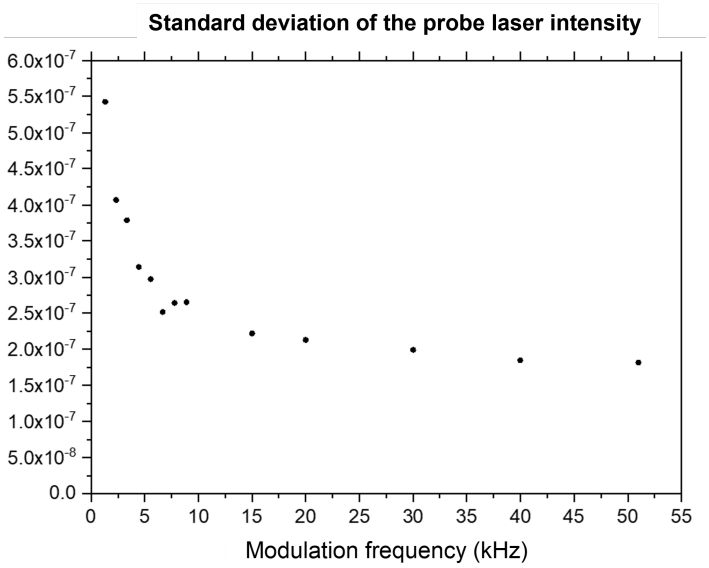

Figure 4.4: Standard deviation of the probe laser intensity at different frequencies. The input power is about 10 mW.

- Spatial filtering

To obtain a uniform beam profile and a better overlap of both pump beams, we inject them through a polarization-maintaining single-mode fibre. This allows us to control the pump beam size and obtain a homogeneous pumping over the entire area of the probe beam (about 4 mm diameter).

4.2.1.2 Probe laser

We have used an extended cavity diode laser from TOPTICA as the probe laser having a wavelength range of 507-514 nm and an output power of 25 mW at 512 nm. The laser

linewidth, as provided by the manufacturer is ≈ 200 KHz for timescales shorter than 5 μs. However, it is important to note that we were unable to obtain spectroscopic signals with a frequency resolution better than ≈ 15 MHz at time scales around 1s (relevant for our experiment).

Figure 4.5 shows the frequency drift of the free-running probe laser as a function of time when positioning the laser frequency on the slope of the absorption line, which acts as a frequency discriminator. The amplitude noise is insignificant in this measurement, as verified by tuning the laser frequency away from the atomic resonance.

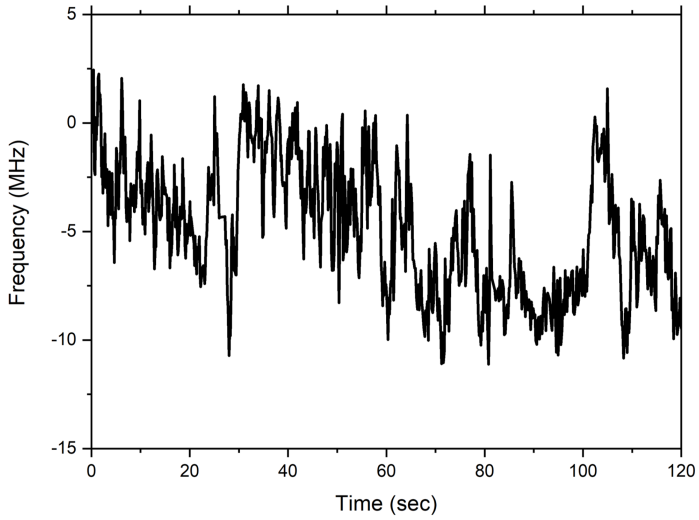

Figure 4.5: Frequency deviation of free-running probe laser as a function of integration time (in sec).

- Scanning of the laser

The probe laser frequency scan is performed by applying a voltage on the piezoelectric actuator of the grating. A feed-forward technique (simultaneous scan of the laser current) is also applied to extend the single mode-hop-free scanning range of the laser to about 20 GHz. The Stanford Research lock-in amplifiers used in our experiment are equipped with low-noise voltage sources. We use this source to perform the probe laser scan which is controlled by a custom-built Labwindows program.

- Frequency modulation (FM)

For the selective reflection experiment, a frequency modulation (FM) is also applied to

the probe laser. This is achieved by adding an external voltage (generated by a function generator) on the piezoelectric element of the grating. Typically the peak-to-peak modulation depth is 56 MHz (peak to peak) and the modulation frequency is 233 Hz.

- Fabry–Pérot interferometer and Wavemeter

The probe laser frequency scan is always monitored with a Thorlabs Fabry–Pérot interferometer having a free spectral range of 1.5 GHz and a resolution of 7.5 MHz (finesse of about 200). This allows us to monitor the single-mode scan of the probe laser. Additionally, we have also installed a Burleigh wavemeter (accuracy of ± 0.0002 nm at 1000 nm) to monitor the frequency of the probe laser.

4.2.2 A brief discussion of the cells

4.2.2.1 Selective reflection (SR) Cell

We performed SR spectroscopy on a Caesium vapour cell manufactured in Armenia by D. Sarkisyan's group and had been previously employed to investigate the Casimir-Polder (CP) interaction of Cs($7D_{3/2}$) [22] and Cs($7P_{1/2}$) states [50] in the presence of thermally excited surface modes. A photograph of the cell (taken from [50]) is displayed in figure 4.6.

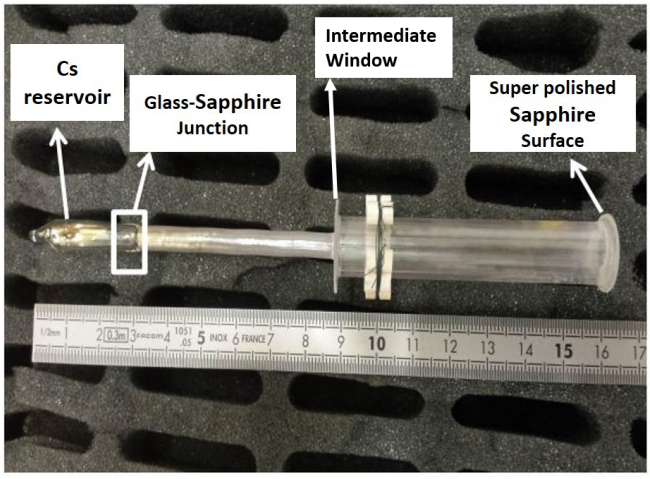

Figure 4.6: A photo of the SR cell.

The main body of the cell is an 8 cm long alumina cylinder onto which two sapphire windows are glued. The first window (where selective reflection measurements are per-

formed) is a super-polished sapphire window (diameter of about 2 cm) with a roughness of 0.3 nm as measured by atomic force microscopy. This window is glued on the main body of the cell using a high-temperature mineral glue able to withstand temperatures up to 900° C. The second window (intermediate window) is also made of sapphire with a lower surface quality. The 8 cm long sidearm parallel to the cell's main body is glued to a small hole drilled into the intermediate window. The cell is put inside three independent ovens which are screwed on a platform that is securely placed on our optical table. These ovens precisely regulate the temperature of the cell.

- The heating system

The heating system of the cell consists of three independent ovens (figure 4.7): oven (1) heats the main sapphire window, oven (3) controls the heating of the Cs reservoir and oven (2) heats the middle part of the cell and maintains the thermal gradient between the surface and the reservoir (figure 4.7). Oven (1) is sealed with a glass window that allows optical access while thermally insulating the oven. The cell temperature is measured using three thermocouples: one is touching the front face of the sapphire window, another is in contact with the Caesium reservoir and a third one is placed in contact with the intermediate window. The three ovens are identical having tungsten filaments as heating elements. The filaments are consistently looped in forward and backward directions to minimize the induced magnetic field on passing current through them.

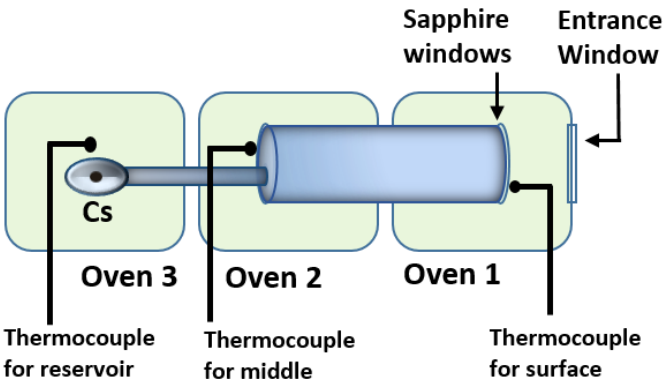

Figure 4.7: Selective reflection cell with the ovens and the thermocouples.

- Control for heating system

The cell temperature is controlled using a "Labwindows" program which regulates the power supplied to each of the three independent ovens (surface, middle, and reservoir). The program ensures that all parts of the cell quickly reach the desired temperature and maintains a difference of at least 50°C between the reservoir (oven 3) and the main body of the cell (ovens 1 and 2) to avoid Caesium condensation on the main body of the cell. To prevent thermal stress, the temperature rise and fall are not allowed to exceed 15° C/min. The maximum allowed temperatures defined by the manufacturer for oven (1), oven (2), and oven (3) are 900°C, 350°C, and 200°C, respectively. The temperature is measured every 5 seconds. The temperature stabilization accuracy is very good, within fluctuations of only about 2°C, which can result in a 5% variation in the vapour pressure. If a thermocouple disconnects from the control system, the program shuts down all the ovens. In the case of a blackout, Backup batteries are installed so that the program has enough time to bring the cell to room temperature.

We assume that the vapour pressure close to the surface remains approximately the same as that of the reservoir. The Caesium (Cs) pressure in the cell can be obtained by employing the following equation [70]:

$$P = 10^{(7.046 - 3830 T_r^{-1})} \tag{4.1}$$

where P is the vapour pressure (Torr) and T_r is the reservoir temperature (K).
Subsequently one can also obtain the relative atomic density as:

$$n = (P/K_B T_s)$$

where K_B is the Boltzmann constant and T_s is the surface temperature (K).
Figure 4.8 shows Caesium density and pressure as a function of Temperature (we assume that $T_s = T_r = T$).

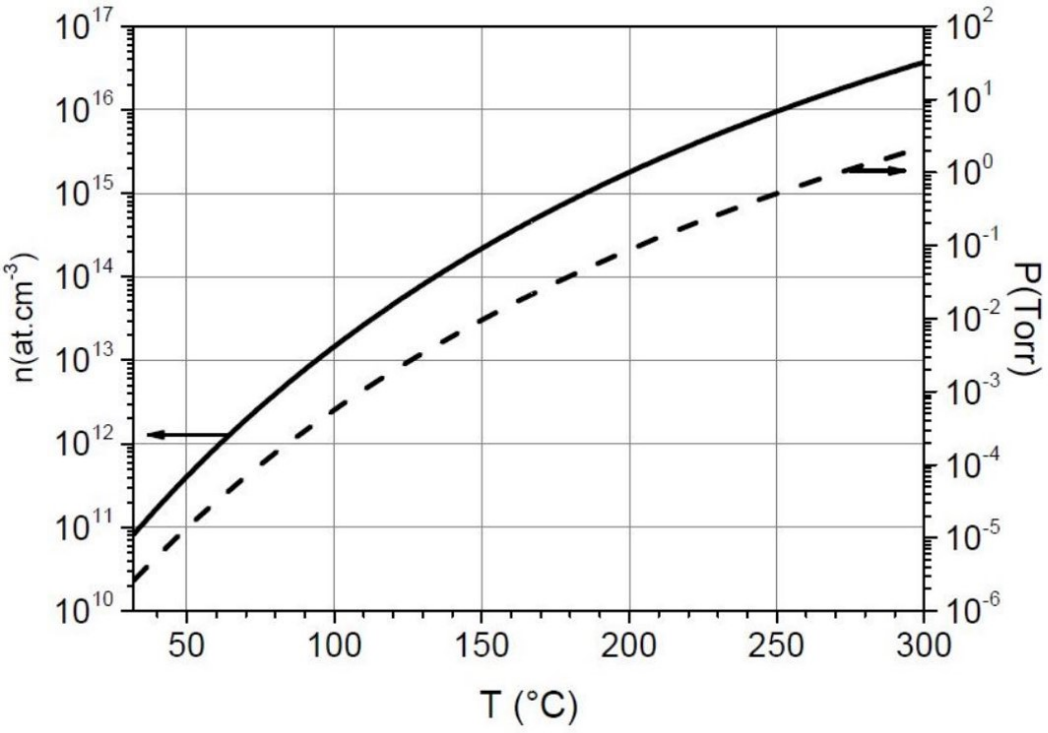

Figure 4.8: Ground state Caesium ($6S_{1/2}$) vapour pressure (in Torr) and atomic density (in atom cm^{-3}) as a function of temperature T (in °C) (where we assume $T_s = T_r = T$).

4.2.2.2 Thin cell (TC)

The thin-cell (TC) used in our TC experiment is also manufactured in Armenia by D. Sarkisyan's group and was previously used to measure the CP interaction of the Caesium $6D_{3/2}$ state at nanometric atom-surface separations (130 - 40 nm) [23]. A detailed study of this cell (like mapping of the cell thickness) has already been conducted within our research group [52]. The cell is ovoid-shaped with YAG windows of $\approx$ 20 mm in diameter and 2.5 mm in thickness (figure 4.9, taken from [52]). An Al_2O_3 ring of $\approx$ 10 - 15 mm diameter acts as a spacer between the two YAG windows which are attached with mineral glue. After pumping the cell, the YAG windows buckle under atmospheric pressure. This creates a thickness gradient inside the cell ranging from $\approx$ 40 nm at the centre, up to $\approx$ 1000 nm towards the edges of the cell. Different thicknesses can be explored by translating the cell along the X-Y plane. Figure 4.9 shows a photograph of the cell (front view, taken from [52]).

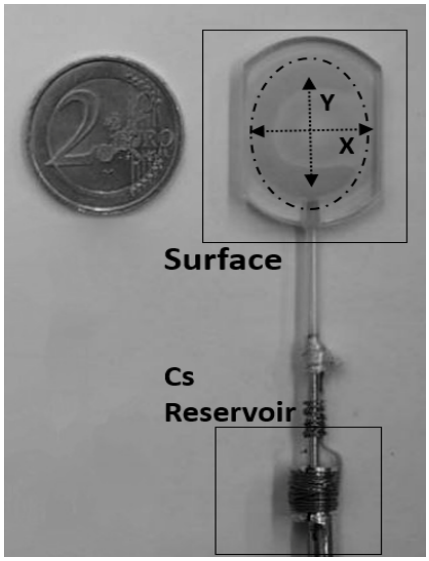

Figure 4.9: A Photo of the thin cell with a coin for reference.

- The heating system

The heating system of the cell consists of two independent ovens (figure 4.10): oven (1) controls the temperature of the YAG surface while oven (2) controls the temperature of the Cs reservoir. Oven (1) is sealed with an AR-coated (894 nm) silica entrance window of 20 mm diameter that allows optical access to the cell. The cell temperature is measured using thermocouples with one touching the front face of the YAG window and another in contact with the Caesium reservoir (figure 4.10). Ovens are enclosed in a ceramic shell inside a black housing which provides thermal insulation. The maximum operating temperature defined by the manufacturer for the oven (1) is about 300°C and for the oven (2) is about 270°C. The ovens are mounted on a transitional platform that can move in X-Y-Z direction allowing us to easily explore different cell thicknesses.

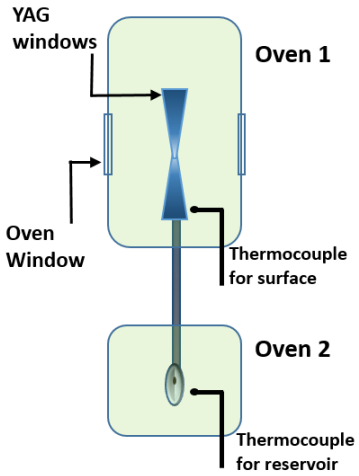

Figure 4.10: Schematic of thin cell (side view) indicating the ovens and thermocouples.

- Thickness measurement

The thickness of the thin cell is measured by Fabry-Pérot interferometry. Figure 4.11 illustrates the path of a laser beam (**1**) passing through the cell at near normal incidence. The thin-cell reflection is indicated as (**3**) (only one reflection beam is observed due to the good parallelism between the two interfaces forming the thin-cell cavity) while the reflection from the first window is indicated as (**2**).

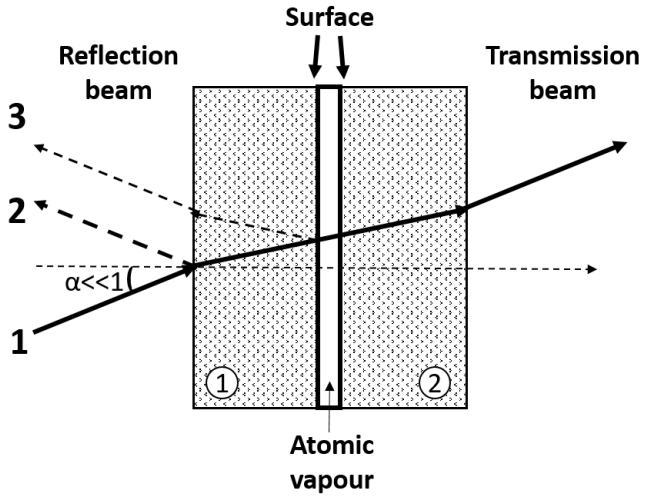

Figure 4.11: Transmission path of a near normal incident beam (1) through the thin cell which acts as a low finesse Fabry–Pérot interferometer. Beams indicated by (2) and (3) are the reflected beams from the first window and the thin cell respectively. $\alpha \ll 1$ is the incident angle which has been deliberately upscaled in the figure for convenience.

Correcting for the losses induced by the first window, the experimentally determined thin cell reflectance ($\mathbf{R}_c$) is given by:

$$\mathbf{R}_C = \frac{\mathbf{P}_3}{\mathbf{P}_1 \mathbf{T}_W^2} \tag{4.2}$$

where $\mathbf{T}_w$=1-($\mathbf{P}_2/\mathbf{P}_1$) is the transmittance of the windows/air interface and $\mathbf{P}_1$, $\mathbf{P}_2$ $\mathbf{P}_3$ is the power of the incident (1) and reflected beams (2,3) respectively.

Using Fabry–Pérot theory, the thin cell reflectance for an incident beam having wavelength λ is given by:

$$\mathbf{R}_C = \frac{\mathbf{F} \sin^2\left(2\pi \mathrm{d} \frac{\cos(\alpha)}{\lambda}\right)}{1 + \mathbf{F} \sin^2\left(2\pi \mathrm{d} \frac{\cos(\alpha)}{\lambda}\right)} \tag{4.3}$$

where d is the thin cell thickness, λ is the wavelength of the incident beam, α is the incident angle and $\mathbf{F} = 4R_W/(1 - R_W^2)$. R_W is the reflectivity of the YAG-air interface,

which is also a function of wavelengths.

Equation 4.3 is a periodical function of cell thickness d (figure 4.12). Therefore, an experimental measurement using a single wavelength does not allow us to uniquely determine the cell thickness [52]. For this purpose, we use 2 or more lasers of different wavelengths for our thickness measurement. In figure 4.12, we show a typical cell thickness measurement using two lasers (894 nm and 512 nm). The two lasers overlap and hit the same point on the cell. By using two different wavelengths, we obtain an overlap between the two reflectances for a particular cell thickness of 477 ± 5 nm (marked as black cross).

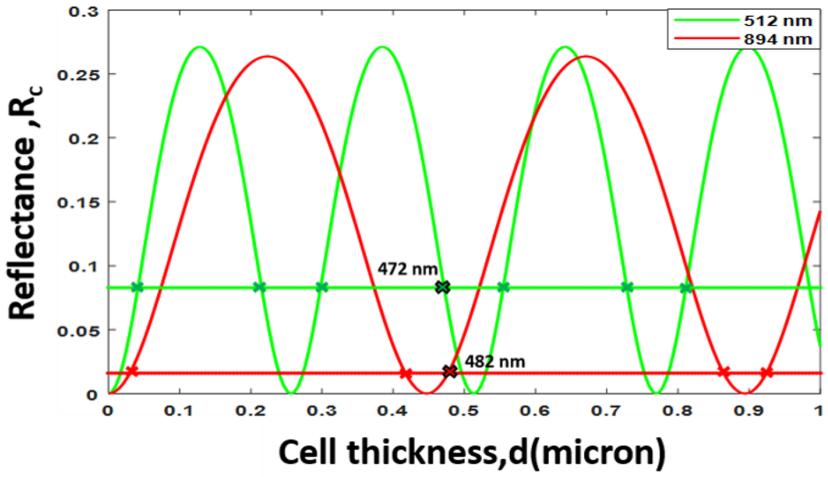

Figure 4.12: Reflectance (R_c) as a function of cell thickness (d) (red line: 894 nm, green line: 512 nm). The straight line shows the value of measured reflectance. By using two different wavelengths, we can pinpoint the cell thickness to be 477 ± 5 nm.

4.2.2.3 The macroscopic cells

- For locking the pump laser

For locking the pump lasers (894 nm) on the slope of D_1 saturated absorption line, we have used a Thorlabs Caesium vapour reference cell, kept at ambient temperature. The cell is made from quartz and has a cylindrical shape with a length of about 80 mm and a diameter of 25 mm with a sidearm of about 100 mm.

- Cells used for frequency reference

To obtain frequency references and calibrate the frequency scale of our probe laser, we perform a two-step absorption spectroscopy on $(6P_{1/2} \rightarrow nS_{1/2}, nD_{3/2})$ line in the microscopic cell [section 4.3]. The cell body is an approximately 1 cm long copper cylinder having sapphire windows on either side and an extended forearm in the middle containing Cs reservoir [71]. The cell is inserted in a system of two metal boxes, one containing the body of the cell and the other containing the Cs reservoir. Each box is independently heated up, hence two independent temperature regions are defined and we ensure overheating of the windows ($T_s \sim 100°C$) relative to the Cs reservoir ($T_r \sim 70°C$). The temperature was measured by two thermocouples, one touching the cell's main body and the other is on contact with the cell reservoir.

4.2.3 Data acquisition unit and automation of the experimental setup

Data acquisition processes are controlled by custom-built Labwindows software. The computer controls a voltage ramp that is applied to the piezoelectric actuator of the laser grating to scan the laser's frequency. For each frequency scan point, the input signals from the photodetectors and the lock-in amplifiers are digitized by a DAQ and recorded in the computer. Next, these signals are treated in a Matlab program that uses the stepwise $(6P_{1/2} \rightarrow nS_{1/2}, nD_{3/2})$ absorption signal to calibrate the frequency scale of each scan. The time difference between two successive frequency point measurements is about 200 ms and the lock-in amplifier time constant is set to 300 ms. A typical scan with a frequency resolution of 3 MHz over a span of 3 GHz takes about 5 minutes. Finally, we average approximately 150 scans to acquire an acceptable signal-to-noise ratio which takes around 10 hours of integration time. During this long integration time, we verify that the experimental conditions remain unchanged by simultaneously checking the frequency stabilization of the pump lasers, the temperature of the cell and the scan of the probe laser.

4.3 Absorption spectroscopy in a volumetric cell

4.3.1 Two-step absorption spectroscopy

Two-step absorption spectra were also obtained by pumping the atoms from $6S_{1/2} \rightarrow 6P_{1/2}$ at 894 nm (pump laser) and subsequently performing absorption spectroscopy on $6P_{1/2} \rightarrow nS_{1/2}, nD_{1/2}$ (n = 15 - 17) line with the 507 - 514 nm laser (probe laser). The pump and probe lasers co-propagate in a 1 cm Caesium vapour cell (spectroscopic measurements are not influenced by the atom-surface interactions). An amplitude modulation (AM) of 1.9 kHz is applied to the pump laser with an optical chopper. Pump and probe laser intensities were kept fixed at 3.5 mW/cm^2 and 2.5 mW/cm^2 respectively and the Cs vapour pressure around $\sim$ 0.1 mTorr. For this discussion, we will consider the $6P_{1/2} \rightarrow 15D_{3/2}$ transition (512 nm) with the pump laser locked on the $6S_{1/2}(F = 3) \rightarrow 6P_{1/2}(F = 4)$ transition. Figure 4.13 shows the normalized two-step $6P_{1/2} \rightarrow 15D_{3/2}$ absorption spectrum (signal amplitude is normalized to the off-resonant transmission probe power).

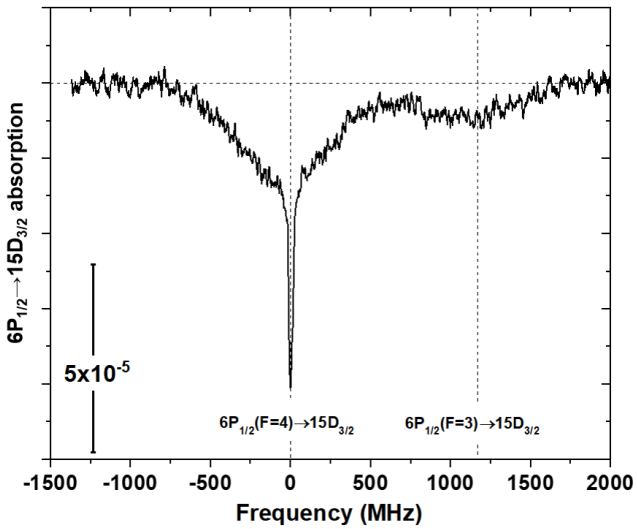

Figure 4.13: Normalized $6P_{1/2} \rightarrow 15D_{3/2}$ absorption spectrum with the pump laser locked on $6S_{1/2}(F = 3) \rightarrow 6P_{1/2}(F = 4)$ transition. Signal amplitude normalized to off-resonant transmission probe powers. Laser intensities: pump $\sim$ 3.5 mW/cm^2, probe $\sim$ 2.5 mW/cm^2. Cs vapor pressure: $\sim$ 0.1 mTorr. Horizontal dashed line: the zero level and vertical dashed lines: $6P_{F=4,3} \rightarrow 15D_{3/2}$ transition in volume.

The sub-Doppler peak over a broad (Doppler broadened) pedestal corresponds to a velocity selection by the infrared pump laser when the probe (green) laser is tuned on the $6P_{1/2}(F = 4) \rightarrow 15D_{3/2}$ resonance. The existence of the broad pedestal is attributed to a redistribution of the atomic excitation to all velocity groups by either collisions or radiation trapping [72][73].

Firstly, we obtained normalized $6P_{1/2} \rightarrow 15D_{3/2}$ absorption spectra by increasing pump intensity from 3.5 mW/cm^2 to 50 mW/cm^2 keeping the vapour pressure at 0.1 mTorr (figure 4.14). Signal amplitudes are normalized to the maximum amplitude of each absorption line. We observe two distinct absorption lines for the two hyperfine components of $6P_{1/2}$ and a significant broadening of the lineshape, suggesting a strong contribution coming from collisions among excited $6P_{1/2}$ state atoms in the excitation redistribution process. It is interesting to notice that the initial velocity selective excitation (sub-Doppler signals separated by exactly 1.167 GHz) can be observed for both hyperfine components of $6P_{1/2}$. This is a new observation and in the following section, we present some preliminary investigations on these sub-Doppler signals.

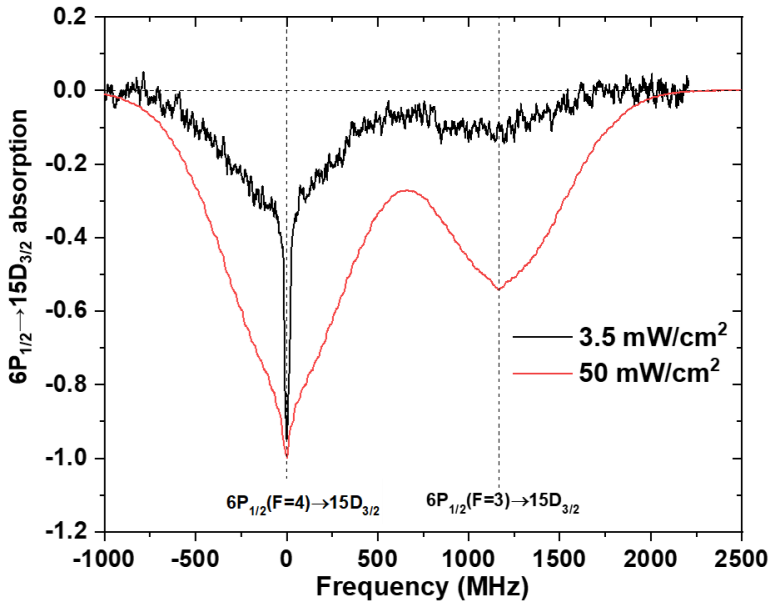

Figure 4.14: Normalized $6P_{1/2} \rightarrow 15D_{3/2}$ absorption spectrum with the pump laser locked on $6S_{1/2}(F = 3) \rightarrow 6P_{1/2}(F = 4)$ transition. Signal amplitudes: normalized to the maximum amplitude of each absorption line. Laser intensities: pump $\sim$ 3.5 mW/cm^2, probe $\sim$ 2.5 mW/cm^2. Cs vapor pressure: $\sim$ 0.1 mTorr. Horizontal dashed line: the zero level and vertical dashed lines: $6P_{F=4,3} \rightarrow 15D_{3/2}$ transition in volume.

Subsequently, $6P_{1/2} \rightarrow 15D_{3/2}$ absorption spectra were also obtained for different vapour densities with high pump intensities ~ 50 mW/cm^2 (figure 4.15). With increasing vapour density the redistribution of the excitation becomes more efficient for both hyperfine components for a given pump intensity, suggesting an increase in the collision rate between the ground state Cs($6S_{1/2}$) atoms and excited Cs ($6P_{1/2}$) state. Like the previous case, we can also observe a significant broadening of the lineshape. However, despite the broadening, a sub-Doppler signal due to the initial velocity selective excitation is still distinguishable over the broad lineshape.

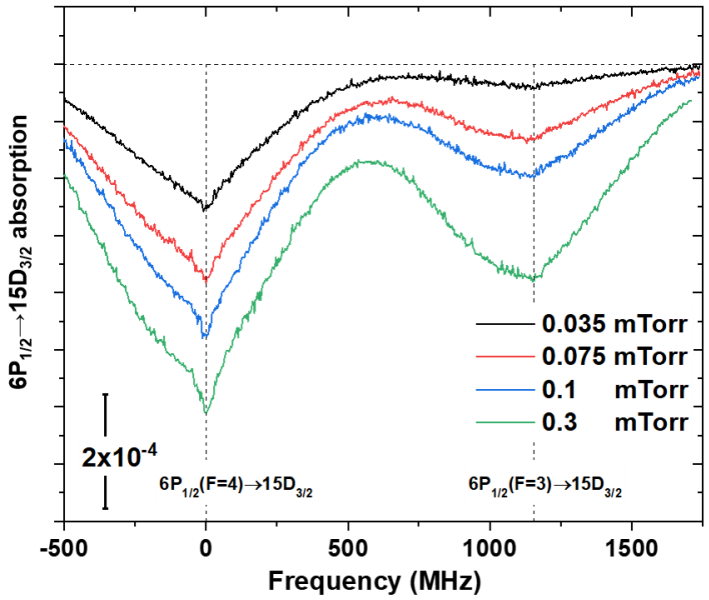

Figure 4.15: Normalized $6P_{1/2} \rightarrow 15D_{3/2}$ absorption spectra with pump intensities of ~ 50 mW/cm^2 for different ground state ($6S_{1/2}$) vapour pressure. Signal amplitudes are normalized to off-resonant transmission probe powers. Probe laser intensities ~ 2.5 mW/cm^2. A horizontal dashed line indicates the zero level and two vertical dashed lines mark $6P_{F=4,3} \rightarrow 15D_{3/2}$ transition in volume.

4.3.1.1 Sub-Doppler peaks of $6P_{1/2} \rightarrow 15D_{1/2}$ absorption spectra

To investigate the effects of pump laser frequency on step-wise $6P_{1/2} \rightarrow 15D_{3/2}$ absorption, the frequency of the infrared pump laser was detuned slightly from the D_1 resonance (detuned by 150 MHz about half of the Doppler width). Absorption spectra were obtained with the vapour pressure fixed at approximately 0.1 mTorr with pump and probe laser intensities set at 50 mW/cm^2 and 2.5 mW/cm^2, respectively. Figure 4.16 shows normalized $6P_{1/2} \rightarrow 15D_{3/2}$ absorption spectra (signal amplitudes are normalized to the amplitude

of each absorption line) as a function of frequency detuning of pump laser: (a) Pump frequency, $\omega_{IR} = \omega$ (on $6S_{1/2}(F = 3) \rightarrow 6P_{1/2}(F = 4)$ resonance) (b) Pump frequency, $\omega_{IR} = \omega - \delta$ (c) Pump frequency, $\omega_{IR} = \omega + \delta$.

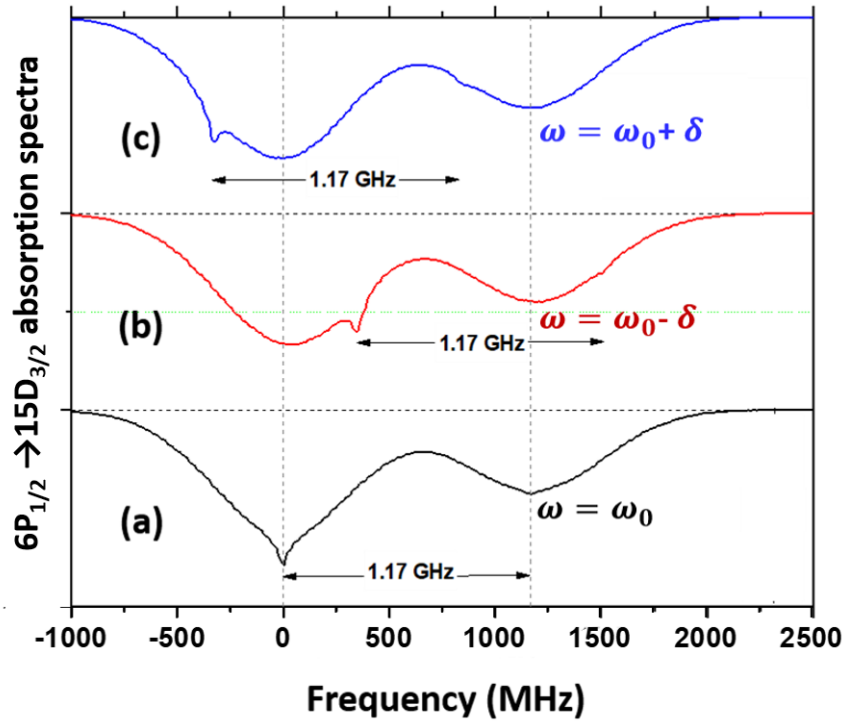

Figure 4.16: Normalized $6P_{1/2} \rightarrow 15D_{3/2}$ absorption spectra for Pump frequency : (a) pump frequency on resonance, $\omega_{IR} = \omega_0$ (b) pump frequency, $\omega_{IR} = \omega_0 - \delta$ (c) pump frequency, $\omega_{IR} = \omega_0 + \delta$. Signal amplitudes are normalized to the maximum amplitude of each absorption line. The pump frequency detuning is $\delta \approx 150$ MHz leading to a ≈ 260 MHz shift of the sub-Doppler peaks in the probe absorption spectrum. A horizontal dashed line indicates the zero level and two vertical dashed lines mark $6P_{F=4,3} \rightarrow 15D_{3/2}$ transition in volume.

For these three cases, it is evident that the sub-Doppler signals for both hyperfine components follow the detuning of the pump laser. The underlying mechanism behind this phenomenon is not yet fully understood and warrants further investigation. Nevertheless, we present an intuitive hypothesis for this observed behaviour.

If we consider the case of figure 4.17 where the pump laser (894 nm) is locked on the $6S_{1/2}(F = 4) \rightarrow 6P_{1/2}(F = 4)$. The pump interacts with v_z atoms exciting them to the $6P_{1/2}(F = 4)$ level. Due to spontaneous emission, some slow atoms (v_z) will be optically pumped to the $6S_{1/2}(F = 3)$ state. This process burns a hole on the $6S_{1/2}(F = 4)$ population while adding a peak on the $6S_{1/2}(F = 3)$ population at v_z. At low densities (without

any active redistribution mechanisms), the excited state population consists entirely of v_z atoms at the $6P_{1/2}(F = 4)$ state, whereas the $6P_{1/2}(F = 3)$ is not populated.
At higher densities, the excitation is also redistributed to the $6P_{1/2}(F = 3)$ level mostly by resonance exchange collisions of the following type [72]:

$$Cs(6P, u_1) + Cs(6S, u_2) \rightarrow Cs(6s, v_1) + Cs(6P, v_2) \tag{4.4}$$

where u_1, u_2, v_1, v_2 represent different velocity classes. In the above collisional mechanism, a velocity-selected excited atom is replaced by a non-velocity selected one with a collisional cross-section that depends on the transition dipole matrix element. The effects of resonance transfer collisions are thus dominant for $Cs(6P_{1/2})$ atoms, while their effect is shown to be considerably diminished for highly excited states (see reference [72] for a study on $Cs(7P)$ collisions). Radiation trapping has also been considered as an important redistribution mechanism within different velocity classes of the same hyperfine component. However, radiation trapping is probably less efficient for redistributing the excitation between the two hyperfine components of the excited state whose frequency separation (1.1 GHz) is much larger than the Doppler width (FWHM about 400 MHz).

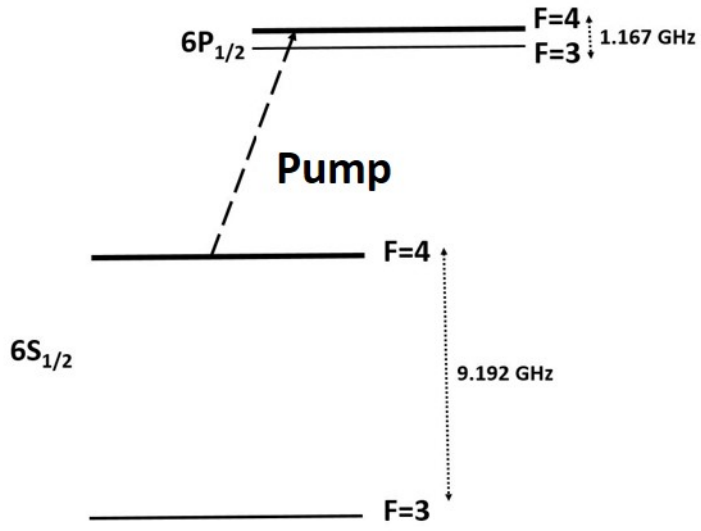

Figure 4.17: An example of $6S_{1/2} \rightarrow 6P_{1/2}$ pumping configuration.

Having established that the population on the excited $6P_{1/2}(F = 3)$ originates from the resonant exchange with ground state atoms the following question arises: Are atoms

mostly transferred from the $6S_{1/2}(F = 4)$ state (whose velocity dependence has a dip at v_z) or from the $6S_{1/2}(F = 3)$ state (whose velocity dependence has a peak at v_z)? If our previous hypotheses (about redistribution mechanism) are correct, this would suggest that the $6S_{1/2}(F = 4) \rightarrow 6P_{1/2}(F = 3)$ should be more favourable due to its higher transition dipole moment element (see Table 4.2). Therefore, the $6P_{1/2}(F = 3)$ population should also be expected to present a small dip at v_z.

Relative Hyperfine Transition Strength Factors S_{FF}			
Transition	Strength	Transition	Strength
$S_{44'}$	5/12	$S_{34'}$	3/4
$S_{43'}$	7/12	$S_{33'}$	1/4

Table 4.2: Relative $6S_{1/2} \rightarrow 6p_{1/2}$ hyperfine transition strength factor S_{FF}.

To test the above hypothesis, we measure the green laser absorption on the $Cs(6P_{1/2}) \rightarrow Cs(15D_{1/2})$ channel for all 4 possible pumping configurations (figure 4.18). We note that in our case, the weak non-saturating green laser simply probes the velocity-dependent population of the Caesium excited state without affecting it. In Figure 4.18 we can see that when the pump laser addresses the same hyperfine component for both ground $Cs(6S_{1/2})$ and excited $Cs(6P_{1/2})$ states i.e. either $6S_{1/2}(F = 4) \rightarrow 6P_{1/2}(F = 4)$ or $6S_{1/2}(F = 3) \rightarrow 6P_{1/2}(F = 3)$, the population of the excited state hyperfine component that is not directly pumped presents a dip at v_z. In the opposite case when the pump laser addresses the different hyperfine components i.e. either $6S_{1/2}(F = 4) \rightarrow 6P_{1/2}(F = 3)$ or $6S_{1/2}(F = 3) \rightarrow 6P_{1/2}(F = 4)$, the population of the excited hyperfine component that is not directly pumped presents a peak at v_z. This experimental result is qualitatively consistent with our tentative explanation for the origin of the sub-Doppler peaks on the $Cs(6P_{1/2}) \rightarrow Cs(15D_{1/2})$ absorption spectrum.

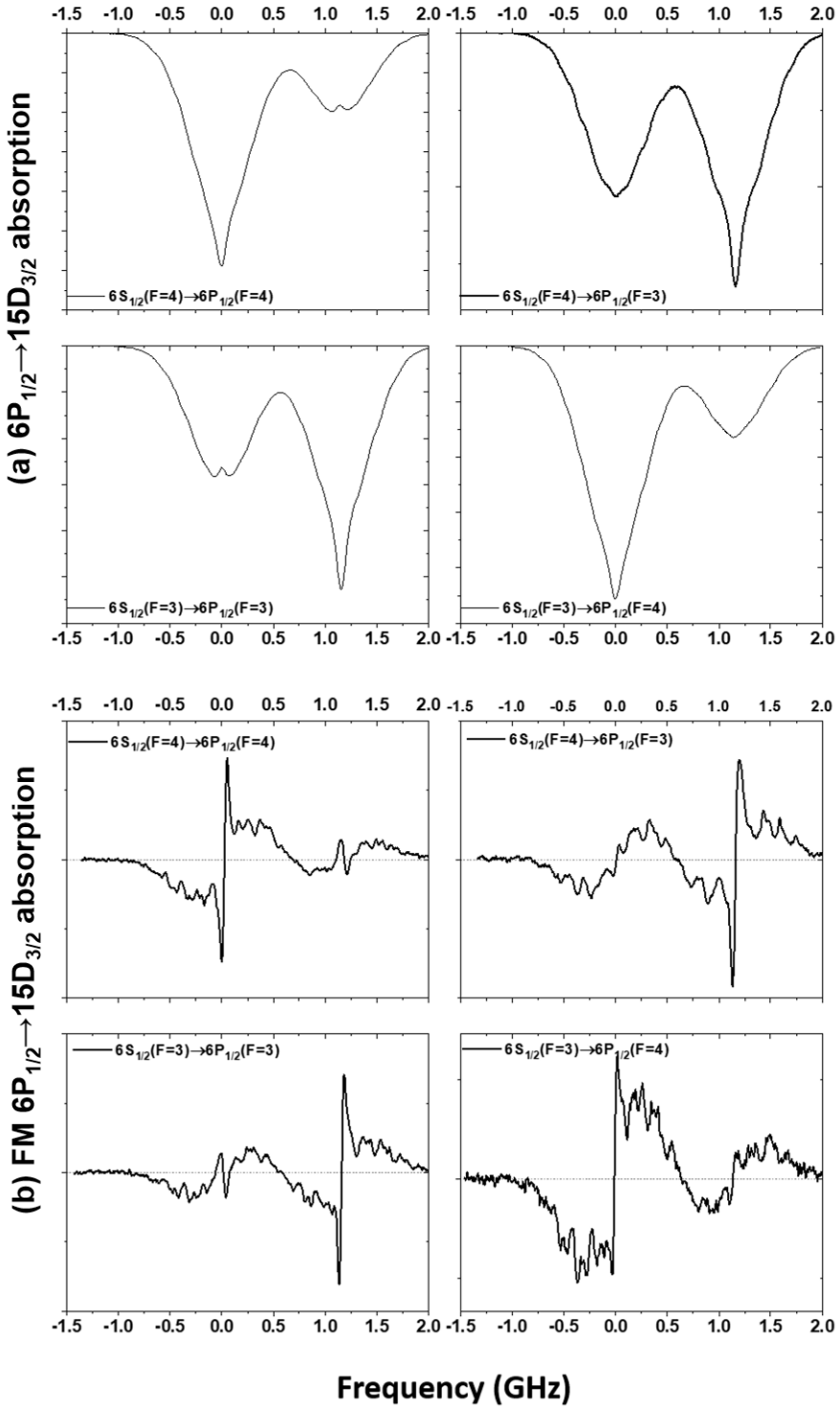

Figure 4.18: (a) Normalized $6P_{1/2} \rightarrow 15D_{3/2}$ absorption spectra (b) normalized FM $6P_{1/2} \rightarrow 15D_{3/2}$ absorption spectra for all 4 possible pumping configurations on the $6S_{1/2} \rightarrow 6P_{1/2}$ line. The signal amplitude is normalized to the maximum amplitude. Pump laser: on resonance (addressing $v_z = 0$ atoms) with AM modulated at 1.7 kHz. Probe laser: FM modulated with 23 MHz peak-to-peak excursion at 233 kHz. The directly pumped hyperfine component always presents a peak at $v_z = 0$ due to the velocity selection of the pump. The hyperfine component that is not directly pumped presents either a peak (for $6S_{1/2}(F = 4) \rightarrow 6P_{1/2}(F = 4)$ or $6S_{1/2}(F = 3) \rightarrow 6P_{1/2}(F = 3)$ pumping) or a dip (for $6S_{1/2}(F = 4) \rightarrow 6P_{1/2}(F = 3)$ or $6S_{1/2}(F = 3) \rightarrow 6P_{1/2}(F = 4)$ pumping). Horizontal dashed line indicates the zero level.

Nevertheless, this unexpected sub-Doppler (high-resolution) spectroscopic signal allows us to calibrate the frequency scale of the green (probe) laser without resorting to a more complicated and optical power-demanding saturated absorption technique.

4.3.2 Saturated absorption Spectroscopy

To estimate the pressure broadening for these highly excited states, we have also performed step-wise saturated absorption $6P_{1/2} \rightarrow 15D_{3/2}$ line in a 100-micron Cs vapour cell. The IR pump (894 nm) $\sim$ 3 W/cm^2 and green probe (512 nm) $\sim$ 0.06 W/cm^2 co-propagate while the green pump (512 nm) $\sim$ 2 W/cm^2 is in counter-propagating configuration (Figure 4.19). The laser beams were tightly focused and overlapped at the centre of the cell. The amplitude of the IR pump and green pump were modulated at 233 Hz and 1.7 KHz respectively with two optical choppers and the $6P_{1/2} \rightarrow 15D_{3/2}$ saturated absorption was obtained by performing cascaded lock-in detection. Figure 4.19 shows the schematic of the experimental setup.

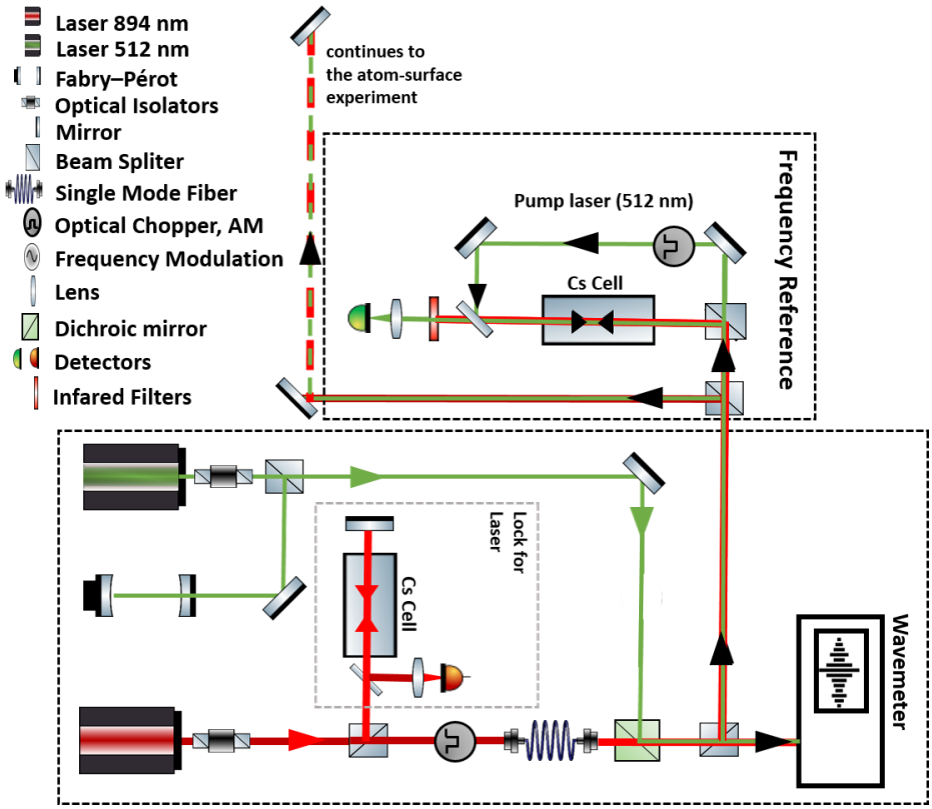

Figure 4.19: Schematic of the experimental setup for the $6P_{1/2} \rightarrow nS_{1/2}, nD_{3/2}$ saturated absorption spectroscopy.

Figure 4.20 shows the normalized $6P_{1/2} \rightarrow 15D_{3/2}$ experimental saturated absorption spectrum (for pump laser tuned on $6S_{1/2}(F = 4) \rightarrow 6P_{1/2}(F = 3)$ transition) (black line) with Lorentzian fitted line (red line) having linewidth $\sim$ 26 MHz for a Cs vapour pressure 7 mTorr. The amplitude of the saturated absorption spectrum is normalized to the non-resonant transmission probe power. To estimate the pressure broadening, we carried out linewidth measurements for different vapour pressures.

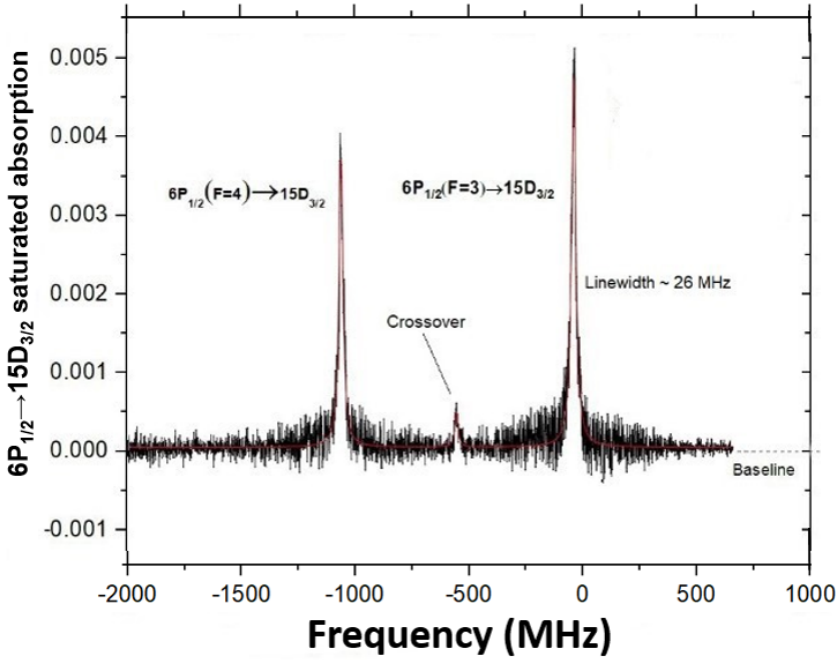

Figure 4.20: Normalized $6P_{1/2} \rightarrow 15D_{3/2}$ saturated absorption spectrum (black line) with Lorentzian fitted with linewidth $\sim$ 26 MHz (red line). Signal amplitude is normalized to the non-resonant transmission probe power. Pump laser intensities: IR $\sim$ 3 W/cm^2 and green $\sim$ 2 W/cm^2, Green Probe intensity : 0.06 mW/cm^2. Cs vapor pressure $\sim$ 7 mTorr.

Figure 4.21 shows the linear evolution of homogeneous linewidth with Caesium vapour pressure. The minimum resolvable linewidth is approximately 15 $\pm$ 2 MHz at 0.3 mTorr. Lowering the vapour pressure even more resulted in a very weak signal with a very high error bar. The pressure broadening (collisional broadening) for $6P_{1/2} \rightarrow 15D_{3/2}$ is estimated to be $\sim$ 2 GHz/Torr. Due to the step-wise excitation, we were heavily limited by the broadening of the D_1 line, which is around 1 GHz/Torr [70]. Previously, similar results were obtained on $6P_{1/2} \rightarrow 6D_{3/2}$ line in the same cell [38] where $6P_{1/2} \rightarrow 6D_{3/2}$ saturated absorption linewidth was also limited to $\sim$ 15 MHz with the pressure broadening of 1.6

GHz/Torr justifying our measurements.

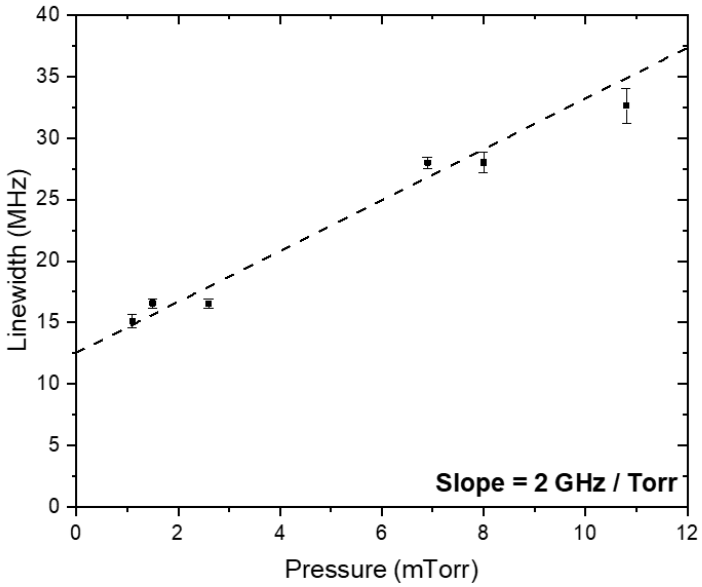

Figure 4.21: Homogeneous linewidth measurement of $6P_{1/2} \rightarrow 15D_{3/2}$ saturated absorption spectra as a function of Caesium vapour pressure. The linear fit (dotted line) to the measurement values shows a linear growth of the homogeneous linewidth with Caesium vapour pressure and presents a slop of 2 GHz/Torr.

Chapter 5

Experimental results of Casimir Polder interaction on $nS_{1/2}$ and $nD_{3/2}$ (where n = 15, 16, 17) using selective reflection spectroscopy

---

In this chapter, we present the analysis of $6P_{1/2} \rightarrow nS_{1/2}$ and $6P_{1/2} \rightarrow nD_{3/2}$ frequency-modulated selective reflection (FMSR) spectra (where n = 15 - 17). Due to the weak probability of the above transitions achieving a good signal-to-noise ratio for our recordings presents an important challenge. In section 5.1 we briefly discuss, the procedure for averaging multiple scans that allow us to obtain reliable FMSR spectra. In section 5.2, we discuss the fitting process of theoretical lineshapes to the experimental signal to extract the atom-surface coefficient C_3 and the homogeneous broadening γ. The process is then implemented to measure the atom-surface interaction of the probed ($16S_{1/2}$, $17S_{1/2}$), and ($15D_{3/2}$, $16D_{3/2}$, $17D_{3/2}$) states in sections 5.2 and 5.3 respectively.

5.1 Recording the FMSR spectra

In figure 5.1, we show a single normalized $6P_{1/2} \rightarrow 16S_{1/2}$ FMSR spectrum (black line) obtained in experimentally optimal conditions. The signal amplitudes are normalized to the off-resonant reflected powers. Caesium vapour pressure is kept moderately high ($\sim$ 25 mTorr) with a maximum available probe and pump laser intensity (Laser intensities: pump $\sim$ 35 mW/cm^2 and probe 100 mW/cm^2). The figure also shows FM of the velocity selective $6P_{1/2} \rightarrow 16S_{1/2}$ absorption spectral (grey line) as a frequency reference in the volume.

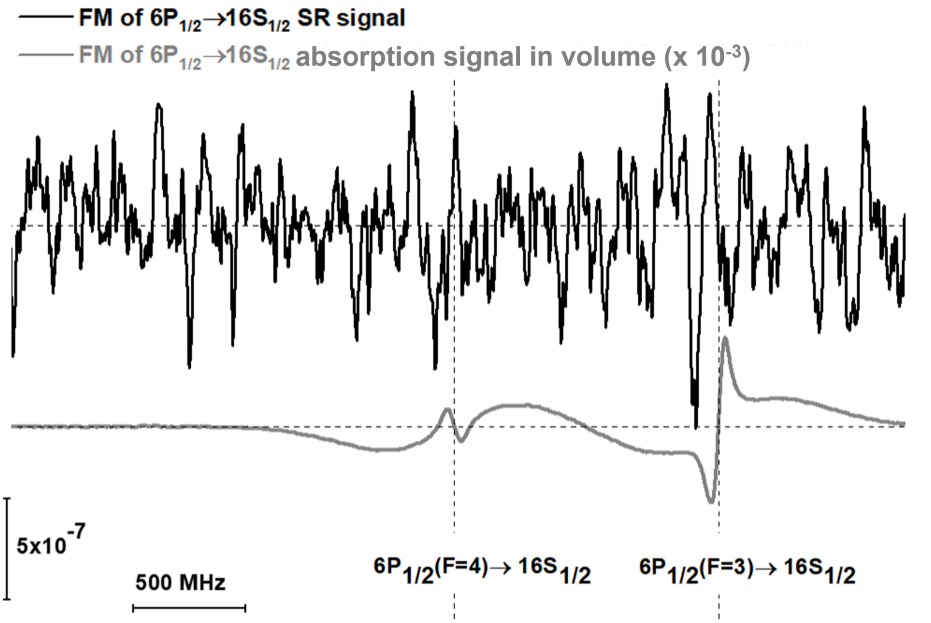

Figure 5.1: Normalized FMSR spectrum (black line) and velocity-selective absorption spectrum (grey line) for $6P_{1/2} \rightarrow 16S_{1/2}$ transition at vapour pressures of $\sim$ 25 mTorr and $\sim$ 0.075 mTorr respectively. Signal amplitudes are normalized to off-resonant reflected probe powers. Laser intensities: pump $\sim$ 35 mW/cm^2, probe $\sim$ 100 mW/cm^2. Scan: time constant 300 ms. Horizontal dashed line: zero references for each spectrum. Vertical dashed lines: frequency reference from $6P_{1/2} \rightarrow 16S_{1/2}$ absorption in volume.

The scan presented in figure 5.1 is extremely noisy (the FMSR lineshapes are barely observable) making it impossible to obtain any reliable data exploitation. In principle, increasing the vapour density or the pump power can increase the $6P_{1/2}$ population and consequently lead to a larger signal amplitude. But for the scans presented in Figure 5.1, the Caesium (Cs) reservoir was close to the maximum operation temperature (200°C)

with a maximum available pump power (as aforementioned). A practical solution for enhancing the signal-to-noise ratio is to average multiple spectra by performing rapid successive laser scans. As the probe laser frequency drift is around 100 MHz/hr and the pump laser frequency drift is around a few tens of MHz/hr, the averaging process requires good calibration of the scan frequency scale. We locked the 894 nm pump laser at $6S_{1/2}(F = 4) \rightarrow 6P_{1/2}(F = 3)$ transition and multiple successive frequency scans of 512 nm probe laser were obtained at every $\sim$ 5 min over a frequency span of $\sim$ 3 GHz. The drift of the probe laser frequency was corrected using the two frequency markers of the absorption curve (dashed lines). Usually, averaging of about 150-170 spectra was needed to obtain an acceptable signal-to-noise ratio. Figure 5.2 shows the comparison between the average of 170 spectra and a single FMSR spectrum.

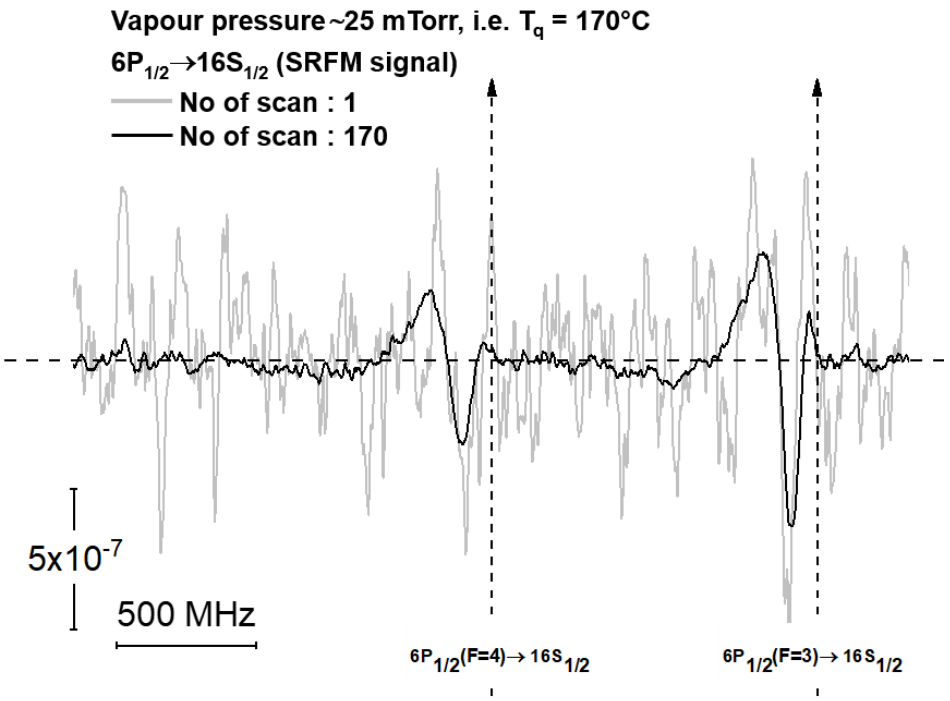

Figure 5.2: Comparison between a single $6P_{1/2} \rightarrow 16S_{1/2}$ FMSR spectrum (grey line) and FMSR spectra after averaging 170 scans (black line).Cs vapour pressure: $\sim$ 25 mTorr. Signal amplitudes are normalized to off-resonant reflected probe powers. Horizontal dashed line: zero references for each spectrum. Vertical dashed lines: frequency reference from $6P_{1/2} \rightarrow 16S_{1/2}$ absorption in volume.

After averaging about 170 spectra, we obtain an FMSR signal with an acceptable signal-to-noise ratio (SNR improved by $\sqrt{n}$=13). Multiple sets of scans confirm the reproducibility of the experimentally obtained signal. We can observe the two contributions

for the two hyperfine components of $6P_{1/2}$ separated by 1.168 GHz. For convenience from now, $6P_{1/2}(F = 3) \rightarrow 16S_{1/2}$ transition will be referred to as the large component (as $6P_{1/2}(F = 3)$ component is directly pumped) while the $6P_{1/2}(F = 4) \rightarrow 16S_{1/2}$ will be referred to the small component (because $6P_{1/2}(F = 4)$ component is indirectly populated by collisional redistribution).

In figure 5.3, we compare the theoretical FMSR lineshape (black line) in the absence of atom-surface interaction ($C_3 = 0$) having a natural linewidth (γ) of the 4.5 MHz (D_1 line) with experimentally obtained $6P_{1/2} \rightarrow 16S_{1/2}$ FMSR spectrum (Grey line). In contrast to the theoretical spectrum for $C_3 = 0$, the experimentally obtained FMSR signal exhibits a noticeable broadening and strong red-detuning, which demonstrates the expected behaviour of FMSR lineshapes under strong Rydberg-surface interactions.

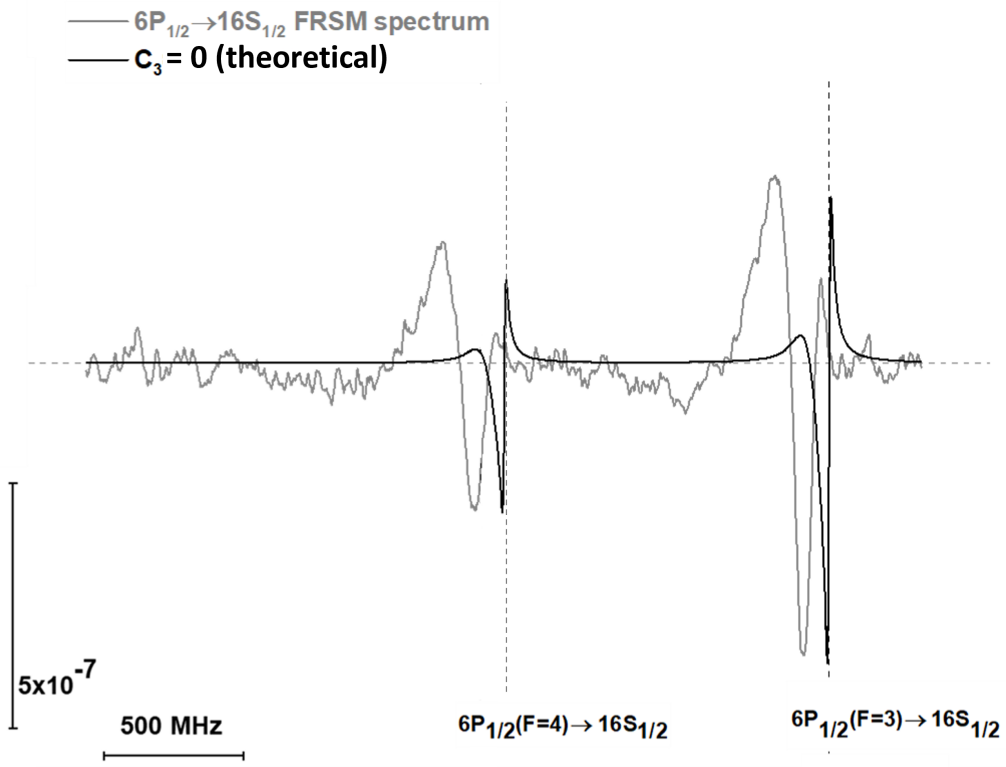

Figure 5.3: Comparison between FMSR lineshape in the absence of atom surface interaction i.e. C3 = 0 and γ = natural linewidth of the D_1 (black line) and experimentally obtained $6P_{1/2} \rightarrow 16S_{1/2}$ FMSR spectrum (Grey line). Signal amplitudes are normalized to off-resonant reflected power. Horizontal dashed line: zero references for each spectrum. Vertical dashed lines: frequency reference from $6P_{1/2} \rightarrow 16S_{1/2}$ absorption in volume.

5.2 Frequency modulated selective reflection spectroscopy on $6P_{1/2} \rightarrow 16S_{1/2}, 17S_{1/2}$ transition

5.2.1 Effect of pump and probe laser intensity

Before interpreting the experimental results, it is important to check the effect of pump and probe laser intensity on the FMSR lineshape. The pump and probe lasers are collimated and overlapped having relatively big beam areas of about 0.2 cm^2 and 0.125 cm^2 respectively measured using an Iris diaphragm. The normalized amplitudes of $6P_{1/2} \rightarrow 16S_{1/2}$ FMSR signal (normalized to the off-resonance reflected probe powers) remain constant on increasing the probe power without any noticeable effect on the lineshape, suggesting that the probe transition is not saturated (probe laser intensity increased up to 100 mW/cm^2). We subsequently explored the effect of pump power on our FMSR spectra. Figure 5.4 shows the normalized $6P_{1/2} \rightarrow 16S_{1/2}$ FMSR spectra at Cs vapour pressure of 10 mTorr for pump power intensities: 17 and 35 mW/cm^2.

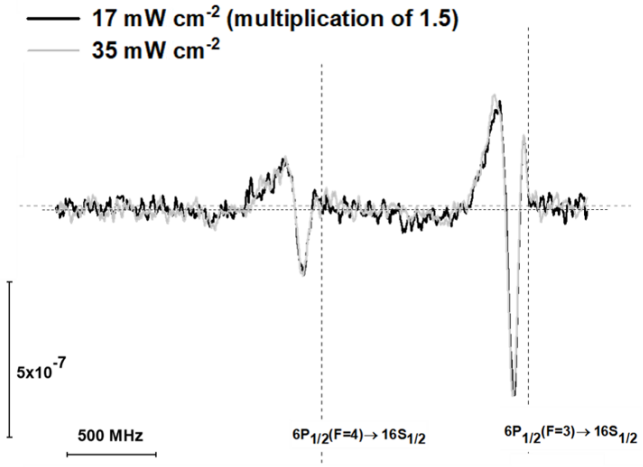

Figure 5.4: Normalized $6P_{1/2} \rightarrow 15D_{3/2}$ FMSR spectra for two pump intensities: 17 mW/cm^2 (black line, multiplied by 1.5 times) and 35 W/cm^2 (grey line) at a vapour pressure of 10 mTorr. Signal amplitudes are normalized to the off-resonant reflected probe powers. Horizontal dashed line: zero references for each spectrum. Vertical dashed lines: frequency reference from $6P_{1/2} \rightarrow 16S_{1/2}$ absorption in volume.

Doubling the pump intensity from 17 - 35 mW/cm^2 results in an increase of signal amplitude by approximately 1.5 times, indicating some saturation effect on the $6S_{1/2} \rightarrow 6P_{1/2}$

transition. Further increasing pump power while keeping the same vapour pressure would not result in a significant increase of the $6P_{1/2}$ population and thus the FMSR signal amplitude. Most importantly, no distortion of the lineshape was detected (increasing pump power affects only signal amplitude). Similar behaviour was observed for all the explored vapour pressures and other S states.

5.2.2 Fitting procedure of the FMSR spectra

Before proceeding with the details of the fitting procedure, we present a comparison between infinite Doppler approximation (black line) which assumes that $\gamma << kv_p$ (a flat velocity distribution $W(v) = 1/\sqrt{\pi}v_p$) and the Maxwell-Boltzmann velocity distribution (a numerically challenging model developed during this thesis) model with experimentally obtained $6P_{1/2} \rightarrow 16S_{1/2}$ FMSR spectrum (grey line) at a vapour pressure of 10 mTorr (figure 5.5).

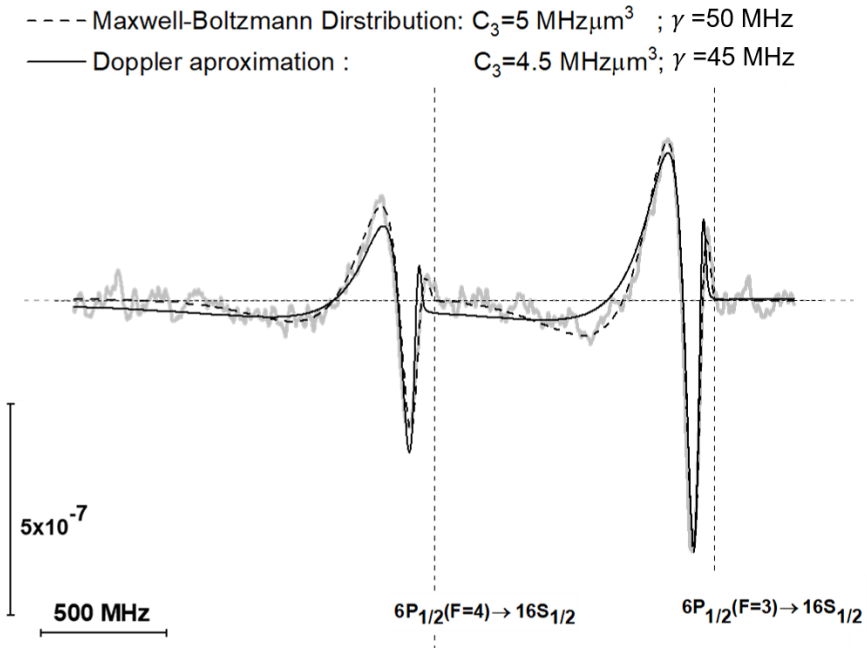

Figure 5.5: Fitting of normalized $6P_{1/2} \rightarrow 16S_{1/2}$ FMSR spectrum (grey line) at a vapour pressure of 10 mTorr with infinite Doppler approximation model (black line) and Maxwell Boltzmann velocity distribution model (dash line). Signal amplitude is normalized to the off-resonant reflected probe power. Horizontal dashed line: zero references for each spectrum. Vertical dashed lines: frequency reference from $6P_{1/2} \rightarrow 16S_{1/2}$ absorption in volume.

The experimental signal deviates significantly from the infinite Doppler approximation

model, primarily for the large red detuning part of the spectra. This is to be expected since the induced shift due to the Rydberg-surface interaction ($\sim$ 600 MHz at 200 nm atom surface separation) is comparable to or even larger than the Doppler width ($\sim$ 500 MHz FWHM). On the other hand, the novel model which incorporates the Maxwell-Boltzmann velocity distribution is more accurate in describing the experimental conditions. Henceforth, we employ this model for the interpretation of our experimental data.

Subsequently, we briefly discuss the effect of C_3 and Γ on the spread and asymmetry of the lineshape and how one can perform a visual inspection of the experimental curves compared to the theoretical curves for the first estimation of C_3 and γ.

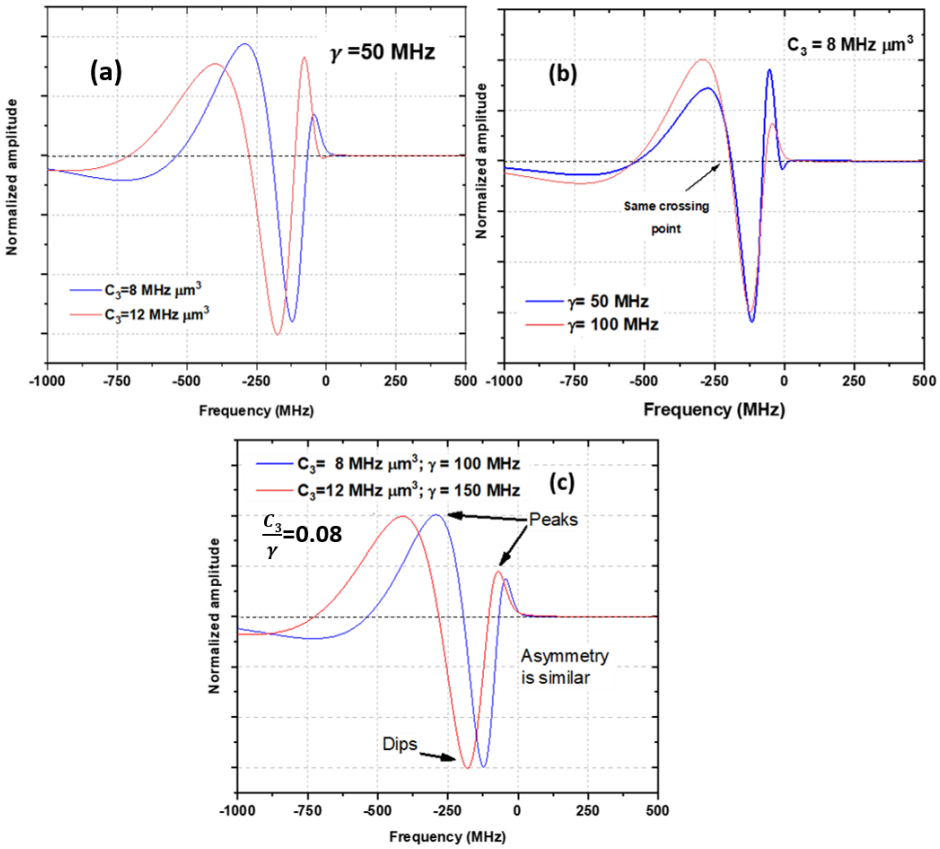

Figure 5.6: Normalized theoretical lineshape for different combination of C_3 and γ values (a) different C_3 having same γ (b) same C_3 with different γ (c) two different combination of C_3 and γ having same C_3/γ ratio (0.08). The amplitude is normalized to the maximum amplitude of the signal. Horizontal dashed line: zero references for each spectrum. The vertical zero line indicates the atomic resonance frequency.

Figure 5.6(a) shows the effects of C_3 on the lineshape while keeping γ constant. A larger C_3 coefficient shifts the curve further to the red side inducing an in-homogeneous broadening

(characteristic of Casimir-Polder interactions) [18]. Figure 5.6(b) shows that increasing γ while keeping the C_3 constant slightly broadens the curve and changes its symmetry (the ratio between successive peaks and dips in the curve). The zero crossing points (indicated in the figure) do not depend on γ and are essentially a measure of C_3. In figure 5.6(c), we plot two curves that have the same ratio $C_3/\gamma \sim 0.08$. The symmetry of the curve (ratio of amplitudes between successive peaks and dips) depends predominantly on the C_3/γ ratio. This is reminiscent of the dimensionless parameter $A = (2C_3/\gamma)$ [18] that universally defines the lineshapes in the case of the infinite Doppler approximation.

A simple inspection of the spread and asymmetry of the lineshape is therefore sufficient to extract a first estimate of the C_3 and γ parameters that best fit the experimental curve. We use this 'visual fit' to determine the starting points of our numerical fitting procedure that subsequently compares the experimental lineshapes with a library of theoretical FMSR lineshapes to extract the values of C_3 and γ that best fit our data. The best fit is here chosen by minimizing the Least Square Error. The fitting is performed using MATLAB code having 3 degrees of freedom:

- **Amplitude** : determines the magnitude of the predicted signal.
- **Shift**: adjusts the horizontal position along the frequency axis (X-axis).
- **Offset**: adjusts the vertical position along the Y axis.

By adjusting these 3 parameters, the MATLAB code optimizes the fit of the theoretical curve to the experimental signal by minimizing the least square error. We point out that in our spectra the offset is usually very small and bears no real significance in our spectra.

The two components of our FMSR signal (large and small) are sufficiently separated (spacing of 1.168 GHz) to be treated almost independently. First, we optimize the fit for the large component (that is almost completely independent of the small component). Then we fix the parameters of the large component and optimize the fit to find the parameters of the small component (including a small influence from the wings of the large component). Finally, the best-fitted curves for both components are combined for

a global fit.

Figure (5.7) shows fits for the normalized $6P_{1/2} \rightarrow 16S_{1/2}$ FMSR spectra obtained at a vapour pressure of 25 mTorr with the theoretical lineshapes having different combinations of C_3 and γ values. The best fit is achieved for $C_3 = 5$ MHz μm^3 with a $\gamma = 70$ MHz and $\gamma = 50$ MHz for the small and large components respectively (red curve). The theoretical lineshape converges closely with the experimental curve, yet a notable visual discrepancy arises in the fitting for C_3 values of 4 and 6 MHz μm^3 (the blue and green curves respectively). These fits are deemed unacceptable and offer an estimation of the error bars associated with our measurement of C_3.

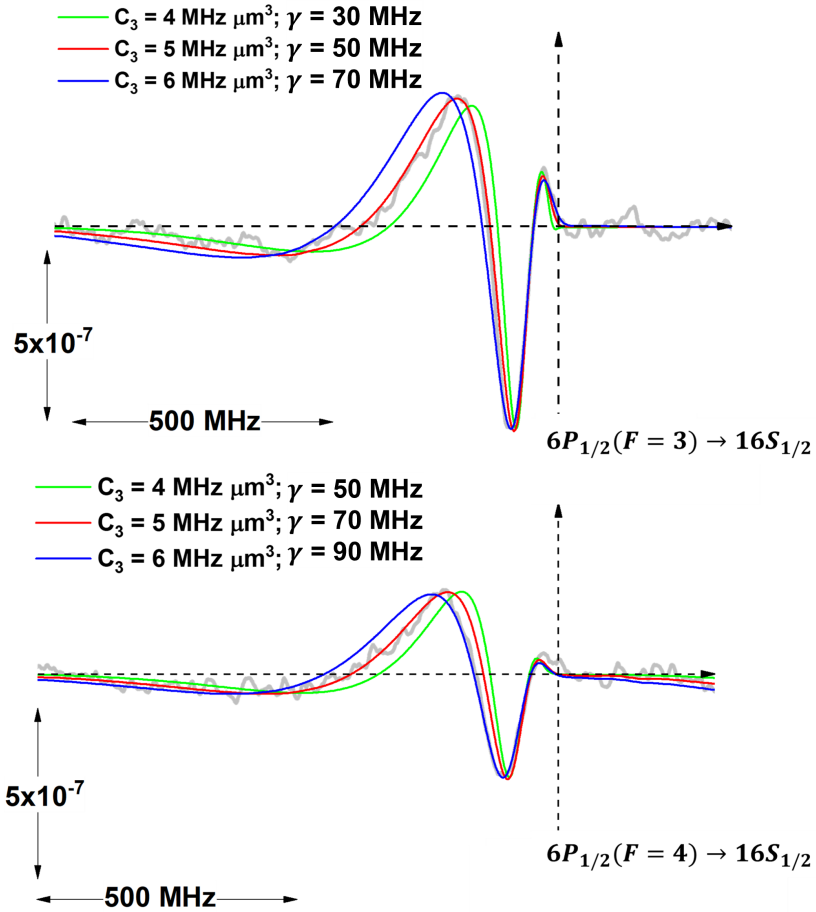

Figure 5.7: Fits of normalized $6P_{1/2} \rightarrow 16S_{1/2}$ FMSR spectra (obtained at Cs vapour pressure of $\sim$ 25 mTorr) with the theoretical lineshapes having different combinations of C_3 and γ values. FMSR signal amplitude is normalized to the off-resonant reflected probe power. Horizontal dashed line: zero references for each spectrum. Vertical dashed lines: frequency reference from $6P_{1/2} \rightarrow 16S_{1/2}$ absorption in volume.

A more comprehensive visual presentation of the fitting process would be a 3D surface

plot where the X-axis is C_3 (with a variation of 0.5 MHz μm^3), the Y-axis is linewidth, γ (with a variation of 10 MHz) and Z-axis being the least square error.

Figure 5.8 shows such surface plots for the big (a) and small (b) components of the FMSR spectra. These 3D representations provide a global view of the overall fitting results, making it easy to find the regions (marked with a circle in figure 5.7) for which the fits are acceptable, as well as the areas where the fit deviates from the experimental signal. For the large component (figure 5.8(a)), the optimal fit found is around $C_3 = 5.1 \pm 0.6$ MHz μm^3 and $\gamma = 50 \pm 15$ MHz (when the error bars are asymmetric, we have taken the biggest value). For the small component (figure 5.8(b)), the optimal fit lies around $C_3 = 5.5 \pm 1.2$ MHz μm^3 and $\gamma = 70 \pm 20$ MHz. A detailed analysis of the experiment FMSR signal will be provided in the next section.

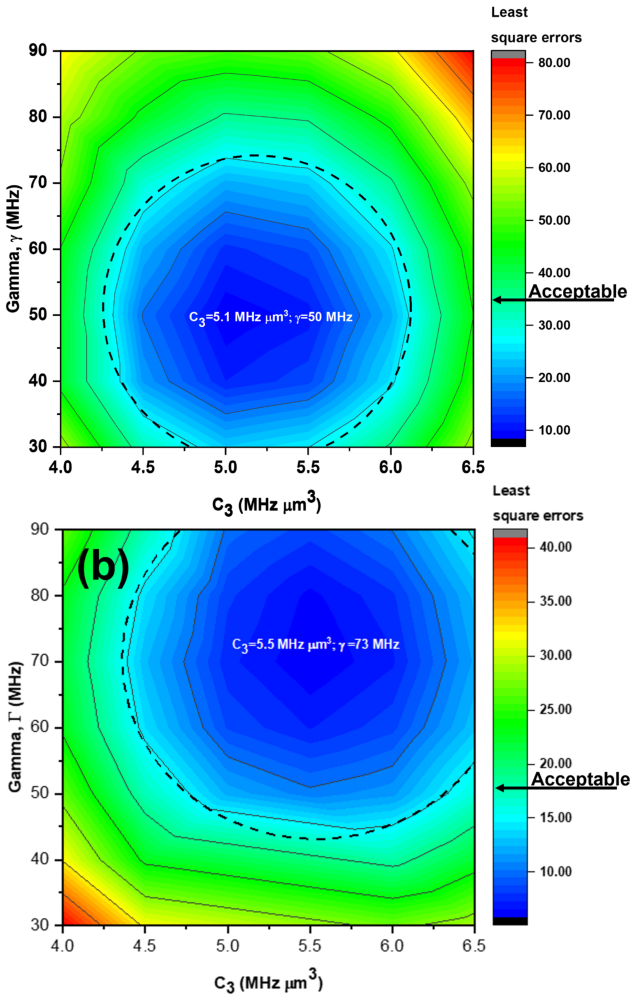

Figure 5.8: 3D contour plot of the least square error (Z-axis) mapped with colours with X-axis being C_3 (MHz μm^3) and Y-axis being γ (MHz) for (a) large component i.e. $6P_{1/2}(F = 3) \rightarrow 16S_{1/2}$) and (b) small component i.e. $6P_{1/2}(F = 4) \rightarrow 16S_{1/2}$).

5.2.3 C_3 and γ measurement from $6P_{1/2} \rightarrow 16S_{1/2}, 17S_{1/2}$ FMSR spectra

In figure 5.9 and 5.10, we show the best fit for the normalized $6P_{1/2} \rightarrow 16S_{1/2}, 17S_{1/2}$ FMSR signal (signal amplitudes are normalized to the off-resonant reflected powers) at different caesium vapour pressures.

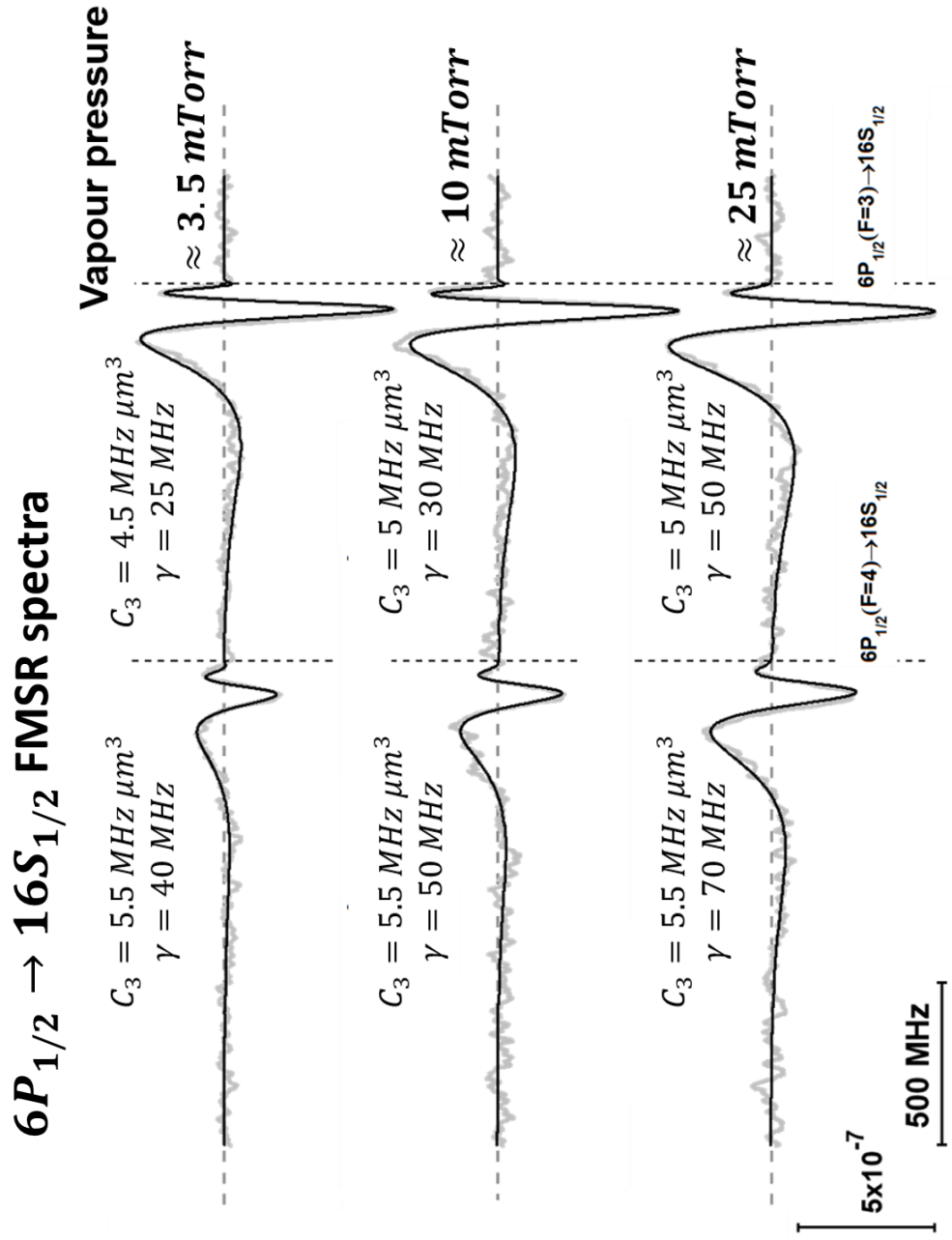

Figure 5.9: Best fit (black line) for $6P_{1/2} \rightarrow 16S_{1/2}$ FMSR signal (grey line) for different caesium vapour pressure. FMSR signal amplitude is normalized to the off-resonant reflected probe powers. Horizontal dashed line: zero references for each spectrum. Vertical dashed lines: frequency reference from $6P_{1/2} \rightarrow 16S_{1/2}$ absorption in volume.

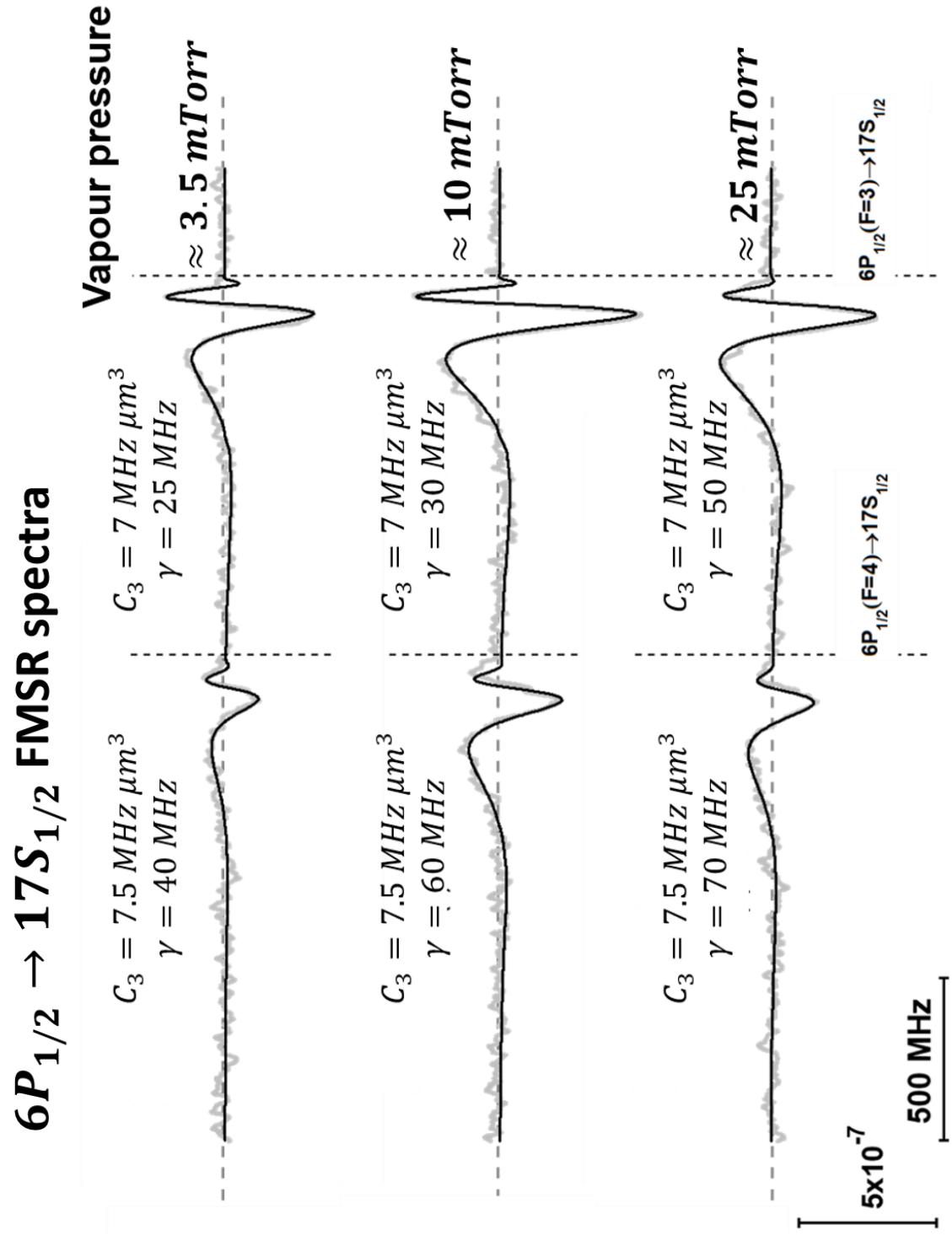

Figure 5.10: Best fit (black line) for $6P_{1/2} \rightarrow 17S_{1/2}$ FMSR signal (grey line) for different caesium vapour pressure. FMSR signal amplitude is normalized to the off-resonant reflected probe powers. Horizontal dashed line: zero references for each spectrum. Vertical dashed lines: frequency reference from $6P_{1/2} \rightarrow 17S_{1/2}$ absorption in volume.

The measured C_3 (in MHz μm^3) values for both $16S_{1/2}$ and $17S_{1/2}$ states are shown in figure 5.11 as a function of caesium vapour pressure (mTorr). As expected, increasing the vapour pressure does not influence the strength of Casimir-Polder interactions. We find that $C_3(16S_{1/2}) = 5.1 \pm 1$ MHz μm^3, (with a theoretical prediction of ~ 3.5 MHz μm^3) and $C_3(17S_{1/2}) = 7.35 \pm 1.2$ MHz μm^3 (with a theoretical prediction of ~ 4.7 MHz μm^3). Although the measured C_3 remains about 1.5 times bigger than theoretical predictions for both states, it is interesting to notice that it scales as $n^{\star 4}$ (theoretically predicted scaling law, see section 2.3).

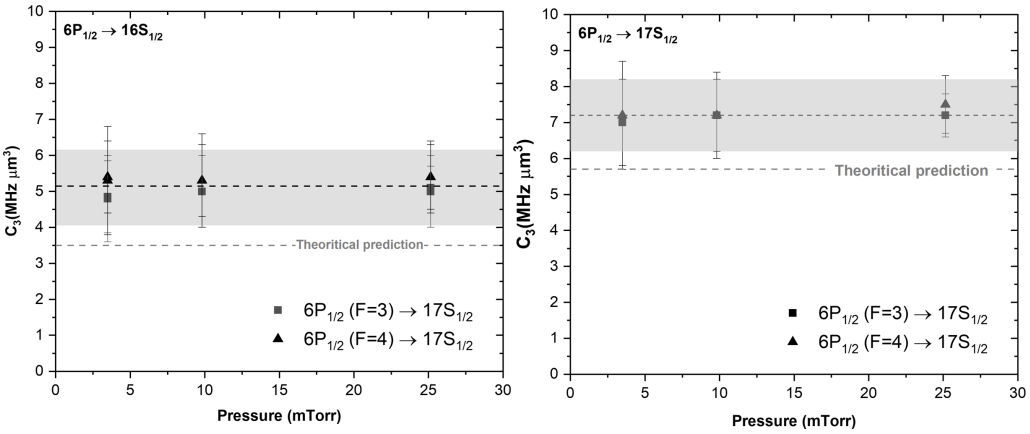

Figure 5.11: Extracted C_3 values (in MHz μm^3) as a function of Cs vapour pressure (in mTorr) for $16S_{1/2}$ (left) and $17S_{1/2}$ (right) states. Grey dashed line: predicted C_3 value for a sapphire surface. Square marker: larger transition ($6P_{1/2}(F = 3) \rightarrow nS_{1/2}$). Triangle marker: small transition ($6P_{1/2}(F = 4) \rightarrow nS_{1/2}$). The grey-shaded area shows the uncertainty in C_3 measurements.

Figure 5.12 shows the extracted γ values as a function of Cs vapour pressure. The homogeneous linewidth evolves linearly with vapour pressure with a slope of about 1GHz/Torr, a value not incompatible with expected values for pressure broadening for the $16S_{1/2}$ and $17S_{1/2}$ states (see discussion in the previous chapter and [74]). However, a systematic difference in the extracted value γ is observed between the small and large components. This discrepancy could be because the velocity distribution of excited atoms in the directly pumped hyperfine state could deviate significantly from a thermal Maxwell-Boltzmann distribution assumed in our model. We should note that in previous works [38], utilising the same two-step excitation steps for selective reflection spectroscopy the directly pumped component was discarded (for the above reason) and only the small component

(pumped via collisions) was analysed for a C_3 measurement. This represents the first attempt to perform such analysis, motivated partly by the small signal-to-noise ratio of our measurements. The influence of direct two-photon excitation could also be a reason for discrepancies between the two extracted linewidths. Nevertheless, it is interesting to note again that besides this discrepancy, the theoretical model fits the experiment very well and the extracted C_3 value (the main goal of this experiment) is compatible with both hyperfine (small and large) components. An analysis of FMSR lineshapes using a combination of Gaussian (representing the thermal part of the distribution) and Lorentzian (representing the directly pumped atoms) distributions would be interesting for further investigation (not included in this thesis statement).

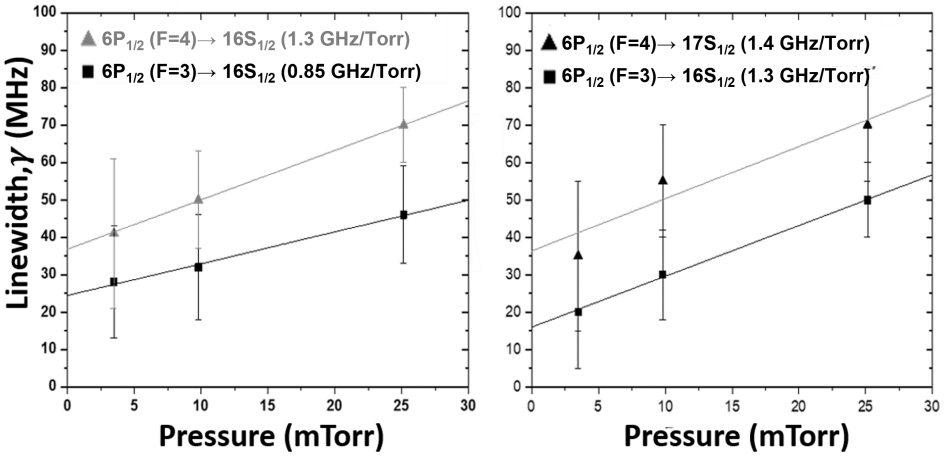

Figure 5.12: Extracted homogeneous linewidth γ (in MHz) for $16S_{1/2}$ and $17S_{1/2}$ states as a function of Cs vapour pressure. The dashed lines show the linear growth of the homogeneous linewidth. Triangle marker : small transition $(6P_{1/2}(F = 4) \rightarrow nS_{1/2})$,square marker: the larger transition $(6P_{1/2}(F = 3) \rightarrow nS_{1/2})$.

5.3 Frequency modulated selective reflection spectroscopy of $15D_{3/2}$ $17D_{3/2}$ and $18D_{3/2}$

5.3.1 Effect of pump and probe laser intensity

Similarly, to the $nS_{1/2}$ states, the normalised amplitude of the $6P_{1/2} \rightarrow nD_{3/2}$ transitions (normalized to the off-resonant reflected probe powers) remains independent of probe power, suggesting that the probe transition is not saturated. However, $nD_{3/2}$ states were

not so well behaved as the $nS_{1/2}$ states for high pump laser powers. This is illustrated in Figure 5.13 where the normalized $6P_{1/2} \rightarrow 15D_{3/2}$ FMSR spectra are shown for different pump intensities (12, 17, 25, and 35 mW/cm^2) for Cs vapour pressure of 25 mTorr. High pump intensity induces a distortion (changes in the symmetries i.e. the ratio between the successive peaks and dips) and an overall blue shift in the FMSR lineshapes, that only disappears for pump intensities below 17 mW/cm^2. For lower vapour pressure (figure 5.14) further decrease of pump intensity is required to avoid the reported blue shift FMSR signal. This behaviour is consistently observed for all the probed $nD_{3/2}$ lines. This behaviour new observation and is not yet well understood.

One intuitive hypothesis revolves around the fact that the large electric dipole moments associated with Rydberg states are particularly sensitive to stray fields. The Stark shift of these Rydberg states due to these stray electric fields can induce either blue or red shifts, contingent upon the atomic state. To have a concrete understanding, further measurements are needed to measure the possible effects of stray fields. But for now, to avoid any lineshape distortions, we performed the FMSR experiment for the $nD_{3/2}$ lines with low pump intensity of $\sim$ 17 mW/cm^2.

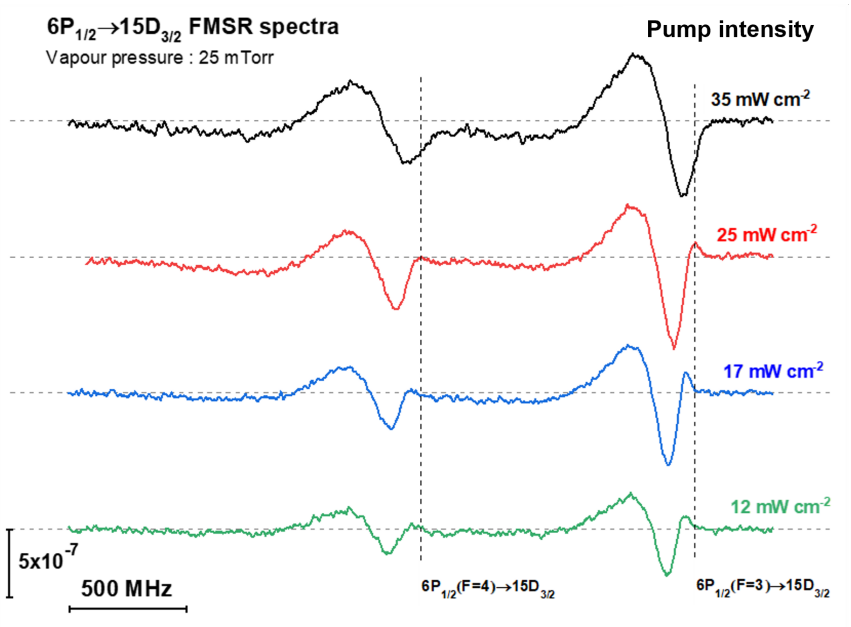

Figure 5.13: $6P_{1/2} \rightarrow 15D_{3/2}$ FMSR spectra for pump intensities: 12, 17, 25, and 35 mW/cm^2 & Cs vapour pressure: $\sim$ 25 mTorr. Signal amplitudes are normalized to off-resonant reflected probe powers. Horizontal dashed line: zero reference. Vertical dashed lines: frequency reference from $6P_{1/2} \rightarrow 15D_{3/2}$ absorption in volume.

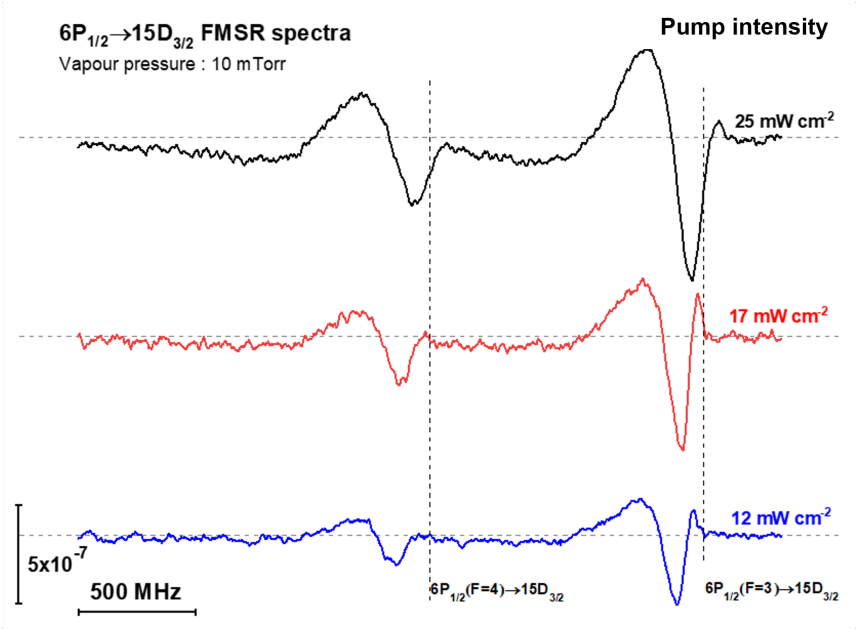

Figure 5.14: $6P_{1/2} \rightarrow 15D_{3/2}$ FMSR spectra for pump intensities: 12, 17 and 25 mW/cm^2 & Cs vapour pressure: $\sim$ 10 mTorr. Signal amplitudes are normalized to off-resonant reflected probe powers. Horizontal dashed line: zero reference. Vertical dashed lines: frequency reference from $6P_{1/2} \rightarrow 15D_{3/2}$ absorption in volume.

5.3.2 Relative amplitude of $6P_{1/2} \rightarrow nS_{1/2}, nD_{3/2}$ (n = 15 - 17) FMSR spectra

Assuming all experimental conditions remain unchanged (caesium density, pump and probe power), the relative amplitude of $6P_{1/2} \rightarrow nS_{1/2}$ and $6P_{1/2} \rightarrow nS_{1/2}$ transitions should depend exclusively on the square of the dipole matrix element, shown in table 5.1. The above statement should hold for any linear spectroscopy technique (both selective reflection and linear absorption).

In figure 5.15, we present the normalized $6P_{1/2} \rightarrow nS_{1/2}, nD_{3/2}$ (n=15-17) absorption spectra obtained in the volume of 1 cm long vapour cell (section 4.2.2.3, the transition are not influenced by atom surface interaction) at a relatively low caesium vapour pressure of 0.08 mTorr. The amplitudes of the signals are first normalized to the off-resonant transmitted probe powers and then to the amplitude of the $6P_{1/2} \rightarrow 15D_{3/2}$ transition with appropriate multiplication factors. These multiplication factors (shown in figure 5.15) are in good accordance with the expected ratios given by Table 5.1 (theoretical predictions).

$6P_{1/2} \rightarrow$	$\lvert\langle j_1 \lvert \mathrm{p} \rvert j_2\rangle\rvert^2$ normalized to $\lvert\langle 6P_{1/2} \lvert \mathrm{p} \rvert 15D_{3/2}\rangle\rvert^2$
$15D_{3/2}$	1
$16D_{3/2}$	1.2
$17D_{3/2}$	1.5
$16S_{1/2}$	8.3
$17S_{1/2}$	10.2

Table 5.1: Square of reduced dipole matrix elements $\lvert\langle 6P_{1/2} \lvert \mathrm{p} \rvert nS_{1/2}, nD_{3/2}\rangle\rvert^2$ transition where n= 15 - 17 normalized $\lvert\langle 6P_{1/2} \lvert \mathrm{p} \rvert 15D_{3/2}\rangle\rvert^2$.

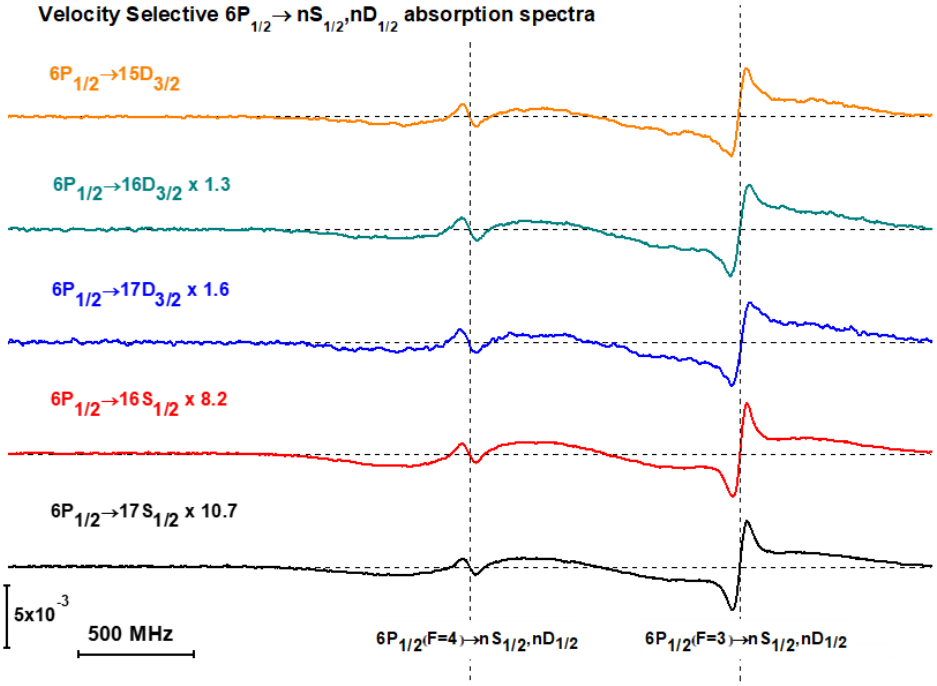

Figure 5.15: Velocity-selective $6P_{1/2} \rightarrow nS_{1/2}, nD_{3/2}$ (n = 15 - 17) absorption spectra in a 1 cm cell at $\sim$ 0.08 mTorr Cs vapor pressure. The amplitudes of absorption signals are first normalized to off-resonant transmitted probe powers and then to the maximum amplitude of the $6P_{1/2} \rightarrow 15D_{3/2}$ transition with appropriate multiplication factors. Horizontal dashed line: zero reference. Vertical dashed lines: frequency reference from $6P_{1/2} \rightarrow nS_{1/2}, nD_{3/2}$ absorption in volume.

In figure 5.16 we compare the relative amplitude of $6P_{1/2} \rightarrow 15D_{3/2}$ and $6P_{1/2} \rightarrow 16S_{1/2}$ FMSR spectra at Cs vapour pressure of $\sim$ 20 mTorr for pump laser intensity of 35 mW/cm^2. The amplitudes of the FMSR signals are normalized to the off-resonant probe power. Contrary to linear absorption, the amplitude of FMSR signals on the $D_{3/2}$ line is

less than the theoretically expected value (around 8). A quick inspection of figure 5.16 suggests that the two signals have roughly the same amplitude. However, a proper comparison of the experimental signals with the theoretical predictions, taking into account the linewidth of the signals, suggests that the $6P_{1/2} \rightarrow 15D_{3/2}$ signal is about 2 times larger than the $6P_{1/2} \rightarrow 16S_{1/2}$ signal. The apparent reduction of signal amplitude when probing D states is an experimental observation for which we have not as of yet a clear explanation.

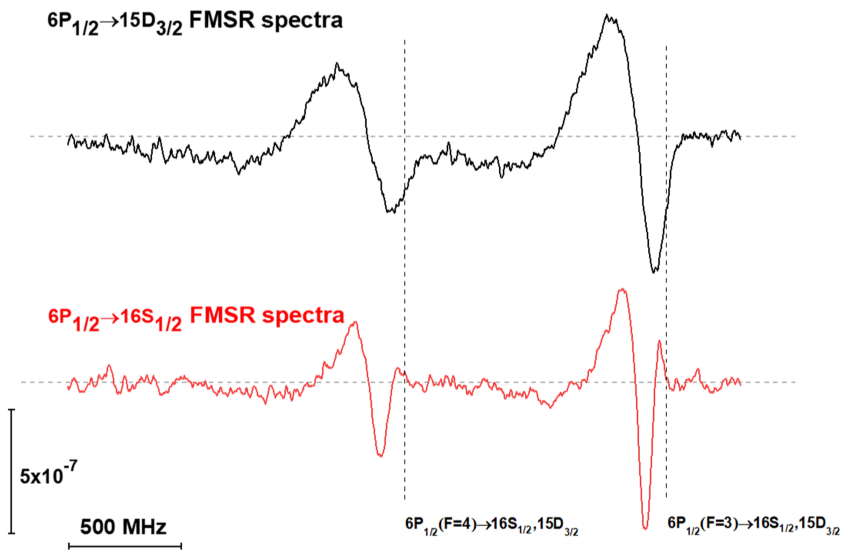

Figure 5.16: FMSR spectra for $6P_{1/2} \rightarrow 15D_{3/2}, 16S_{1/2}$ (black and red line respectively) at Cs vapour pressure: $\sim$ 20 mTorr & pump laser intensity: 35 mW/cm^2. FMSR signal amplitudes are normalized to the off-resonant reflected probe powers. Horizontal dashed line: zero references for each spectrum. Vertical dashed lines: frequency reference from $6P_{1/2} \rightarrow 15D_{3/2}, 16S_{1/2}$ absorption in volume.

5.3.3 C_3 and γ measurement from $6P_{1/2} \rightarrow 15D_{3/2}, 16D_{3/2}$ and $17D_{3/2}$ FMSR spectra

In figure 5.17 - 5.20, we show the experimental FMSR spectra along with the best fits obtained on the $6P_{1/2} \rightarrow 15D_{3/2}, 16D_{3/2}$ and $17D_{3/2}$ transitions. Figures 5.17 and 5.18 show the $6P_{1/2} \rightarrow 15D_{3/2}$ FMSR spectra obtained at different caesium vapour pressures for 17 (black line) and 12 (red line) mW/cm^2 pump intensities respectively. At these low pump intensities, no distortion of the lineshape was detected when probing the $D_{3/2}$ states. However, due to the smaller signal amplitude, it was challenging to obtain a respectable

signal-to-noise ratio for probing higher states such as $16D_{3/2}$ and $17D_{3/2}$. Figure 5.19 and 5.20 show the normalized FMSR lineshapes on the $6P_{1/2} \rightarrow 16D_{3/2}, 17D_{3/2}$ transitions for different caesium vapour pressure for a pump intensity of 17 mW/cm^2. The signal amplitudes are normalized to the off-resonant probe powers.

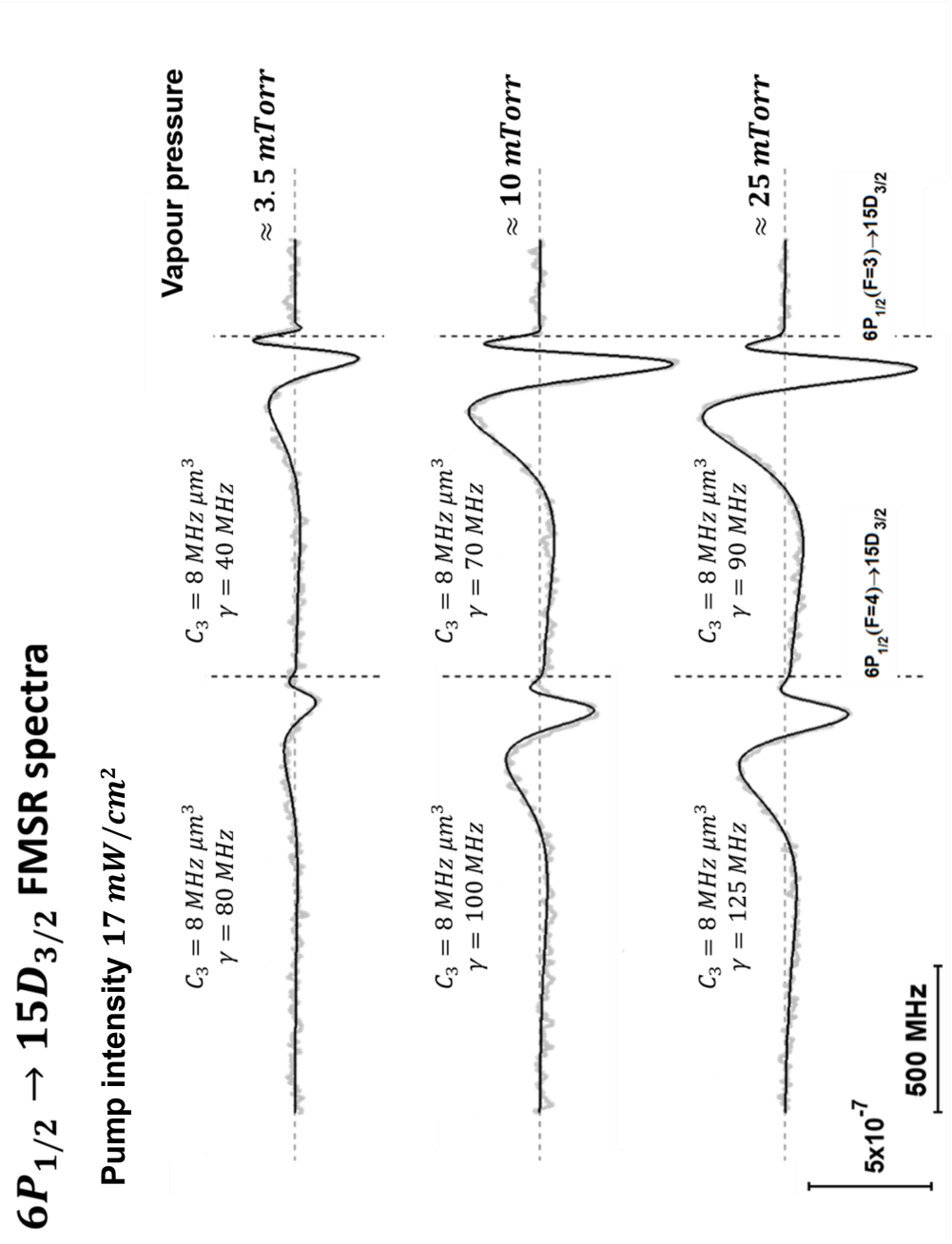

Figure 5.17: Best fit (black line) for $6P_{1/2} \rightarrow 15D_{3/2}$ FMSR signal (grey line) for different caesium vapour pressure. FMSR signal amplitudes are normalized to the off-resonant reflected probe powers. Pump laser intensity: 17 mW/cm^2. Horizontal dashed line: zero references for each spectrum. Vertical dashed lines: frequency reference from $6P_{1/2} \rightarrow 15D_{3/2}$ absorption in volume.

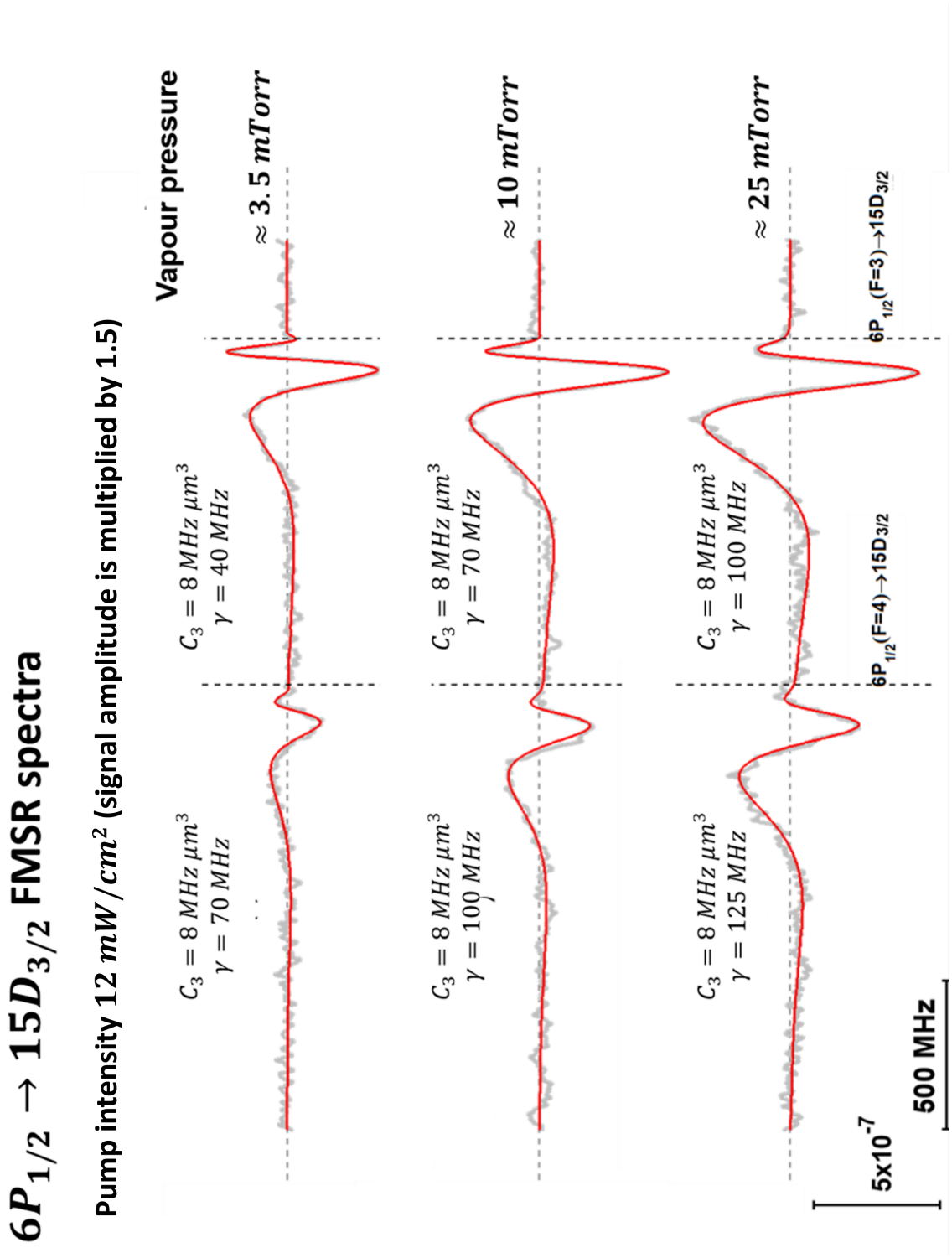

Figure 5.18: Best fit (red line) for $6P_{1/2} \rightarrow 15D_{3/2}$ FMSR signal (grey line) for different caesium vapour pressure. FMSR signal amplitudes are normalized to the off-resonant reflected probe powers. Pump laser intensity: 12 mW/cm^2. Horizontal dashed line: zero references for each spectrum. Vertical dashed lines: frequency reference from $6P_{1/2} \rightarrow 15D_{3/2}$ absorption in volume.

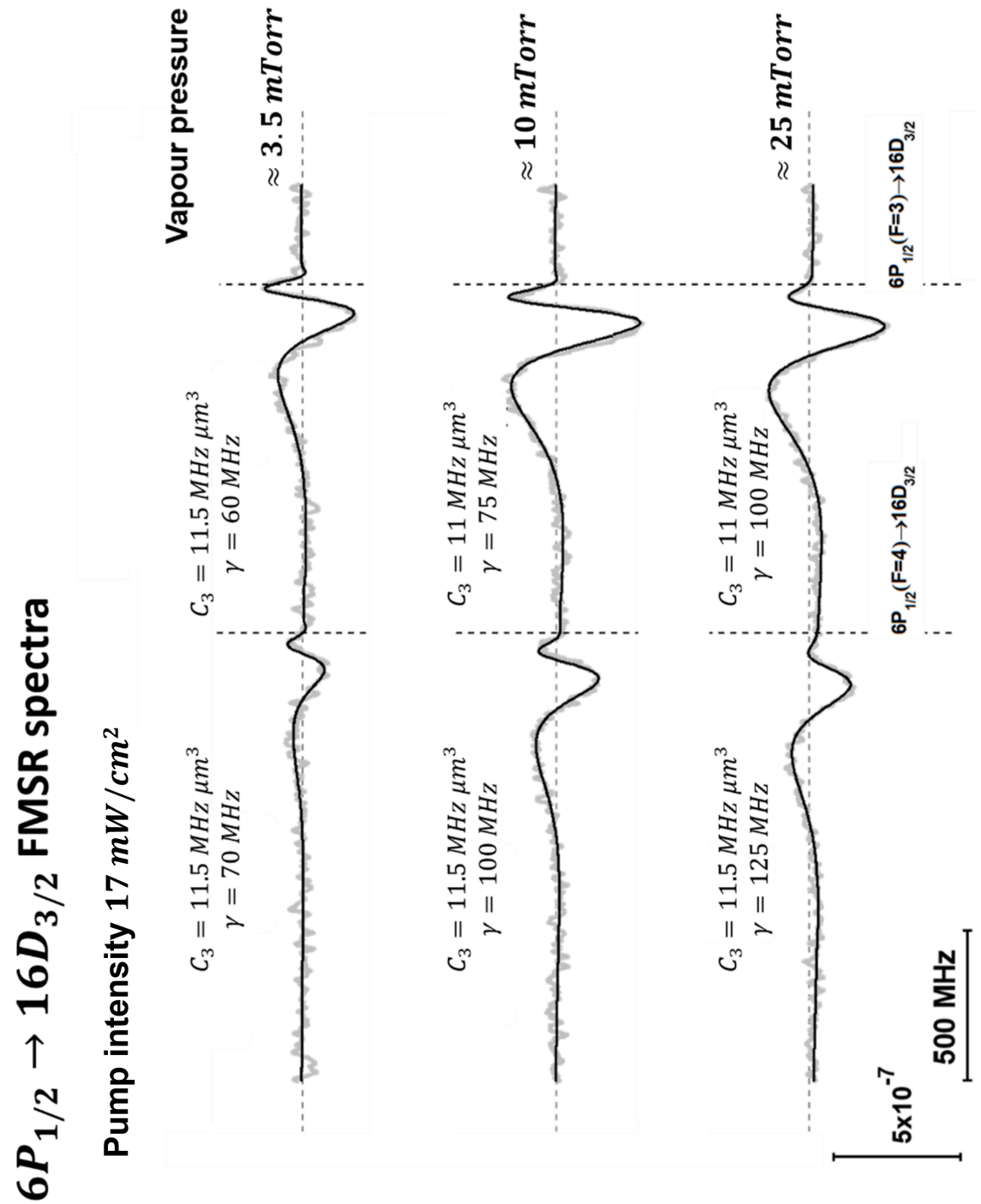

Figure 5.19: Best fit (black line) for $6P_{1/2} \rightarrow 16D_{3/2}$ FMSR signal (grey line) for different caesium vapour pressure. FMSR signal amplitudes are normalized to the off-resonant reflected probe powers. Pump laser intensity: 17 mW/cm^2. Horizontal dashed line: zero references for each spectrum. Vertical dashed lines: frequency reference from $6P_{1/2} \rightarrow 16D_{3/2}$ absorption in volume.

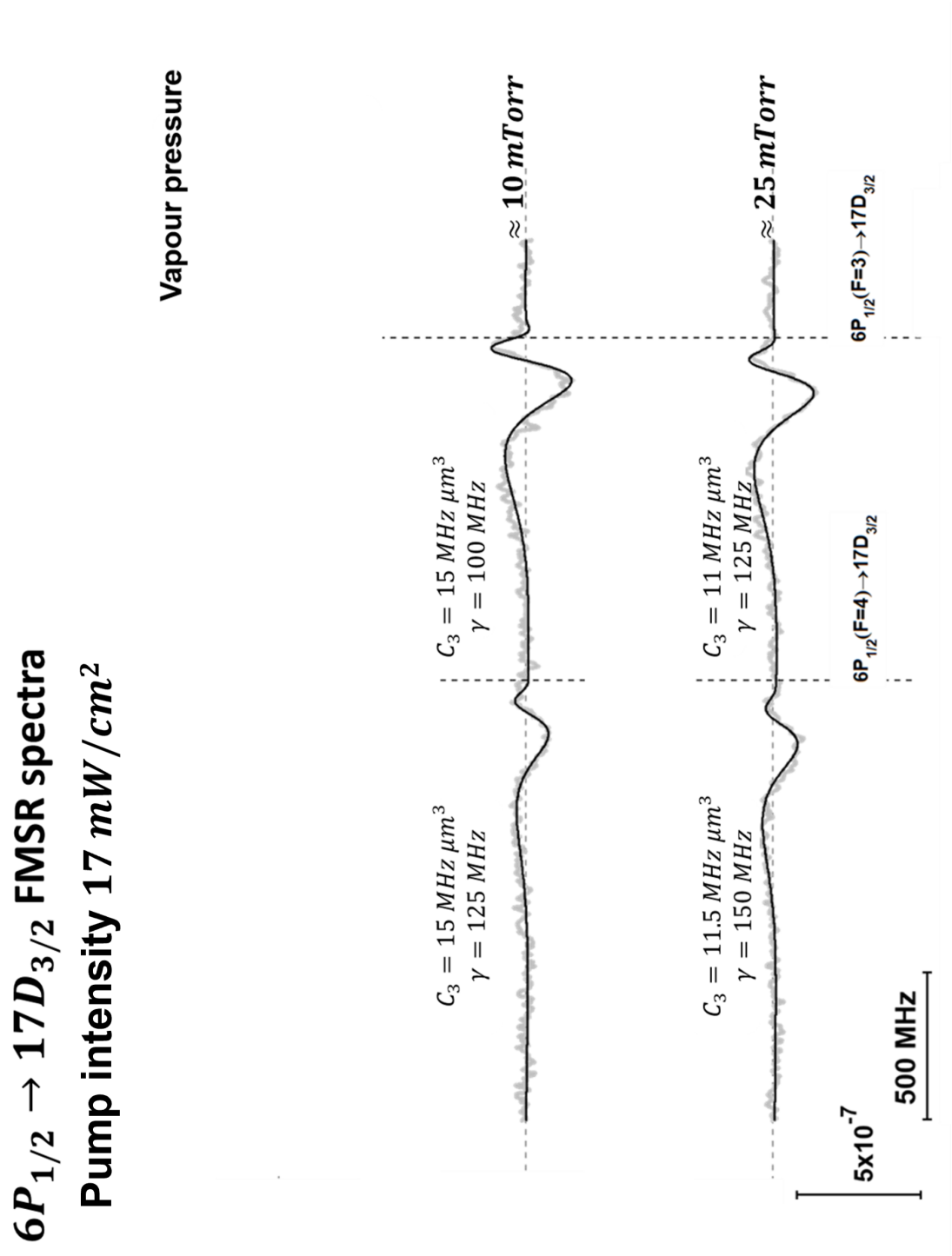

Figure 5.20: Best fit (black line) for $6P_{1/2} \rightarrow 17D_{3/2}$ FMSR signal (grey line) for different caesium vapour pressure. FMSR signal amplitudes are normalized to the off-resonant reflected probe powers. Pump laser intensity: 17 mW/cm^2. Horizontal dashed line: zero references for each spectrum. Vertical dashed lines: frequency reference from $6P_{1/2} \rightarrow 17D_{3/2}$ absorption in volume.

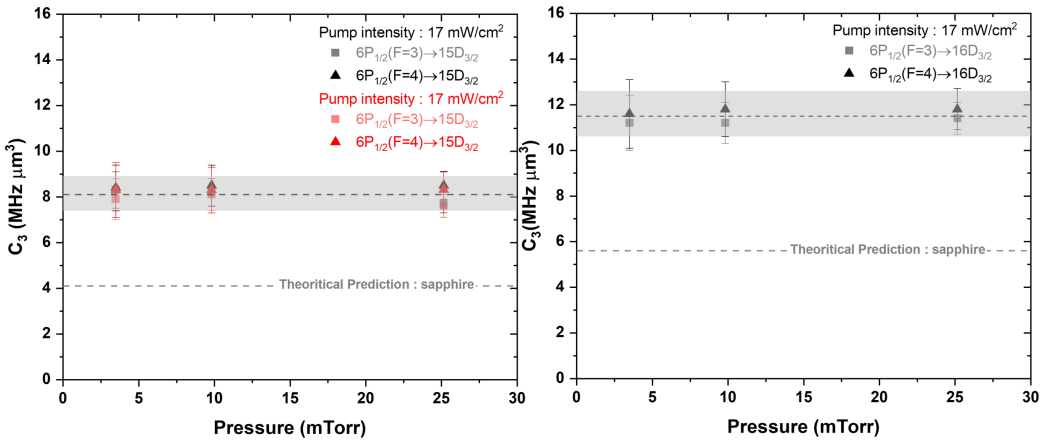

Figure 5.21: Extracted C_3 values (in MHz μm^3) as a function of Cs vapour pressure (in mTorr) for $15D_{3/2}$ state (left) for pump intensities: 17 (black marker), 12 (red marker) mW/cm^2 and $16D_{3/2}$ (right) states for pump intensity 17 mW/cm^2 (black marker). Grey dashed line: predicted C_3 value for a sapphire surface. Triangle marker: small transition ($6P_{1/2}(F = 4) \rightarrow nD_{3/2}$). Square marker: larger transition ($6P_{1/2}(F = 3) \rightarrow nD_{3/2}$). The grey-shaded area shows the uncertainty in C_3 measurements.

Figure 5.21 shows the extracted C_3 (in MHz μm^3) values as a function of caesium vapour pressure (mTorr) for both the $15D_{3/2}$ and $16D_{3/2}$ states. The extracted values are independent of vapour pressure giving: $C_3(15D_{3/2}) = 8.1 \pm 1$ MHz μm^3 (with a prediction of ~ 4.1 MHz μm^3), $C_3(16D_{3/2}) = 11.3 \pm 1.3$ MHz μm^3 (with a prediction of ~ 5.7 MHz μm^3) and $C_3(17D_{3/2}) = 15 \pm 2$ MHz μm^3 (with a prediction of ~ 8.9 MHz μm^3). It can be seen that the experimental measurements exceed the theoretical predictions, in this case by a factor of 2, larger than the 1.5 factor observed for the S states (section 5.2). We should note that the extracted C_3 value for the $17D_{3/2}$ state slightly deviates from the $(n^*)^4$ scaling. However, this could be attributed to the relatively large uncertainty of this measurement (the signal-to-noise ratio degrades significantly for this transition).

Figure 5.22 shows the extracted linewidth, γ values as a function of vapour pressure for the $6P_{1/2} \rightarrow 15D_{3/2}, 16D_{3/2}$ transitions. The homogeneous linewidth, γ evolves linearly with vapour pressure with a slope of about 2 GHz/Torr, which is compatible with the measurement we obtained in the volume experiment (as discussed in section 4.3.2 pressure broadening ~ 2 GHz/Torr for $6P_{1/2} \rightarrow 15D_{3/2}$ transition). Similar to the S states, a systematic difference in homogeneous linewidth for the small and large components can be also observed for the $D_{3/2}$ line which can be again attributed to the fact that

the directly pumped component of $6P_{1/2}$ state can significantly deviate from a thermal Maxwell- Boltzmann distribution that we have considered in our theoretical model. Nevertheless, like the $S_{1/2}$ states, the extracted C_3 value for $D_{3/2}$ remains consistent with caesium vapour pressure.

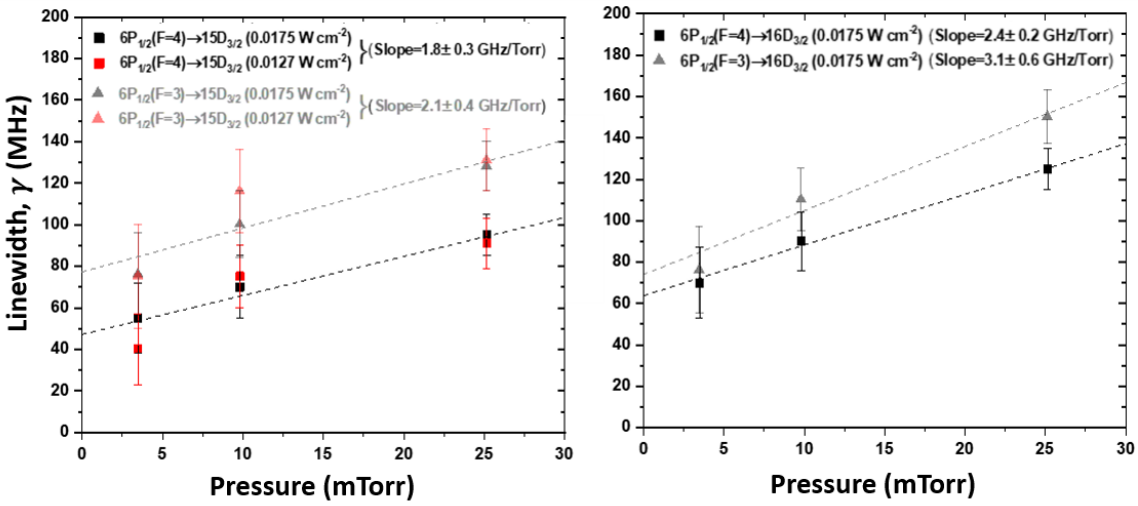

Figure 5.22: Measured homogeneous linewidth, γ (in MHz) as a function of Cs vapour pressure for $15D_{3/2}$ and $16D_{3/2}$. Red and black marker indicates the measurement for a pump power of 12 and 17 mW/cm^2 respectively. Triangle marker indicates the small transition ($6P_{1/2}(F = 4) \rightarrow nD_{3/2}$) and square marker indicates the larger transition ($6P_{1/2}(F = 3) \rightarrow nD_{3/2}$).

5.3.4 Remarks

The novel numerical model that we have developed in the course of this thesis (chapter 3) reproduces our experimental spectra nicely and allows us to extract the C_3 and γ values. For $6P_{1/2} \rightarrow nS_{1/2}, nD_{3/2}$, we have observed that the extracted C_3 values remain consistent with caesium vapour pressure but exceed the theoretical predictions (by a factor of 1.5 or 2, see chapter 2). This inconsistency with theory is more pronounced when probing the $nD_{3/2}$ lines. This discrepancy between theory and experiment is larger than in previously reported FMSR measurements [43][45][38]. We also found that the homogeneous linewidth, γ also remains linear with the caesium vapour pressure and the value remains slightly larger for the large components (directly pumped) than the small component (indirectly pumped). This can be attributed to the fact that the directly pumped $6P_{1/2}$ component can have a velocity distribution different from Maxwell Boltzmann (some

combination of Maxwell Boltzmann and Lorentzian). We are currently pushing our experiments further, by performing thin-cell spectroscopy on the same Rydberg states. The use of thin cells could illuminate the observed discrepancy between theory and experiment and also hold the potential for uncovering the influence of higher-order interactions. It is important to note that the thin cell spectroscopy work is still in its preliminary stages and further measurement and analysis are ongoing. The numerical model for thin-cell spectroscopy accounting for highly excited atom surface interaction developed during the thesis can act as an essential tool for the analysis of the thin-cell spectra in future. In the concluding chapter of this thesis, we offer a comprehensive summary of the entire work and present initial findings from thin cell spectroscopy along with some future perspectives.

Chapter 6

Conclusion and Perspectives

6.1 Overview of this thesis

In this thesis, we revisited the formalism for calculating atom-surface interactions in the non retarded limit incorporating higher-order interaction energy terms (quadrupole and octupole). Using the electrostatic approach, we provided explicit calculations for predicting the dipole interaction coefficient C_3 as well as the quadrupole interaction coefficient C_5 for highly excited Rydberg states.

We also developed a numerical method to simulate selective reflection and thin cell spectroscopy accounting for all velocity components (Maxwell velocity distribution) of the atomic vapour. We showed the necessity of the new model for predicting SR lineshapes in the presence of strong atom-surface interactions. With our calculations of C_3 and C_5 coefficients and our model for calculating selective reflection and thin cell spectra, we examine the conditions under which higher-order interactions could be experimentally observable.

Finally, we presented our frequency-modulated selective reflection (FMSR) experiment on $6P_{1/2} \rightarrow nS_{1/2}, nD_{3/2}$ transitions (n = 15 - 17). Detailed analysis of the experimental spectra allowed us to measure the C_3 coefficients of the $Cs(nS_{1/2})$ and $Cs(nD_{3/2})$ states

interacting with a sapphire surface. Surprisingly, we observe that the C_3 coefficients of the $nS_{1/2}$ states are about 1.5 times larger than theoretically predicted, while C_3 coefficients of the $nD_{3/2}$ states are about 2 times larger. Even more surprisingly, we have observed that the experimentally measured amplitude ratio between the $6P_{1/2} \rightarrow 15D_{3/2}$ and the $6P_{1/2} \rightarrow 16S_{1/2}$ FMSR signals is smaller than the ratio of probabilities of the two transitions. This is the first observed linearity breakdown in FMSR spectroscopy which remains for the moment without explanation. We are conducting a comprehensive investigation into other S and D states on various surfaces (such as glass and YAG), as well as examining the potential impact of stray fields. which can offer a meaningful explanation in the near future.

6.2 Preliminary work on probing Rydberg atoms in nanometric thin cell

Given the discrepancies between the predicted and extracted C_3 values, we are currently exploring these Rydberg transitions in a nanometric cell having a thickness ranging from 30 nm to 1µm [23]. Thin cell (TC) spectroscopy offers a promising opportunity to validate the discrepancies observed in the case of SR spectroscopy. Furthermore, it may serve as a valuable method for probing higher-order transitions (as discussed in Chapter 3). The experimental configuration is similar to the SR spectroscopy (figure 4.2) and we perform our spectroscopic measurement simultaneously on the transmitted and reflected beam from the thin cell. Our first measurements focused on probing the $6P_{1/2} \rightarrow 16S_{1/2}$ transition (at 513nm). The pump laser is amplitude modulated (AM) and locked on the $6S_{1/2}(F = 3, 4) \rightarrow 6P_{1/2}(F = 4)$ transition. In thin-cell experiments we did not deploy frequency modulations on the probe laser as we were expecting a huge broadening of the lineshape due to the interaction with two surfaces and the probe signal was only demodulated at the AM (pump) frequency.

In Figure 6.1, we present preliminary normalized $6P_{1/2} \rightarrow 16S_{1/2}$ thin-cell transmission spectra for different cell thicknesses L (signal amplitudes are firstly normalized to off-

resonance transmission probe powers and then normalized to the maximum amplitude of transmission spectra at 640 nm for Cs vapour pressure of ~ 0.27 Torr). With decreasing cell thickness L, increasing redshift of atomic resonance and homogeneous broadening of the lineshapes are nicely visible. This is a clear demonstration of strong Rydberg-atom surface interactions. The contribution of the second hyperfine component (small component) is strongly suppressed and is only visible for large cell thicknesses. This is probably because collisions with the cell walls dominate over inter-atomic collisional redistribution.

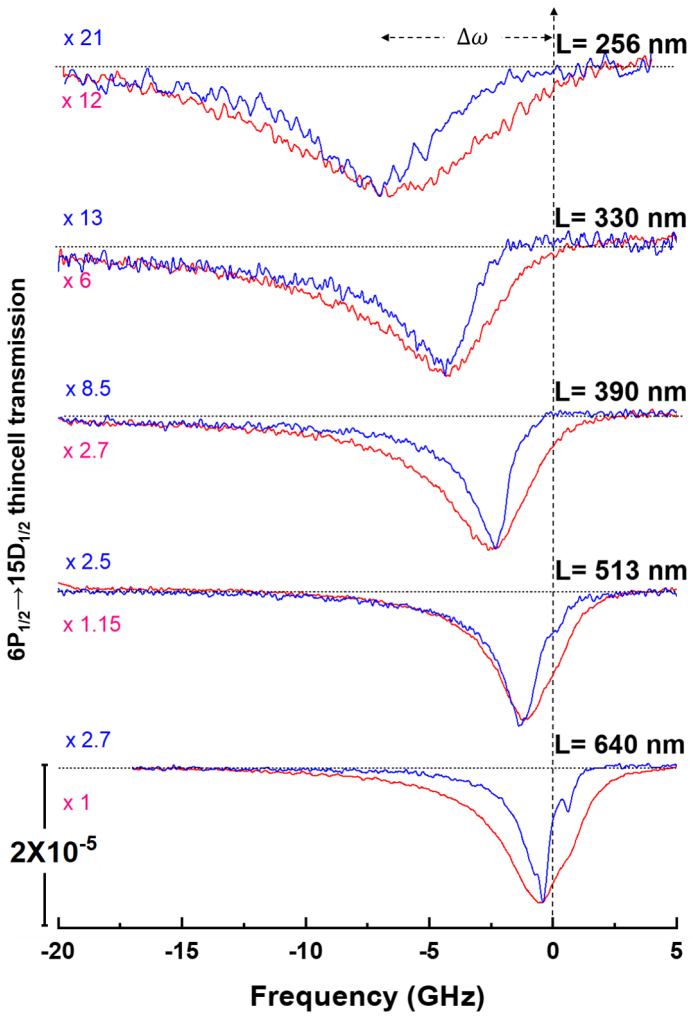

Figure 6.1: Normalized $6P_{1/2} \rightarrow 16S_{1/2}$ thin cell transmission spectra for various cell thicknesses L at two caesium vapour pressures: ~ 0.27 Torr (red line) and ~ 0.025 Torr (blue line). Signal amplitudes are normalized to off-resonance probe powers and further normalized to the maximum amplitude of transmission spectra at 640 nm for ~ 0.27 Torr Cs vapour pressure, the normalization factors are indicated with their respective colours. $\Delta\omega$ represents the redshift from the frequency reference (marked as 0). Horizontal lines indicate the zero level of each spectrum.

For a preliminary analysis of the thin cell spectra, we can suppose that the major contribution to the absorption signal comes from atoms that are in the middle of the cell at equidistant from the two reflecting surfaces [23][75] (positioned at $z = L/2$ distance from each of the cell walls). The CP frequency shift ($\Delta\omega$) at this distance can be roughly estimated from the dip (minimum) of the transmission curves. Under these oversimplifying assumptions, we can make a first estimate of the C_3 coefficient ($C_3 \sim \Delta\omega L^3/16$).

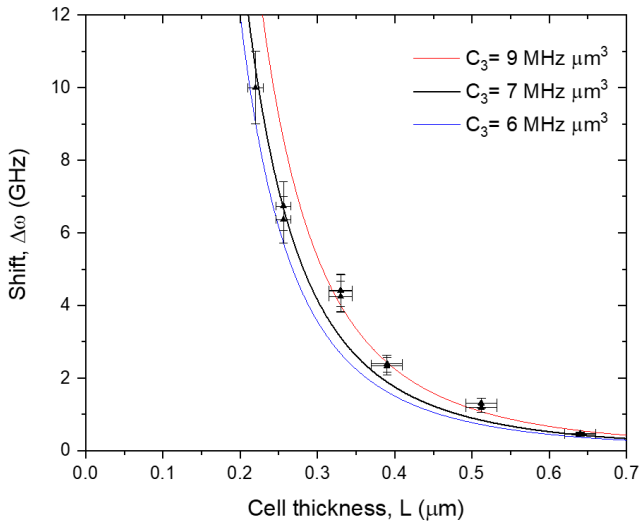

Figure 6.2: Tracing the shift (only the dip) of the $6P_{1/2} \rightarrow 16S_{1/2}$ thin cell transmission spectra as a function of cell thickness (L). The colour lines are C_3 predictions assuming the atom is placed in the middle of the cell ($C_3 \sim \Delta\omega L^3/16$).

In figure 6.2, we trace the shift of the dip of the transmission signal as a function of cell thickness (L) which broadly follows the $1/z^3$ law for these thicknesses. The apparent C_3 coefficient is here around 7 - 8 MHz μm^3 which is even larger than the value obtained by FMSR spectroscopy $\sim$ 5 MHz μm^3. One can nevertheless notice, that this preliminary set of measurements and a more rigorous presentation of thin cell experiments (exploring even smaller cell thickness) along with an analysis of transmission and reflection spectra with a more appropriate theoretical model will be the subject of the ongoing thesis of Esther Butery in the same group.

A possible reason for the discrepancies between theory and experiment could be an additional electrostatic interaction due to a charge build-up or adsorbed caesium atoms on the dielectric windows. To investigate this hypothesis further, we plan on performing FMSR measurements on a cell with fused silica (or quartz) or glass windows. Previous

studies in different vapour cells have shown that the conductivity of a glass surface in contact with a cesium vapour is more than an order of magnitude higher than that of sapphire [76]. This phenomenon that prevents the application of DC electric fields inside a glass vapour cell using external electrodes, could suggest that glass surfaces are better suited for avoiding charge build-ups and measuring Rydberg-surface interactions without the influence of external parasitic electric fields.

In our analysis of the experimental data, we have adopted an approach that assumes the interaction between Rydberg atom and surfaces occurs solely through CP interactions. Nevertheless, it is essential to acknowledge that the Stark shifts due to adsorbed atoms or parasitic electric field in the surface of the dielectric windows are known to be an important problem in precision atom-surface experiments [77][78][79][80]. In particular, high-lying states become extremely sensitive to electric fields [81][82] as their polarisability scales more rapidly ($\alpha \propto n^{\star 7}$) than the C_3 coefficient ($\propto n^{\star 4}$). A possible solution to this problem involves conducting measurements of the Stark shift for higher $nD_{3/2}$ or $nS_{1/2}$ states where the Stark shift tends to supersede the atom-surface shift. Extrapolating these findings can offer valuable insights into estimating the impact on relevant Rydberg states. It is worth noting that D states are much more sensitive to electric fields than S states. Moreover, the polarisabilities of the two states have often opposing signs (a blue Stark shift is expected for the cesium D states used in this experiment) [39]. This suggests that D states can be used to probe parasitic electric fields whose value can be subsequently used as a correction to the CP measurement of S states.

Utilizing our newly developed numerical model, we can readily adjust the potential, such as implementing a $1/z^2$ potential to simulate atom-charge interaction, or modifying velocity distributions by combining Maxwell-Boltzmann and Lorentzian distributions to emulate a velocity-selective Doppler-broadened velocity distribution. By analyzing the resulting FMSR spectra under these multifaceted approach, we aim to gain a more comprehensive understanding of the observed spectra.

Moreover, our ongoing nanometric thin-cell spectroscopy on these Rydberg transitions will offer additional insights into Rydberg-surface interactions, particularly at shorter

atom-surface separations (shorter then $\lambda/2$, approximately 250-150 nm), where the atom-surface interaction supposedly remains the predominant factor.

Chapter 7

Appendix A

7.1 Interaction between atom and its surface induced image: method of images

We treat the atom as a charge distribution $\rho(\mathbf{r})$ in the vicinity of a perfectly reflecting surface. The surface extends in the x-y plane and the atom is situated at $z>0$ (figure 2.1 same as chapter 2). In this calculation, we only consider the interaction between the atom and its surface-induced image and the interaction potential is given by:

$$\Phi^{im}(\mathbf{r}) = \int \frac{\rho^{im}(\mathbf{r}')}{|\mathbf{r}-\mathbf{r}'|} d^3r'$$

where $\Phi^{im}(\mathbf{r})$ is the potential due to image charge distribution $\rho^{im}(\mathbf{r}')$.

We take $f(\mathbf{r}') = 1/|\mathbf{r}-\mathbf{r}'|$ where

$$f|_{\mathbf{r}'=\mathbf{0}} = \frac{1}{r}$$

$$\left.\frac{\partial f}{\partial r_i'}\right|_{\mathbf{r}'=\mathbf{0}} = \frac{r_i}{r^3}$$

$$\left.\frac{\partial^2 f}{\partial r'_i \partial r'_j}\right|_{\mathbf{r'}=\mathbf{0}} = \frac{3r_i r_j}{r^5} - \frac{\delta_{ij}}{r^3}$$

$$\left.\frac{\partial^3 f}{\partial r'_i \partial r'_j \partial r'_k}\right|_{\mathbf{r'}=\mathbf{0}} = 15\frac{r_i r_j r_k}{r^7} - 3\frac{\delta_{ij}r_k + \delta_{ik}r_j + \delta_{jk}r_i}{r^5}$$

and so on.

Subsequently, the potential can be expended as (using Einstein's summation notation):

$$\Phi^{im}(\mathbf{r}) = \int \rho^{im}(\mathbf{r'}) \left[\frac{1}{r} + \frac{r_i}{r^3}r'_i + \frac{3r_i r_j - r^2\delta_{ij}}{r^5}r'_i r'_j + \frac{15r_i r_j r_k - 3r^2(\delta_{ij}r_k + \delta_{ik}r_j + \delta_{jk}r_i)}{r^7}r'_i r'_j r'_k + \ldots\right] d^3r'$$

Using the fact that $r^2 = \delta_{ij}r_i r_j$ and $r'^2 = \delta_{ij}r'_i r'_j$, we can write

$$\Phi^{im}(\mathbf{r}) = \frac{1}{r}\int \rho^{im}(\mathbf{r'})d^3r' + \frac{1}{r^3}r_i \int {r'}_i \rho^{im}(\mathbf{r'})d^3r' + \frac{1}{2r^5}r_i r_j \int \left(3r'_i r'_j - r'^2\delta_{ij}\right)\rho^{im}(\mathbf{r'})d^3r'$$

$$+\frac{1}{6r^7}r_i r_j r_k \int \left[15r'_i r'_j r'_k - 3(\delta_{ij}r'_k + \delta_{ik}r'_j + \delta_{jk}r'_i)\right]\rho^{im}(\mathbf{r'})d^3r' + \ldots$$

As mentioned previously we denote the monopole, dipole, quadrupole and octupole moment as:

- $q^{im} = \int \rho^{im}(\mathbf{r'})d^3r'$ is the image monopole moment (total charge).
- $p_i^{im} = \int {r_i}'\rho^{im}(\mathbf{r'})d^3r'$ is the image dipole moment.
- $Q_{ij}^{im} = \int \left(3r'_i r'_j - {r'}^2\delta_{ij}\right)\rho^{im}(\mathbf{r'})d^3r'$ is the image quadrupole moment.
- $T_{ijk}^{im} = \int \left[15r'_i r'_j r'_k - 3(r')^2(\delta_{ij}r'_k + \delta_{ik}r'_j + \delta_{jk}r'_i)\right]\rho^{im}(\mathbf{r'})d^3r'$ is the image octupole moment.

Rewriting the potential in a compact format (using Einstein's summation notation and neglecting the monopole term as an atom is neutral), we get:

$$\begin{aligned}\Phi^{im}(\mathbf{r}) &= p_i^{im}\frac{r_i}{r^3} + \frac{1}{2}Q_{ij}^{im}\frac{r_i r_j}{r^5} + \frac{1}{6}T_{ijk}^{im}\frac{r_i r_j r_k}{r^7} + \ldots \\ &= \Phi_p^{im}(\mathbf{r}) + \Phi_Q^{im}(\mathbf{r}) + \Phi_T^{im}(\mathbf{r}) + \ldots\end{aligned} \tag{7.1}$$

where $\Phi_p^{im}(\mathbf{r}), \Phi_q^{im}(\mathbf{r}), \Phi_t^{im}(\mathbf{r})$ are the potentials due to dipole, quadrupole and octupole moments.

7.2 Interaction energy between atom and its surface induced image

The electrostatic interaction energy (W) between the atom and image can be calculated in the following form:

$$W = \frac{1}{2}\int \rho(\mathbf{r})\Phi^{im}(\mathbf{r}+\mathbf{r_0})d^3r \tag{7.2}$$

In this expression, the origin is situated on the atom and the vector $\mathbf{r}_0$ represents the distance of the atom from its image. If $\Phi^{im}(\mathbf{r})$ is a smooth (slowly varying) function over the region where $\rho(\mathbf{r})$ is non-negligible, we perform a Taylor expansion of this potential [24] given by:

$$\Phi^{im}(\mathbf{r}+\mathbf{r_0}) = \Phi^{im}|_{\mathbf{r=0}} + r_i\frac{\partial\Phi^{im}}{\partial r_i}\bigg|_{\mathbf{r=0}} + \frac{1}{2}r_ir_j\frac{\partial^2\Phi^{im}}{\partial r_i\partial r_j}\bigg|_{\mathbf{r=0}} + \frac{1}{6}r_ir_jr_k\frac{\partial^3\Phi^{im}}{\partial r_i\partial r_j\partial r_k}\bigg|_{\mathbf{r=0}} + \dots$$

Since $\int \rho(\mathbf{r})\Phi^{im}(0)d^3r = 0$, the interaction energy can also be expended as:

$$W = \frac{1}{2}\int \rho(\mathbf{r})\left(r_i\frac{\partial\Phi^{im}}{\partial r_i}\bigg|_{\mathbf{r=0}} + \frac{1}{2}r_ir_j\frac{\partial^2\Phi^{im}}{\partial r_i\partial r_j}\bigg|_{\mathbf{r=0}} + \frac{1}{6}r_ir_jr_k\frac{\partial^3\Phi^{im}}{\partial r_i\partial r_j\partial r_k}\bigg|_{\mathbf{r=0}} + \dots\right)d^3r$$

For an external field (for the image), we know that $\delta_{ij}\dfrac{\partial\Phi}{\partial r_i\partial r_j} = 0$, we can rewrite the interaction energy as:

$$W = \underbrace{\frac{1}{2}p_i\frac{\partial\Phi}{\partial r_i}\bigg|_{\mathbf{r=0}}}_{W_1} + \underbrace{\frac{1}{12}Q_{ij}\frac{\partial^2\Phi}{\partial r_i\partial r_j}\bigg|_{\mathbf{r=0}}}_{W_2} + \underbrace{\frac{1}{24}T_{ijk}\frac{\partial^3\Phi}{\partial r_i\partial r_j\partial r_k}\bigg|_{\mathbf{r=0}}}_{W_3} + \dots \tag{7.3}$$

where

$W_1 = W_{pp^{im}} + W_{pQ^{im}} + W_{pT^{im}} + \dots$, $W_{pp^{im}}, W_{pQ^{im}}, W_{pT^{im}}$ are dipole-dipole,dipole-quadrupole, dipole-octupole atom-image interaction energies.

$W_2 = W_{Qp^{im}} + W_{QQ^{im}} + \dots$, $W_{Qp^{im}}, W_{QQ^{im}}$ are quadruple-dipole, quadruple-quadruple

atom-image interaction energies. To calculate interaction energies (equation 7.3), it becomes imperative to compute the derivatives of the potential to higher orders. The previous expression depends on the distance between the atom and its image $\mathbf{r_0}$. In the following, to simplify the notation, we replace $\mathbf{r_0}$ with $\mathbf{r}$. To calculate interaction energies (equation 7.3), it becomes imperative to compute the derivatives of the potential to higher orders.

7.2.1 Derivatives of the dipole moment

The potential due to dipole is (in index notation):

$$\Phi_p^{im}(\mathbf{r}) = \frac{p_i^{im} r_i}{r^3}$$

The first derivative of this potential is:

$$\frac{\partial \Phi_p^{im}(\mathbf{r})}{\partial r_j} = -3\frac{(p_i^{im} r_i) r_j}{r^5} + \frac{p_i^{im}}{r^3}\delta_{ij}$$

The second derivative of the dipole potential would be:

$$\frac{\partial^2 \Phi_p^{im}(\mathbf{r})}{\partial r_j \partial r_k} = -\frac{3p_i^{im} r_j}{r^5}\delta_{ik} - \frac{3(p_i^{im} r_i)}{r^5}\delta_{jk} - \frac{3p_i^{im} r_k}{r^5}\delta_{ij} + \frac{15(p_i^{im} r_i) r_j r_k}{r^7}$$

7.2.2 Derivatives of the quadruple moment

The potential due to quadruple moment is (in index notation):

$$\Phi_Q^{im}(\mathbf{r}) = \frac{1}{2}\frac{r_i Q_{ij}^{im} r_j}{r^5}$$

The field due quadruple moment can be obtained as:

$$\frac{\partial \Phi_Q^{im}(\mathbf{r})}{\partial r_k} = -\frac{5}{2}\frac{(r_i Q_{ij}^{im} r_j) r_k}{r^7} + \frac{Q_{ij}^{im} r_i}{r^5}\delta_{jk}$$

where we consider that $Q_{ij} = Q_{ji}$ the quadruple tensor is symmetric than we can write $\frac{\partial(r_i Q_{ij} r_j)}{\partial r_k} = 2Q_{ij} r_i \delta_{jk}$

The second derivative of the quadrupole moment would be:

$$\frac{\partial^2 \Phi_Q^{im}(\mathbf{r})}{\partial r_k \partial r_l} = \frac{Q_{ij}^{im}}{r^5}\delta_{jk}\delta_{il} - 5\frac{Q_{ij}^{im} r_i r_l}{r^7}\delta_{jk} - 5\frac{Q_{ij}^{im} r_i r_k}{r^7}\delta_{jl} - \frac{5}{2}\frac{(r_i Q_{ij}^{im} r_j)}{r^7}\delta_{kl} + \frac{35}{2}\frac{(r_i Q_{ij}^{im} r_j) r_k r_l}{r^9}$$

Subsequently, the other higher-order terms were also obtained (not shown here as the calculation of the higher-order terms is straightforward but tedious.)

7.2.3 Interaction energy between dipole and image dipole ($W_{pp^{im}}$)

The interaction energy between the atomic dipole ($\mathbf{p}$) and the field generated by its induced image on the wall is as follows:

$$\begin{aligned} W_{pp^{im}} &= \frac{1}{2} p_i \frac{\partial \Phi_p^{im}(\mathbf{r})}{\partial r_i} \\ &= -\frac{3}{2}\frac{(p_i^{im} r_i)(p_i r_i)}{r^5} + \frac{1}{2}\frac{p_i^{im} p_i}{r^3} \end{aligned}$$

In vector notation,

$$W_{pp^{im}} = \frac{1}{2}\frac{\mathbf{p}\cdot\mathbf{p}^{im}}{r^3} - \frac{3}{2}\frac{(\mathbf{p}\cdot\mathbf{r})(\mathbf{p}^{im}\cdot\mathbf{r})}{r^5} \tag{7.4}$$

In our case, the atomic dipole and image dipole are linked by the symmetry properties, given by:

$$\begin{cases} p_x = -p_x^{im} \\ p_y = -p_y^{im} \\ p_z = p_z^{im} \\ r = 2z \end{cases}$$

The interaction energy in the cartesian coordinate system becomes:

$$W_{pp^{im}} = -\frac{1}{16 z^3}\left[p^2 + p_z^2\right]$$

where $p^2 = p_x^2 + p_y^2 + p_z^2$.

7.2.4 Interaction energy between dipole and quadrupole image ($W_{pQ^{im}}$)

The interaction energy between the dipole ($\mathbf{p}$) and image quadrupole field is given by:

$$\begin{aligned} W_{pQ^{im}} &= p_k \frac{\partial \Phi_Q^{im}(\mathbf{r})}{\partial r_k} \\ &= p_k \left[-\frac{5}{4} \frac{(r_i Q_{ij}^{im} r_j) r_k}{r^7} + \frac{1}{2} \frac{Q_{ij}^{im} r_i \delta_{jk}}{r^5} \right] \end{aligned}$$

In vector notation:

$$W_{pQ^{im}} = -\frac{5}{4} \frac{(\mathbf{p} \cdot \mathbf{r})(\mathbf{r} \cdot \mathbf{Q}^{im} \cdot \mathbf{r})}{r^7} + \frac{1}{2} \frac{\mathbf{p} \cdot \mathbf{Q}^{im} \cdot \mathbf{r}}{r^5} \tag{7.5}$$

Similar to the previous case, the atomic quadrupole and image quadrupole moments are linked by the symmetry properties:

$$\mathbf{Q}^{im} = \begin{bmatrix} -Q_{xx} & -Q_{xy} & Q_{xz} \\ -Q_{yx} & -Q_{yy} & Q_{yz} \\ Q_{zx} & Q_{zy} & -Q_{zz} \end{bmatrix}$$

The dipole and image quadrupole interaction energy becomes:

$$W_{pQ^{im}} = \frac{1}{64 z^4} \left[3 p_z Q_{zz} + 2 p_y Q_{yz} + 2 p_x Q_{xz} \right] \tag{7.6}$$

7.2.5 Interaction energy between quadrupole and image dipole ($W_{Qp^{im}}$)

The interaction energy between the atomic quadrupole and the image dipole can be obtained as:

$$\begin{aligned} W_{Qp^{im}} &= \frac{1}{12} Q_{jk} \frac{\partial^2 \Phi_p^{im}(r)}{\partial r_j \partial r_k} \\ &= \frac{1}{12} Q_{jk} \left[-\frac{3 p_i^{im} r_j}{r^5} \delta_{ik} - \frac{3 (p_i^{im} r_i)}{r^5} \delta_{jk} - \frac{3 p_i^{im} r_k}{r^5} \delta_{ij} + \frac{15 (p_i^{im} r_i) r_j r_k}{r^7} \right] \end{aligned}$$

In vector notation:

$$W_{Qp^{im}} = \frac{1}{4}\left[-2\frac{\mathbf{p}^{im}\cdot\mathbf{Q}\cdot\mathbf{r}}{r^5} - \frac{\mathbf{p}^{im}\cdot\mathbf{r}}{r^5}\mathrm{Tr}\left(\mathbf{Q}\right) + 5\frac{(\mathbf{p}^{im}\cdot\mathbf{r})(\mathbf{r}\cdot\mathbf{Q}\cdot\mathbf{r})}{r^7}\right]$$

Knowing that $Q_{ij}\delta_{ij} = \mathrm{Tr}\left(\mathbf{Q}\right) = 0$, we have:

$$W_{Qp^{im}} = -\frac{1}{2}\frac{\mathbf{p}^{im}\cdot\mathbf{Q}\cdot\mathbf{r}}{r^5} + \frac{5}{4}\frac{(\mathbf{p}^{im}\cdot\mathbf{r})(\mathbf{r}\cdot\mathbf{Q}\cdot\mathbf{r})}{r^7} \tag{7.7}$$

By making the same assumptions as before, the quadrupole-dipole interaction energy would be (in cartesian coordinates):

$$W_{Qp^{im}} = \frac{1}{64z^4}\left[3p_zQ_{zz} + 2p_yQ_{yz} + 2p_xQ_{xz}\right] \tag{7.8}$$

7.2.6 Interaction energy between quadrupole and image quadrupole ($W_{QQ^{im}}$)

The atomic quadrupole and image quadruple interaction energy can be calculated as:

$$\begin{aligned} W_{QQ^{im}} &= \frac{1}{12}Q_{kl}\frac{\partial^2\Phi_Q^{im}}{\partial r_k\partial r_l} \\ &= \frac{1}{12}Q_{kl}\left[\frac{Q_{ij}^{im}}{r^5}\delta_{jk}\delta_{il} - 5\frac{Q_{ij}^{im}r_ir_l}{r^7}\delta_{jk} - 5\frac{Q_{ij}^{im}r_ir_k}{r^7}\delta_{jl} - \frac{5}{2}\frac{(r_iQ_{ij}^{im}r_j)}{r^7}\delta_{kl} + \frac{35}{2}\frac{(r_iQ_{ij}^{im}r_j)r_kr_l}{r^9}\right] \end{aligned}$$

In vector notation, we have:

$$W_{QQ^{im}} = \frac{1}{12}\left[\frac{\mathrm{Tr}\left(\mathbf{Q}^{im}\cdot\mathbf{Q}\right)}{r^5} - 10\frac{\mathbf{r}\cdot\mathbf{Q}\cdot\mathbf{Q}^{im}\cdot\mathbf{r}}{r^7} + \frac{35}{2}\frac{(\mathbf{r}\cdot\mathbf{Q}^{im}\cdot\mathbf{r})(\mathbf{r}\cdot\mathbf{Q}\cdot\mathbf{r})}{r^9}\right] \tag{7.9}$$

Using the symmetry properties and expressing the interaction terms in cartesian coordinates:

$$W_{QQ^{im}} = -\frac{1}{768z^5}\left[17Q_{zz}^2 + 16Q_{zy}^2 + 16Q_{zx}^2 + 2Q_{xx}^2 + 4Q_{yx}^2 + 2Q_{yy}^2\right] \tag{7.10}$$

Similarly, one can calculate the atomic dipole and image octupole interaction energy

(W_{pT}^{im}) and atomic dipole and image octupole interaction energy ($W_T p^{im}$) which goes by $1/r^5$. As mentioned before, arranging the interaction energies by their dependence over r, we can write:

$$W = \underbrace{W_{pp^{im}}}_{\sim 1/r^3} + \underbrace{W_{pQ^{im}} + W_{Qp^{im}}}_{\sim 1/r^4} + \underbrace{W_{QQ^{im}} + W_{pT^{im}} + W_{Tp^{im}}}_{\sim 1/r^5} . \tag{7.11}$$

where $W_{pp^{im}}$, $W_{pQ^{im}}$, $W_{Qp^{im}}$, $W_{QQ^{im}}$, $W_{pT^{im}}$, $W_{Tp^{im}}$ correspond to the interaction energy between atom-image: dipole-dipole, dipole-quadrupole, quadrupole-dipole, quadrupole-quadrupole, octupole-quadrupole, octupole-octupole respectively (batched together with their dependence over r).

Bibliography

[1] JE Lennard-Jones. Processes of adsorption and diffusion on solid surfaces. *Transactions of the Faraday Society*, 28:333–359, 1932.

[2] Hendrik BG Casimir and Dirk Polder. The influence of retardation on the london-van der waals forces. *Physical Review*, 73(4):360, 1948.

[3] EA Hinds, KS Lai, and M Schnell. Atoms in micron-sized metallic and dielectric waveguides. *Philosophical Transactions of the Royal Society of London. Series A: Mathematical, Physical and Engineering Sciences*, 355(1733):2353–2365, 1997.

[4] Cenap Ates, Thomas Pohl, Thomas Pattard, and Jan M Rost. Many-body theory of excitation dynamics in an ultracold rydberg gas. *Physical Review A*, 76(1):013413, 2007.

[5] A Urvoy, F Ripka, Igor Lesanovsky, D Booth, JP Shaffer, T Pfau, and R Löw. Strongly correlated growth of rydberg aggregates in a vapor cell. *Physical Review Letters*, 114(20):203002, 2015.

[6] Fabian Ripka, Harald Kübler, Robert Löw, and Tilman Pfau. A room-temperature single-photon source based on strongly interacting rydberg atoms. *Science*, 362(6413):446–449, 2018.

[7] Matt T Simons, Joshua A Gordon, and Christopher L Holloway. Atom-based rf electric field metrology above 100 ghz. In *Terahertz, RF, Millimeter, and Submillimeter-Wave Technology and Applications IX*, volume 9747, pages 216–222. SPIE, 2016.

[8] JA Sedlacek, A Schwettman, and H Kübler. R. löw, t. pfau, and jp shaffer, 2012.

[9] Christopher G Wade, Nikola Šibalić, Natalia R de Melo, Jorge M Kondo, Charles S Adams, and Kevin J Weatherill. Real-time near-field terahertz imaging with atomic optical fluorescence. *Nature Photonics*, 11(1):40–43, 2017.

[10] Ofer Firstenberg, Charles S Adams, and Sebastian Hofferberth. Nonlinear quantum optics mediated by rydberg interactions. *Journal of Physics B: Atomic, Molecular and Optical Physics*, 49(15):152003, 2016.

[11] Callum Murray and Thomas Pohl. Quantum and nonlinear optics in strongly interacting atomic ensembles. In *Advances in Atomic, Molecular, and Optical Physics*, volume 65, pages 321–372. Elsevier, 2016.

[12] JA Crosse, Simen Å Ellingsen, Kate Clements, Stefan Y Buhmann, and Stefan Scheel. Thermal casimir-polder shifts in rydberg atoms near metallic surfaces. *Physical Review A*, 82(1):010901, 2010.

[13] Johannes Block and Stefan Scheel. Casimir-polder-induced rydberg macrodimers. *Physical Review A*, 100(6):062508, 2019.

[14] EA Hinds and Vahid Sandoghdar. Cavity qed level shifts of simple atoms. *Physical Review A*, 43(1):398, 1991.

[15] Harald Kübler, JP Shaffer, T Baluktsian, R Löw, and T Pfau. Coherent excitation of rydberg atoms in micrometre-sized atomic vapour cells. *Nature Photonics*, 4(2):112–116, 2010.

[16] Georg Epple, Nicolas Y Joly, Tijmen G Euser, Philip St. J Russell, and Robert Löw. Effect of stray fields on rydberg states in hollow-core pcf probed by higher-order modes. *Optics Letters*, 42(17):3271–3274, 2017.

[17] AM. Akul'shin, V.L. Velichanskii, AS Zibrov, V.V. Nikitin, V.A. Sautenkov, EK Yurkin, and N.V. Senkov. Collisional broadening of intra doppler resonances of selective reflection on the d1 line of cesium. *JETP Letters*, 36:303, 1982.

[18] M. Ducloy and M. Fichet. General theory of frequency modulated selective reflection. influence of atom surface interactions. *Journal of Physics II France*, 1:777, 1991.

[19] M. Fichet, F. Schuller, D. Bloch, and M. Ducloy. van der waals interactions between excited-state atoms and dispersive dielectric surfaces. *Physical Review A*, 51(2):1553, 1995.

[20] Martine Chevrollier, Michèle Fichet, Marcos Oria, Gabriel Rahmat, Daniel Bloch, and Martial Ducloy. High resolution selective reflection spectroscopy as a probe of long-range surface interaction: measurement of the surface van der waals attraction exerted on excited cs atoms. *Journal de Physique II*, 2(4):631–657, 1992.

[21] H. Failache, S. Saltiel, M. Fichet, D. Bloch, and M. Ducloy. Resonant coupling in the van der waals interaction between an excited alkali atom and a dielectric surface: an experimental study via stepwise selective reflection spectroscopy. *The European Physical Journal D-Atomic, Molecular, Optical and Plasma Physics*, 23:237–255, May 2003.

[22] Athanasios Laliotis, Thierry de Silans, Isabelle Maurin, et al. Casimir–polder interactions in the presence of thermally excited surface modes. *Nature Communications*, 5:4364, 2014.

[23] M. Fichet, G. Dutier, A. Yarovitsky, P. Todorov, I. Hamdi, I. Maurin, S. Saltiel, D. Sarkisyan, M.-P. Gorza, and D. Bloch. Exploring the van der waals atom-surface attraction in the nanometric range. *Europhysics Letters*, 77(5):54001, 2007.

[24] John David Jackson. Classical electrodynamics 3rd edition, ed john wiley & sons. *Inc., New York, USA*, 1998.

[25] B Numerov. Note on the numerical integration of d2x/dt2= f (xt). *Astronomische Nachrichten, volume 230, Issue 19, p. 359*, 230:359, 1927.

[26] Nenad M Sakan and Zoran Simic. Numerov method analysis with a goal of application of complex plasma models. *MNRAS*, 406:590–596, 2010.

[27] C J Lorenzen and K Niemax. Precise quantum defects of ns, np and nd levels in cs i. *Zeitschrift für Physik A Atoms and Nuclei*, 315:127–133, 1984.

[28] M Marinescu, HR Sadeghpour, and A Dalgarno. Dispersion coefficients for alkali-metal dimers. *Physical Review A*, 49(2):982, 1994.

[29] Jun John Sakurai and Eugene D Commins. Modern quantum mechanics, revised edition, 1995.

[30] Constantine E Theodosiou. Lifetimes of alkali-metal—atom rydberg states. *Physical Review A*, 30(6):2881, 1984.

[31] II Beterov, II Ryabtsev, DB Tretyakov, and VM Entin. Quasiclassical calculations of blackbody-radiation-induced depopulation rates and effective lifetimes of rydberg n s, n p, and n d alkali-metal atoms with n 80. *Physical review A*, 79(5):052504, 2009.

[32] R Gupta, W Happer, LK Lam, and Sune Svanberg. Hyperfine-structure measurements of excited s states of the stable isotopes of potassium, rubidium, and cesium by cascade radio-frequency spectroscopy. *Physical Review A*, 8(6):2792, 1973.

[33] P Goy, JM Raimond, G Vitrant, and S Haroche. Millimeter-wave spectroscopy in cesium rydberg states. quantum defects, fine-and hyperfine-structure measurements. *Physical Review A*, 26(5):2733, 1982.

[34] D Meschede, W Jhe, and EA Hinds. Radiative properties of atoms near a conducting plane: An old problem in a new light. *Physical Review A*, 41(3):1587, 1990.

[35] Stefan Yoshi Buhmann and Dirk-Gunnar Welsch. Casimir-polder forces on excited atoms in the strong atom-field coupling regime. *Physical Review A*, 77(1):012110, 2008.

[36] J-Y Courtois, J-M Courty, and JC Mertz. Internal dynamics of multilevel atoms near a vacuum-dielectric interface. *Physical Review A*, 53(3):1862, 1996.

[37] J Dalibard, J Dupont-Roc, and C Cohen-Tannoudji. Vacuum fluctuations and radiation reaction: identification of their respective contributions. *Journal de Physique*, 43(11):1617–1638, 1982.

[38] Horacio Failache. *Etude spectroscopique des couplages résonnants dans l'interaction de van der Waals entre un atome et une surface diélectrique*. PhD thesis, PhD thesis, 1999.

[39] ARC Alkali Rydberg Calculator. ARC Alkali Rydberg Calculator Documentation. https://arc-alkali-rydberg-calculator.readthedocs.io/en/latest/index.html, n.d. Accessed: July 29, 2023.

[40] J. M. Wylie and J. E. Sipe. Quantum electrodynamics near an interface. ii. *Physical Review A*, 32:2030–2043, 1985.

[41] J. M. Wylie and J. E. Sipe. Quantum electrodynamics near an interface. *Physical Review A*, 30:1185–1193, 1984.

[42] A Laliotis and M Ducloy. Casimir-polder effect with thermally excited surfaces. *Physical Review A*, 91(5):052506, 2015.

[43] Thierry Passerat de Silans. *Interaction atome-surface: interaction de van der waals entre un atome excité et une surface diélectrique thermiquement émissive: oscillations de bloch pour un atome adsorbé*. PhD thesis, Université Paris-Nord-Paris XIII, 2009.

[44] JC de Aquino Carvalho, I Maurin, P Chaves de Souza Segundo, A Laliotis, D de Sousa Meneses, and D Bloch. Spectrally sharp near-field thermal emission: revealing some disagreements between a casimir-polder sensor and predictions from far-field emittance. *Physical Review Letters*, 131(14):143801, 2023.

[45] Athanasios Laliotis, Thierry Passerat De Silans, Isabelle Maurin, Martial Ducloy, and Daniel Bloch. Casimir-polder interactions in the presence of thermally excited surface modes. *Nature communications*, 5(1):4364, 2014.

[46] Horacio Failache, Solomon Saltiel, Michèle Fichet, Daniel Bloch, and Martial Ducloy. Resonant van der waals repulsion between excited cs atoms and sapphire surface. *Physical Review Letters*, 83(26):5467, 1999.

[47] M-P Gorza and M Ducloy. Van der waals interactions between atoms and dispersive surfaces at finite temperature. *The European Physical Journal D-Atomic, Molecular, Optical and Plasma Physics*, 40:343–356, 2006.

[48] AS Barker Jr. Infrared lattice vibrations and dielectric dispersion in corundum. *Physical review*, 132(4):1474, 1963.

[49] Mathias Schubert, TE Tiwald, and CM Herzinger. Infrared dielectric anisotropy and phonon modes of sapphire. *Physical Review B*, 61(12):8187, 2000.

[50] Joao Carlos de Aquino Carvalho. *Interaction Casimir-Polder entre atome de césium et surface de saphir thermiquement émissive*. PhD thesis, Sorbonne Paris Cité, 2018.

[51] Gabriel Dutier, Solomon Saltiel, Daniel Bloch, and Martial Ducloy. Revisiting optical spectroscopy in a thin vapor cell: mixing of reflection and transmission as a fabry–perot microcavity effect. *JOSA B*, 20(5):793–800, 2003.

[52] Gabriel Dutier. *Cavité nanométrique de vapeur de Césium: Spectroscopie à haute résolution et interaction de surface de type Van Der Waals*. PhD thesis, Université Paris 13, France, 2003.

[53] G. Nienhuis, F. Schuller, and M. Ducloy. Nonlinear selective reflection from an atomic vapor at arbitrary incidence angle. *Physical Review A*, 38(10):5197, 1988.

[54] F. Schuller, M. Ducloy, and G. Nienhuis. Schuller f., ducloy m. and nienhuis g., ann. phys. france ls (1990) cl-183. *Ann. Phys. France*, ls:Cl–183, 1990.

[55] F. Schuller, G. Nienhuis, and M. Ducloy. Schuller f., nienhuis g. and ducloy m., phys. rev. a 43 (1991) 443. *Physical Review A*, 43:443, 1991.

[56] G. Nienhuis, F. Schuller, and M. Ducloy. Nienhuis g., schuller f. and ducloy m., phys. rev. a38 (1988) 5197. *Physical Review A*, 38:5197, 1988.

[57] M. F. H. Schuurmans. Schuurmans m. f. h., j. phys. france 37 (1976) 469. *Journal de Physique France*, 37:469, 1976.

[58] M. Chevrollier, D. Bloch, G. Rahmat, and M. Ducloy. Van der waals-induced spectral distortions in selective-reflection spectroscopy of cs vapor: The strong atom–surface interaction regime. *Optics Letters*, 16(23):1879–1881, 1991.

[59] DE Van Dobben and CrS BRUYN. Cumulative sum tests: theory and practice. *Hafner, New York, NY*, 1968.

[60] Pierre-François Verhulst. Notice sur la loi que la population poursuit dans son accroissement. *Correspondance Mathématique et Physique*, 10:113–121, 1838. PDF.

[61] Eric W. Weisstein. Sigmoid function. MathWorld–A Wolfram Web Resource, Accessed: [Replace with the date you accessed the webpage].

[62] Petko Todorov and Daniel Bloch. Testing the limits of the maxwell distribution of velocities for atoms flying nearly parallel to the walls of a thin cell. *The Journal of Chemical Physics*, 147(19), 2017.

[63] V. Sandoghdar, C.I. Sukenik, S. Haroche, and E.A. Hinds. Spectroscopy of atoms confined to the single node of a standing wave in a parallel-plate cavity. *Physical Review A*, 53(3):1919, 1996.

[64] D. Sarkisyan et al. Sarkisyan d. et al., opt. commun., 200 (2001) 201. *Optics Communications*, 200:201, 2001.

[65] G. Dutier et al. Dutier g. et al., europhys. lett., 63 (2003) 35. *Europhysics Letters*, 63:35, 2003.

[66] Milton Abramovitz and Irene A Stegun. *Handbook of mathematical functions. With formulas, graphs and mathematical tables*. Dover, 1964.

[67] RH Dicke. The effect of collisions upon the doppler width of spectral lines. *Physical Review*, 89(2):472, 1953.

[68] ZJ Jabbour, RK Namiotka, J Huennekens, Maria Allegrini, S Milošević, and F De Tomasi. Energy-pooling collisions in cesium: 6 p j+ 6 p j→ 6s+ (nl= 7p, 6d, 8s, 4f). *Physical Review A*, 54(2):1372, 1996.

[69] Ennio Arimondo, M Inguscio, and P Violino. Experimental determinations of the hyperfine structure in the alkali atoms. *Reviews of Modern Physics*, 49(1):31, 1977.

[70] Daniel A Steck. Cesium d line data. 2003.

[71] Martine Chevrollier. *Spectroscopie de réflexion sélective à une interface diélectrique/vapeur de césium : observation de l'attraction van der Waals de surface*. PhD thesis, Paris 13, 1992.

[72] Joao Carlos de Aquino Carvalho, Athanasios Laliotis, Martine Chevrollier, Marcos Oriá, and Daniel Bloch. Backward-emitted sub-doppler fluorescence from an optically thick atomic vapor. *Physical Review A*, 96(4):043405, 2017.

[73] J Huennekens, RK Namiotka, J Sagle, ZJ Jabbour, and Maria Allegrini. Thermalization of velocity-selected excited-state populations by resonance exchange collisions and radiation trapping. *Physical Review A*, 51(6):4472, 1995.

[74] DC Thompson, E Weinberger, G-X Xu, and BP Stoicheff. Frequency shifts and line broadenings in collisions between rydberg and ground-state alkali-metal atoms. *Physical Review A*, 35(2):690, 1987.

[75] Vahid Sandoghdar, CI Sukenik, EA Hinds, and Serge Haroche. Direct measurement of the van der waals interaction between an atom and its images in a micron-sized cavity. *Physical review letters*, 68(23):3432, 1992.

[76] MA Bouchiat, J Guéna, Ph Jacquier, M Lintz, and AV Papoyan. Electrical conductivity of glass and sapphire cells exposed to dry cesium vapor. *Applied Physics B*, 68:1109–1116, 1999.

[77] Mauro Antezza, Lev P. Pitaevskii, and Sandro Stringari. Effect of the casimir-polder

force on the collective oscillations of a trapped bose-einstein condensate. *Phys. Rev. A*, 70:053619, Nov 2004.

[78] J. M. McGuirk, D. M. Harber, J. M. Obrecht, and E. A. Cornell. Alkali-metal adsorbate polarization on conducting and insulating surfaces probed with bose-einstein condensates. *Phys. Rev. A*, 69:062905, Jun 2004.

[79] J. M. Obrecht, R. J. Wild, and E. A. Cornell. Measuring electric fields from surface contaminants with neutral atoms. *Phys. Rev. A*, 75:062903, Jun 2007.

[80] Yann Balland, Luc Absil, and Franck Pereira dos Santos. Quectonewton local force sensor, 2023.

[81] H. Hattermann, M. Mack, F. Karlewski, F. Jessen, D. Cano, and J. Fortágh. Detrimental adsorbate fields in experiments with cold rydberg gases near surfaces. *Phys. Rev. A*, 86:022511, Aug 2012.

[82] H. Kübler, J. P. Shaffer, T. Baluktsian, R. Löw, and T. Pfau. Coherent excitation of Rydberg atoms in micrometre-sized atomic vapour cells. *Nature Photonics*, 4(2):112–116, February 2010.